Quantitative Image Reconstruction Methods for Low Signal-To-Noise Ratio Emission Tomography

by

Hongki Lim

A dissertation submitted in partial fulfillment
of the requirements for the degree of
Doctor of Philosophy
(Electrical and Computer Engineering)
in the University of Michigan
2020

Doctoral Committee:

        Professor Yuni K. Dewaraja, Co-Chair
        Professor Jeffrey A. Fessler, Co-Chair
        Professor Jason J. Corso
        Professor Issam El Naqa

Hongki Lim

hongki@umich.edu

ORCID iD: 0000-0002-2764-3730

To my God.

Acknowledgments

First of all, I would like to thank my advisor Prof. Jeff Fessler with my deepest respect. I remember the moment when I emailed him to ask about research opportunity after taking his class. It took me several months to click the "send" button because I was worried about myself of being mediocre student unlike the ingenious professor. However, thanks to his generous acceptance and encouragement, I was able to approach the finish line of my PhD journey. Trying to be like him itself was a greatest education in my life. I would also like to thank Prof. Yuni Dewaraja for her endless patience over me. I even had not heard about PET or SPECT when I begin the research, but she kindly taught me the basics of emission tomography again and again. I have made so many mistakes and it was her additional work to catch and correct the mistakes. I also appreciate her generous support for my professional growth. I would also thank those who have served on my committee, Profs. Jason Corso, Issam El Naqa, for their time and contributions to this dissertation.

Finally, I would like to thank my parents for the lifelong support and my wife Jina for her passionate love.

Table of Contents

List of Figures

FIGURE

List of Tables

TABLE

Abstract

Novel internal radionuclide therapies such as radioembolization (RE) with Y-90 loaded microspheres and targeted therapies labeled with Lu-177 offer a unique promise for personalized treatment of cancer because imaging-based pre-treatment dosimetry assessment can be used to determine administered activities, which deliver tumoricidal absorbed doses to lesions while sparing critical organs. At present, however, such therapies are administered with fixed or empiric activities with little or no dosimetry planning. The main reason for lack of dosimetry guided personalized treatment in radionuclide therapies is the challenges and impracticality of quantitative emission tomography imaging and the lack of well established dose-effect relationships, potentially due to inaccuracies in quantitative imaging. While radionuclides for therapy have been chosen for their attractive characteristics for cancer treatment, their suitability for emission tomography imaging is less than ideal. For example, imaging of the almost pure beta emitter, Y-90, involves SPECT via bremsstrahlung photons that have a low and tissue dependent yield or PET via a very low abundance positron emission (32 out of 1 million decays) that leads to a very low true coincidence-rate in the presence of high singles events from bremsstrahlung photons. Lu-177 emits gamma-rays suitable for SPECT, but they are low in intensity (113 keV: 6%, 208 keV: 10%), and only the higher energy emission is generally used because of the large downscatter component associated with the lower energy gamma-ray.

The main aim of the research in this thesis is to improve accuracy of quantitative PET and SPECT imaging of therapy radionuclides for dosimetry applications. Although PET is generally considered as superior to SPECT for quantitative imaging, PET imaging of 'non-pure' positron emitters can be complex. We focus on quantitative SPECT and PET imaging of two widely used therapy radionuclides, Lu-177 and Y-90, that have challenges associated with low count-rates. The long term goal of our work is to apply the methods we develop to patient imaging for dosimetry based planning to optimize the treatment either before therapy or after each cycle of therapy. For Y-90 PET/CT, we developed an image reconstruction formulation that relaxes the conventional image-domain nonnegativity constraint by instead imposing a positivity constraint on the predicted measurement mean that demonstrated improved quantification in simulated patient studies. For Y-90 SPECT/CT, we propose a new SPECT/CT reconstruction formulation including tissue dependent probabilities for bremsstrahlung generation in the system matrix. In addition to above mentioned quantitative

image reconstruction methods specifically developed for each modality in Y-90 imaging, we propose a general image reconstruction method using trained regularizer for low-count PET and SPECT that we test on Y-90 and Lu-177 imaging. Our approach starts with the raw projection data and utilizes trained networks in the iterative image formation process. Specifically, we take a mathematics-based approach where we include convolutional neural networks within the iterative reconstruction process arising from an optimization problem. We further extend the trained regularization method by using anatomical side information. The trained regularizer incorporates the anatomical information using the segmentation mask generated by a trained segmentation network where its input is the co-registered CT image. Overall, the emission tomography methods we have proposed in this work are expected to enhance low-count PET and SPECT imaging of therapy radionuclides in patient studies, which will have value in establishing dose – response relationships and developing imaging based dosimetry guided treatment planning strategies in the future.

CHAPTER 1

Introduction

Treatment based on fixed- or weight- adjusted activities continues to be the standard of care in most targeted radionuclide therapies (TRT). This practice starkly contrasts with external beam radiotherapy where precise treatment plans are developed on an individualized basis to predict and manage absorbed dose to target lesions and to normal organs. The barriers to improving efficacy of internally administered therapy by implementing such an approach start with the lack of well validated imaging and dosimetry tools that are practical for the clinical environment, and lack of studies that establish convincing relationships between absorbed dose and response [1, 2], potentially due to inaccuracies in absorbed dose estimation. Accurately segmenting and quantifying the activity in lesions/normal organs is imperative for accurate dosimetry because the absorbed dose to a volume of interest depends on the time-integrated (cumulated) activity in the source volumes. While radionuclides for therapies have attractive characteristics for the treatment of cancerous tumors, imaging such radionuclides is challenging and complex. For example, imaging of the almost 'pure' beta emitter Y-90 involves SPECT via bremsstrahlung photons produced with low probability by the betas or PET via a very low abundance positron in the presence of bremsstrahlung that leads to low signal-to-noise, especially in low-uptake regions such as the non-tumoral liver in Y-90 radioembolization. Because of the challenges of direct quantitative imaging of therapy radionuclides, often surrogate imaging tracers are used prior to therapy to predict the distribution, pharmacokinetics and dosimetry of the therapy administration. For example for Y-90 microsphere radioembolization, particles labelled with Tc-99m serve as a SPECT imaging surrogate while for Lu-177 targeted therapies radiotracers labelled with Ga-68 serve as a PET surrogate. However, because of differences between the distribution pattern/pharmacokinetics of the imaging surrogate and the therapeutic agent [3], improving direct imaging of the actual delivered Y-90 and Lu-177 is of much value for dosimetry applications.

Our aim is to develop methods for accurate quantitative low count emission tomography imaging of 'difficult to image radionculides' and these methods are discussed in this dissertation. We focus on Y-90 PET and SPECT and Lu-177 SPECT, but with some adjustment, these methods can be generalized to other radionuclides. In addition to enhancing accuracy of imaging based dosimetry
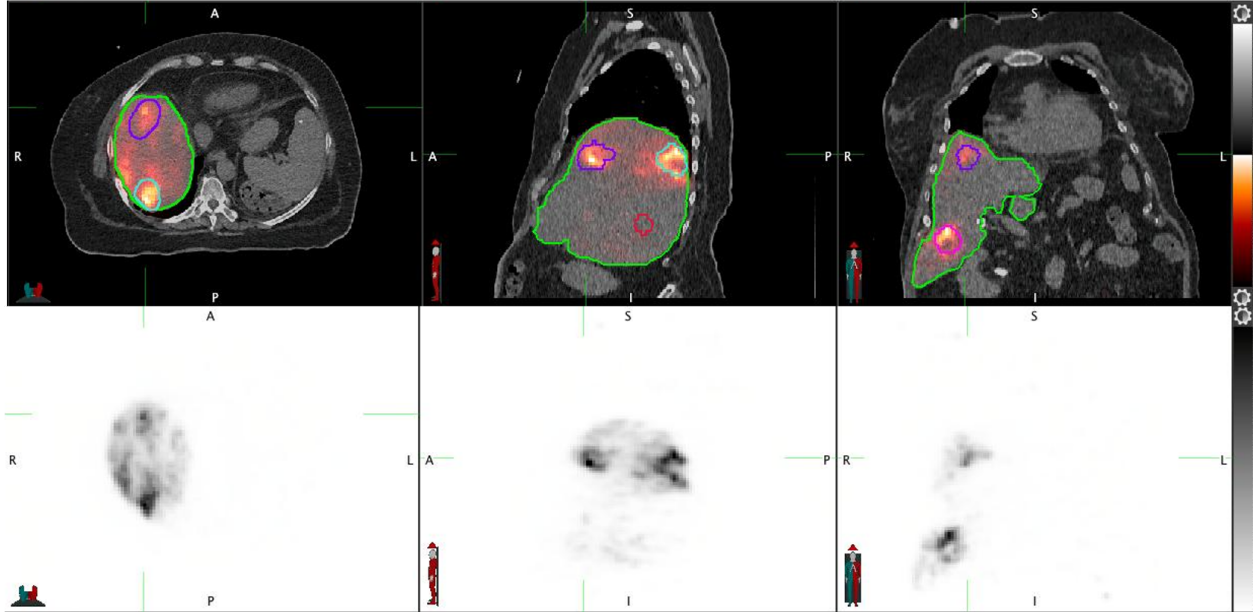
Figure 1.1: Y-90 PET/CT and PET images corresponding to a patient treated with 5.8 GBq of Y-90 microspheres to the right lobe. Liver (green) and lesion segmentations are indicated in the PET/CT images.

our methods are expected to enhance practicality of dosimetry guided treatment. Improving low count imaging enables short scan times that reduce the imaging burden on patients and to the clinic and facilitates whole body imaging, rarely performed for Y-90 PET or Lu-177 SPECT because of the requirements on camera time. It also enables imaging at later time points, where count-rates are substantially lower, relevant when time-activity data are needed to determine cumulated activities for dosimetry. Finally, enhancing low-count imaging opens up the possibility of pre-therapy imaging directly with tracer quantities (typically < 185 GBq) of Y-90 or Lu-177 instead of relying on surrogate imaging agents. Direct pre-treatment imaging with Lu-177 or Y-90 is currently not performed in the clinic, because with the low count-rates it is considered infeasible. Enhancing low count imaging is particularly relevant when voxel-level activity quantification is of interest as in 3-D dosimetry applications.

This work focuses both on formulating new reconstruction strategies as well as clinically relevant evaluations in Lu-177 SPECT and Y-90 PET and SPECT studies. Ground-truth activity distribution is available in simulation and phantom measurement studies, whereas true activity distribution is unknown in patient studies. Therefore, we mainly evaluated the quantification/noise improvements made by our proposed methods with simulation and phantom measurement studies in Chapter 3-6 using geometries, count-rates and distributions that are typical for Y-90 radioembolization or Lu-177 targeted radionuclide therapy. However, we also show and discuss the impact of the proposed methods on patient studies with visualization and available evaluation metrics.

| Standard acquisition SPECT/CT | Standard acquisition (25 minutes) | Emulated pre-therapy acquisition (1 minute) |
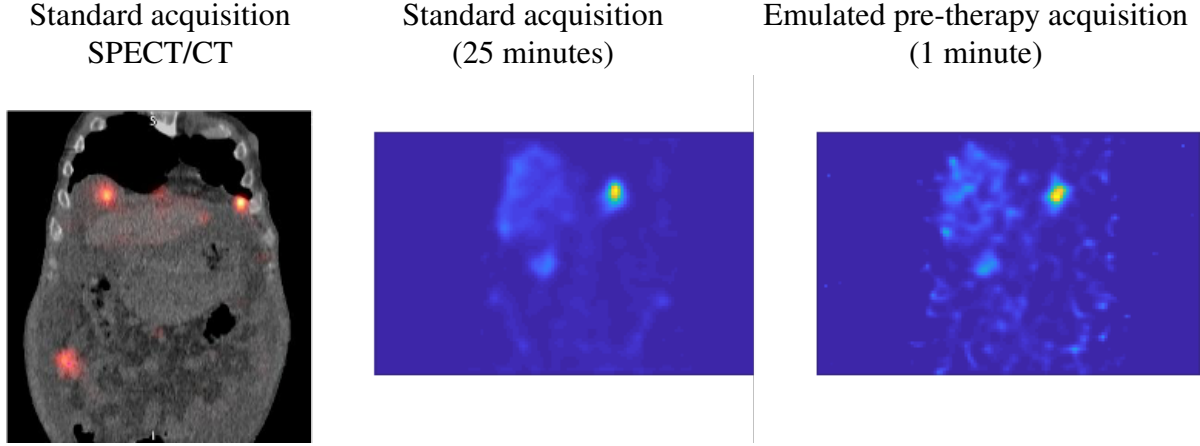
Figure 1.2: An example demonstrating the challenge of Lu-177 SPECT imaging with tracer quantities of Lu-177 due to the low intensity of the Lu-177 gamma-ray and the corresponding low count-rates. The image on the left corresponding to a 7.4 GBq therapy administration, 25 min acquisition. The image on the right was acquired at the end of the imaging session with a reduced acquisition time of 1 min to emulate a $\sim$300 MBq tracer administration. We aim to improve low-count SPECT to reduce noise for pre-therapy imaging as well as to enhance post-therapy imaging with shorter acquisition times, later imaging time points and voxel-level estimation.

In the first part of our work (Chapter 3), we implemented a new PET reconstruction formulation that enforces nonnegativity of the projections instead of the voxel values that is standard for conventional reconstruction as in (2.9). Unlike most existing PET reconstruction methods that impose non-negativity constraints on the reconstructed image, which produce biased reconstructions in low count setting, this new formulation allows some negative voxel values thereby potentially reducing bias. The impact of biased reconstruction on low counts Y-90 PET is well recognized [4], but to our knowledge solutions specific to Y-90 had not been proposed. Previous related works used modifications of the log-likelihood for Poisson data. Because maximum likelihood estimation (based on the correct statistical model) is known to be asymptotically efficient (lowest possible variance of an unbiased estimator), modifying the log-likelihood may affect image noise properties and the modifications require additional parameters to tune. Our objective is similar to these previous works, namely reducing the bias observed in low statistics PET, especially for Y-90 PET. However, our proposed algorithm is distinct because it avoids modifying or approximating the Poisson log-likelihood used in the data-fit term. To relax the non-negativity constraint embedded in PET reconstruction while retaining the original Poisson likelihood, we used an Alternating Direction Method of Multipliers (ADMM) and applied the automatic parameter selection method to improve the convergence speed. The new formulation improved quantification in simulation studies and demonstrated improved contrast recovery with patient and phantom PET measurements data. The efficacy of our method is especially notable when the activity concentration in the volume of interest

is very low.

In the second part of our work (Chapter 4), we incorporated the tissue-dependent probability of bremsstrahlung production into the Y-90 SPECT/CT image reconstruction method. We added a term to the system matrix to model the bremsstrahlung spectra produced in each voxel as a bone-volume fraction weighted mixture of the bone-only and tissue-only spectra to consider the material dependence of the bremsstrahlung generation, which is disregarded in existing reconstruction methods. While the yield of positrons used in Y-90 PET is independent of the tissue media, the yield of bremsstrahlung photons used in SPECT is tissue dependent because bremsstrahlung photon generation is proportional to atomic number of the tissue medium. As a consequence of the atomic number dependence of the bremsstrahlung production probability, the same amount of Y-90 activity in different tissue regions of the body will generate different numbers of bremsstrahlung photons, which impacts both qualitative and quantitative assessment of Y-90 SPECT images. The difference in bremsstrahlung production probabilities (per beta decay) is particularly significant when comparing bone and soft tissue. Although this effect may not significantly impact (homogeneous) liver imaging, it is expected to impact quantification accuracy in heterogeneous regions such as marrow near bone, which is of interest in bone marrow dosimetry in Y-90 radioimmunotherapy. There were no prior works addressing the tissue dependence of bremsstrahlung generation, hence the Y-90 images reported are the distribution of the external bremsstrahlung photons generated by the beta particles and not the Y-90 activity distribution.

In the third part of our work (Chapter 5), we proposed a trained regularizer based iterative reconstruction method that mitigates bias effects with lower computational costs and without increasing noise. Conventional regularizers used in emission tomography penalize differences between neighboring pixels. That approach is equivalent to assuming that convolving the image with the finite difference filters along different directions produces sparse outputs. Using such "hand-crafted" filters is unlikely to be the best approach. A recent trend is to use training data to learn filters that produce sparse outputs when convolved with images of interest. Previous training-based regularization methods for emission tomography borrowed the neural networks that were developed for other purposes (e.g., medical image segmentation). However, the proposed framework is derived by an optimization formulation with a mathematical motivation, characterized by fewer parameters, thereby avoiding over-fitting and making training from small data sets feasible. The numerical results showed that proposed method significantly improves PET reconstruction performance whereas conventional state-of-the-art regularizers had a trade-off between noise and quantification.

In the last part of our work (Chapter 6), we further extend the trained regularizer for emission image reconstruction in Chapter 5 by using anatomical information available from co-registered CT or MR. Most existing trained regularizers for emission tomography do not fully exploit the

information from dual-modality system like SPECT-CT or PET-MR. Incorporating anatomical information into emission tomography can be beneficial because anatomical images have better resolution than emission images and offer accurate boundary information. We propose multi-modality based regularizer which is exploiting anatomical side information provided with CT segmentation mask given by trained segmentation network. We tested the efficacy of the proposed method with an application in Lu-177 SPECT. The numerical and qualitative results showed that proposed method significantly improves SPECT reconstruction performance compared to the conventional regularization method using CT-side information.

The summary of original contributions of this dissertation is as follows:

- New Y-90 PET reconstruction algorithm enforcing new non-negativity constraint is developed [5–7].

- New Y-90 SPECT reconstruction algorithm incorporating new tissue-dependent bremsstrahlung generation probability is developed [8, 9].

- New trained regularizer for general low-count imaging is developed [10–12].

- New trained regularizer using CT-side information from dual modality system (e.g., SPECT/CT) is developed [13].

CHAPTER 2

Background

This chapter reviews background material of PET and SPECT nuclear medicine imaging modalities that is used in subsequent chapters. Emission tomography (ET) uses radioactive material to image the body's physiology. ET is categorized as a functional imaging because it shows functional properties of human body such as metabolism and blood flow. For example, F-18 fludeoxyglucose (FDG) is a radionuclide combined with glucose and it is metabolized by the cell and remains within the cell. Because malignant tumor cells tend to have higher glucose metabolism than the healthy cells, high uptake of FDG indicates the possible existence of malignant cells. Besides the radionuclides used for diagnostic imaging purposes such as F-18 widely used in PET imaging and Tc-99m widely used in diagnostics SPECT imaging, theranostic (therapy + diagnostic) radionuclides enable both imaging and delivery of tumoricidal radiation absorbed doses to destroy cancerous cells. Two such examples are Y-90 and Lu-177, both of which emit beta particles that are widely used to deliver the therapeutic effect in radionuclide therapy. For example, transarterial radioembolization with microspheres loaded with Y-90 is an established treatment for unresectable hepatocellular carcinoma and for liver metastases, with promising clinical results that show longer progression free survival (PFS) with reduced toxicity than chemoembolization [14] and a survival advantage over (sorafenib) chemotherapy [15]. Another example is Lu-177 DOTATATE, a targeted radionuclide therapy (TRT) that was recently FDA approved for treatment of neuroendocrine tumors (NETs). Lu-177 is preferentially delivered to tumor cells by DOTATATE, which binds to the somatostatin receptors expressed by most well-differentiated NETs [16]. A randomized trial [17] demonstrated a markedly longer PFS with Lu-177 DOTATATE than the control group receiving the non-radioactive DOTATATE, the current standard of care.

Both Lu-177 and Y-90 are considered as theransotic radionculides because in addition to the beta particles they emit that are used to deliver the tumorcidal radiation, they are both associated with photons or gamma-ray emissions that can be used to directly image and quantify the activity distribution in the patient. However, quantitative imaging with these therapy radionculides is considerably more challenging than diagnostics radionuclides such as Tc-99m in SPECT and F-18 in PET that have been chosen for their ideal characteristics for imaging. Thus, there is
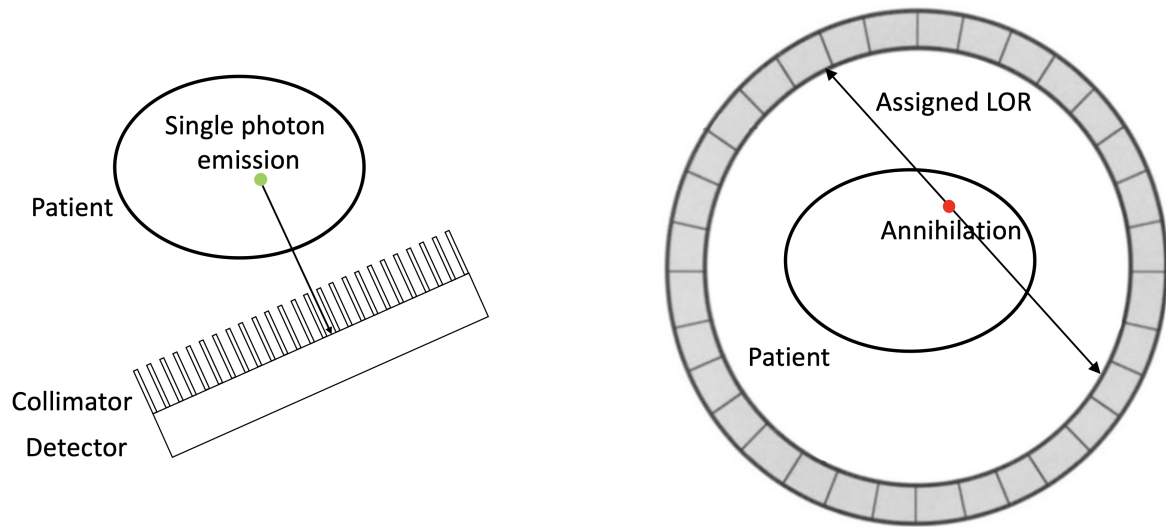
Figure 2.1: Diagram of a SPECT system with collimated detector (left) and PET system with a cylindrical ring of detectors (right)

much incentive to address the challenges of quantitative imaging of therapy radionculides. One of the challenges common to both Lu-177 and Y-90 imaging is the low intensity of the gamma-rays/photons and the corresponding low-count-rates, which will be a focus of this thesis. Enhancing direct imaging of therapy radionuclides will help to establish convincing relationships between absorbed dose and effect (response, toxicity) and enable future dosimetry guided treatment planning instead of the current aproach of using fixed or empiric actvity administration. For example, Lu-177 DOTATATE is administered to patients in four cycles with fixed activity of 7.4 GBq/cycle without consideration of the absorbed doses delivered to tumor or normal organs. With accurate and practical quantitative imaging based dosiemrty protocols, Lu-177 SPECT/CT can be performd after each cycle of therapy to plan the subsequent therapy or to determine if the next scycle is even needed.

Positron emission tomography (PET) [18] and single photon emission computed tomography (SPECT) [19] are the two main techniques of imaging and quantifying these theranostic agents [20–23]. Although PET is considered as superior to SPECT in quantitative imaging applcations due to superior spatial resolution and sensitivity, several of the radionuclides used for therapy emit gamma-rays suitable for SPECT and are not positron emitters [24]. Furthermore, SPECT is more widely available and is more economical. Hence there is value in improving both PET and SPECT imaging of therapy radionuclides. They are mainly distinguished by the decay properties of the administered radiotracer and this distinction leads to different design of hardware for each modality (PET or SPECT) to localize the tracer. SPECT is based on imaging single photons, typically gamma-rays, emitted by the radioactive material within the patient. To determine the corresponding line of response (LOR) between the detector and the point of photon emission, collimated detectors

are used as shown in Fig. 2.1. Collimators enable the detector to select the photons that travel in a specific direction, thereby reducing scatter and partially separating primary photons from secondary ones. PET uses a radiopharmaceutical labeled with a positron-emitter. At the end of its path in tissue [25] the emitted positron annihilates with a nearby electron and produces a pair of 511 keV photons (annihilation photon pair) that propagates in nearly opposite directions from each other. When the two annihilation photons are detected by two detectors in coincidence (within the narrow coincidence time window), the annihilation event is located along the path connecting the two detectors, which is the LOR. In PET, there is no need for a physical collimator as in SPECT because the detected pair of photons (that propagate in opposite directions) draws the LOR itself (Fig. 2.1). This is regarded as electronic collimation. The total number of events detected by a pair of detectors amounts to the line integral measurement and the tomographic image (spatial distribution of the radiotracer) is estimated with image reconstruction algorithm using the set of line integral measurements obtained at multiple angles. However, because of the presence of scattering and attenuation, not all the pairs of photons in PET and single photons in SPECT are correctly detected with the detectors along the LOR. Emitted photons can be absorbed within the object while the photons traverse tissue. Therefore, some photons are undetected when they are absorbed by the patient's body. Moreover, photons can also undergo Compton scattering in tissue where the traveling photon interacts with an electron. The scattered photon deviates from its original path as shown in Fig. 2.2 and loses energy. In addition to scattering and attenuating of photons, accidental (or random) coincidence (AC) events occur in PET imaging.

In a random coincidence event a photon pair produced by separate annihilation events are recorded as a 'true' coincidence event originating from the same annihilation event if the two photons are detected within the coincidence timing window. This event happens when one of the photon pair is absorbed or scattered. Those AC events can have a significant fraction in some PET scans. For example, in Y-90 patient PET imaging where the radionuclide decays mostly by beta emission, it is common that the contribution of random coincidences is more than 90% of the total detected coincidence events (random events + true events) as shown in Fig. 2.3. Bremsstrahlung photons generated by Y-90 and gamma emissions from natural radioactivity in Lu-based crystals used in some PET systems increase singles events. These singles events lead to a high percentage of randoms events and cause low signal-to-noise-ratio (SNR) measurements [20] because SNR is proportional to square root of the noise equivalent count rate (NEC) [26]:

$$\text{SNR} = c \cdot \sqrt{\text{NEC}} = c \cdot \left[\frac{T^2}{(T + S + \gamma R)} \right]^{1/2} \tag{2.1}$$

where c is a constant, T is total trues, S and R are total scatters and randoms, and γ is 1 or 2
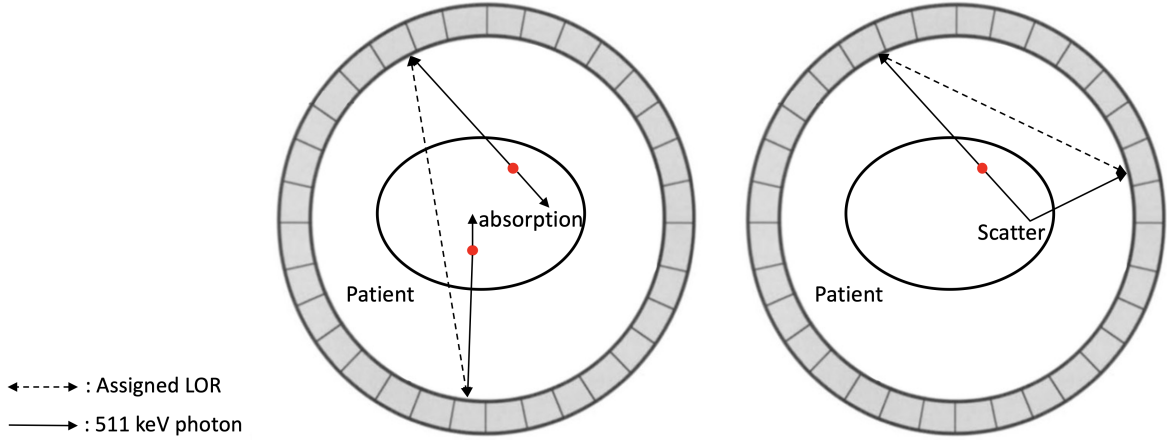
Figure 2.2: Background events in PET: random coincidence event (left) and scattered coincidence event (right).

depending on randoms estimation method.

Therefore, AC events should be estimated and compensated by accurate modeling. One available technique is using singles rates (photons per time) at detectors on LOR and the duration of coincidence timing window:

$$R_{ij} = 2\tau R_i R_j, \tag{2.2}$$

where R_{ij} is the estimated rate of AC events between detectors at ith and jth bin, and τ is duration of coincidence timing window, and R_i is singles rate at detector at ith bin. The idea behind the equation is that $2\tau R_j$ events will be detected at jth detector for the single event at ith detector.

The goal in emission tomography is to find an emission distribution $\boldsymbol{x} = (x_1, ..., x_{n_p})$ [counts] from a realization $\boldsymbol{y} = (y_1, ..., y_{n_d})$ [counts] of the projection measurement vector $\boldsymbol{Y} = (Y_1, ..., Y_{n_d})$, where n_p is the number of voxels of unknown functional image and n_d is the number of rays. Historically, before the emergence of model-based image reconstruction method [27], filtered-back-projection (FBP) method [28, 29] had been widely used because of its computational simplicity, however, it leads to unacceptable noise in emission tomography because FBP does not consider any statistical information. In contrast, statistical methods for image reconstrcution can model the physical effects in measurement accurately. In statistical model-based emission tomography, the measurement data $\boldsymbol{Y}$ are modeled as independent Poisson random variables [30] because the measurements are based on counting process [18]. Emission measurement $\boldsymbol{Y}$ follows Poisson statistical model as follows:

$$Y_i \sim \text{Poisson}\{\bar{y}_i(\boldsymbol{x}_{\text{true}})\}, \quad i = 1, ..., n_d, \tag{2.3}$$
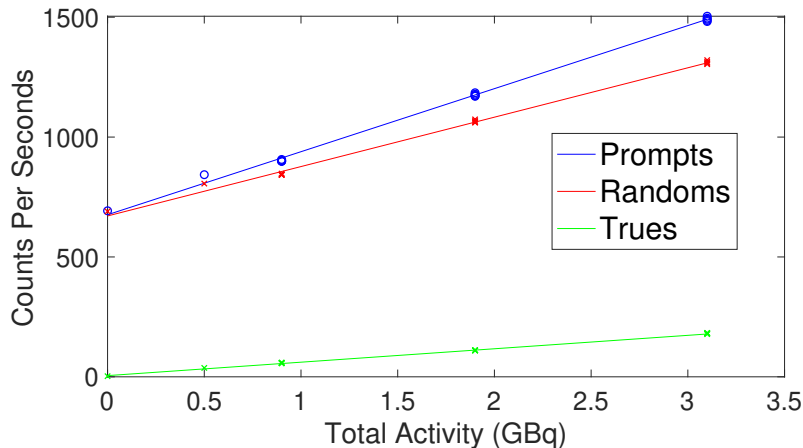
Figure 2.3: Events in Y-90 PET imaging: Very low true coincidences and high random fraction.

where $\boldsymbol{x}_{\text{true}}$ is true unknown value that we want to estimate and $\bar{y}_i(\boldsymbol{x})$ [counts] is the measurement mean:

$$\bar{y}_i(\boldsymbol{x}) = \mathrm{E}[Y_i] = \sum_{j=1}^{n_p} a_{ij} x_j + \bar{r}_i = [\boldsymbol{A}\boldsymbol{x}]_i + \bar{r}_i. \tag{2.4}$$

The matrix $\boldsymbol{A}$ denotes the system model, incorporating factors such as attenuation coefficients, where a_{ij} [unitless] is the probability that an emission from the jth voxel is recorded in the ith ray. $\bar{r}_i$ denotes the mean background events such as scatter and random coincidence for the ith ray. With the Poisson statistical model, the joint distribution of the recorded events $\boldsymbol{Y}$ is given by

$$\mathsf{P}(\boldsymbol{Y} = \boldsymbol{y}|\boldsymbol{x}) = \prod_{i=1}^{n_d} \frac{1}{y_i!} \exp\left(-\bar{y}_i(\boldsymbol{x})\right) \bar{y}_i(\boldsymbol{x})^{y_i}. \tag{2.5}$$

Taking the logarithm of $\mathsf{P}(\boldsymbol{Y} = \boldsymbol{y}|\boldsymbol{x})$ and excluding constants independent of $\boldsymbol{x}$ leads to the log-likelihood of $\boldsymbol{x}$ given $\boldsymbol{y}$. The maximum likelihood (ML) estimate $\hat{\boldsymbol{x}}$ of $\boldsymbol{x}_{\text{true}}$ is a minimizer of the Poisson negative log-likelihood $f(\boldsymbol{x})$:

$$f(\boldsymbol{x}) \overset{c}{=} \sum_{i=1}^{n_d} \mathrm{h}_i([\boldsymbol{A}\boldsymbol{x}]_i), \tag{2.6}$$

10
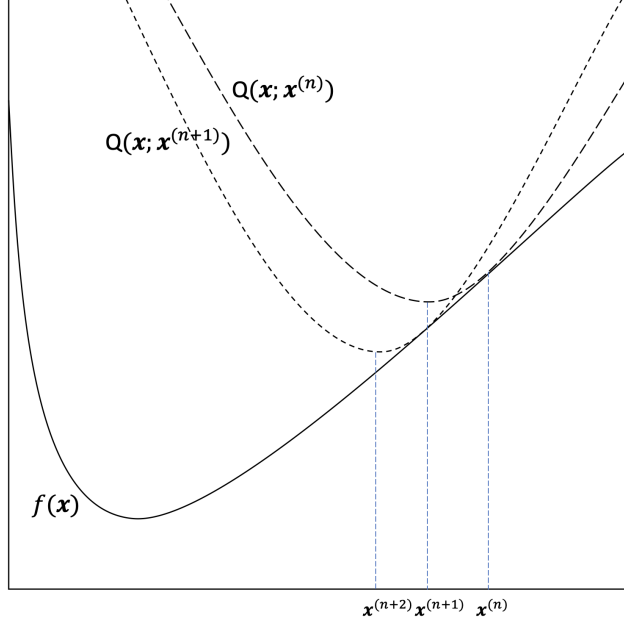
Figure 2.4: 1D illustration of optimization transfer principle.

where

$$
h_i(t) = \begin{cases} t + \bar{r}_i - y_i \log(t + \bar{r}_i), & y_i > 0, \quad t + \bar{r}_i > 0 \\ t + \bar{r}_i, & y_i = 0 \\ \infty, & y_i > 0, \quad t + \bar{r}_i \leq 0. \end{cases} \tag{2.7}
$$

Here, $\overset{c}{=}$ indicates that we exclude constants independent of $\boldsymbol{x}$. The function $h_i(t)$ is convex for $t \in (-\bar{r}_i, \infty)$. The following formulation summarizes the conventional emission tomography problem with a nonnegativity constraint:

$$
\hat{\boldsymbol{x}} = \underset{\boldsymbol{x}}{\operatorname{argmin}} \, f(\boldsymbol{x}) \tag{2.8}
$$

$$
\text{subject to } \boldsymbol{x} \geq 0. \tag{2.9}
$$

The typical approach for solving this formulation is to find a surrogate function $Q(\boldsymbol{x})$ of the log-likelihood that is easier to monotonically decrease than $f(\boldsymbol{x})$. A surrogate function $Q(\boldsymbol{x})$ should satisfy the following properties:

$$
Q(\boldsymbol{x}^{(n)}; \boldsymbol{x}^{(n)}) = f(\boldsymbol{x}^{(n)}) \tag{2.10}
$$

$$
\nabla Q(\boldsymbol{x}; \boldsymbol{x}^{(n)})|_{\boldsymbol{x}=\boldsymbol{x}^{(n)}} = \nabla f(\boldsymbol{x})|_{\boldsymbol{x}=\boldsymbol{x}^{(n)}} \tag{2.11}
$$

$$
Q(\boldsymbol{x}; \boldsymbol{x}^{(n)}) \geq f(\boldsymbol{x}). \tag{2.12}
$$

11

If $Q(\boldsymbol{x})$ satisfies above conditions, the following monotonicity condition is satisfied:

$$f(\boldsymbol{x}) - f(\boldsymbol{x}^{(n)}) \leq Q(\boldsymbol{x}; \boldsymbol{x}^{(n)}) - Q(\boldsymbol{x}^{(n)}; \boldsymbol{x}^{(n)}), \tag{2.13}$$

which ensures that updates using surrogate function monotonically decrease $f(\boldsymbol{x})$. Fig. 2.4 illustrates the principle of optimization transfer. For solving ML estimation problem, a classical reconstruction algorithm based on this optimization transfer principle is an expectation-maximization (EM) algorithm. Here, we review the derivation of EM algorithm. To start, we can generalize the observation of De Pierro [31]:

$$\bar{y}_i(\boldsymbol{x}) = [\boldsymbol{A}\boldsymbol{x}]_i + \bar{r}_i = \sum_{j=1}^{n_p} a_{ij} x_j + \bar{r}_i \tag{2.14}$$

$$= \sum_{j=1}^{n_p} \left(\frac{a_{ij} x_j^{(n)}}{\bar{y}_i^{(n)}} \right) \frac{x_j}{x_j^{(n)}} \bar{y}_i^{(n)} + \left(\frac{\bar{r}_i}{\bar{y}_i^{(n)}} \right) \bar{y}_i^{(n)}, \tag{2.15}$$

where $\bar{y}_i^{(n)} = \bar{y}_i(\boldsymbol{x}^{(n)})$. Here, we define a convex function $\mathrm{p}_i(t) = t - y_i \log t$. Because $\mathrm{p}_i(t)$ is a convex function, the Poisson negative log-likelihood $f(\boldsymbol{x})$ obeys the following inequality:

$$f(\boldsymbol{x}) = \sum_{i=1}^{n_d} \mathrm{p}_i(\bar{y}_i(\boldsymbol{x})) \tag{2.16}$$

$$= \sum_{i=1}^{n_d} \mathrm{p}_i \left(\sum_{j=1}^{n_p} \left(\frac{a_{ij} x_j^{(n)}}{\bar{y}_i^{(n)}} \right) \frac{x_j}{x_j^{(n)}} \bar{y}_i^{(n)} + \left(\frac{\bar{r}_i}{\bar{y}_i^{(n)}} \right) \bar{y}_i^{(n)} \right) \tag{2.17}$$

$$\leq Q_{\mathrm{EM}}(\boldsymbol{x}; \boldsymbol{x}^{(n)}) = \sum_{i=1}^{n_d} \sum_{j=1}^{n_p} \frac{a_{ij} x_j^{(n)}}{\bar{y}_i^{(n)}} \mathrm{p}_i \left(\frac{x_j}{x_j^{(n)}} \bar{y}_i^{(n)} \right) + \left(\frac{\bar{r}_i}{\bar{y}_i^{(n)}} \right) \mathrm{p}_i \left(\bar{y}_i^{(n)} \right) \tag{2.18}$$

$$\overset{c}{=} \sum_{j=1}^{n_p} Q_{\mathrm{EM},j}(x_j; \boldsymbol{x}^{(n)}), \tag{2.19}$$

where

$$Q_{\mathrm{EM},j}(x_j; \boldsymbol{x}^{(n)}) = \sum_{i=1}^{n_d} \frac{a_{ij} x_j^{(n)}}{\bar{y}_i^{(n)}} \left[\frac{x_j}{x_j^{(n)}} \bar{y}_i^{(n)} - y_i \log \left(\frac{x_j}{x_j^{(n)}} \bar{y}_i^{(n)} \right) \right]. \tag{2.20}$$

Inequality (2.18) holds by the following convexity inequality:

$$g \left(\sum_{k=1}^{K} \alpha_k \boldsymbol{u}_k \right) \leq \sum_{k=1}^{K} \alpha_k g \left(\boldsymbol{u}_k \right), \tag{2.21}$$

where $g(\cdot)$ is a convex function and $\alpha_k \in [0, 1]$ and $\sum_{k=1}^{K} \alpha_k = 1$. Equating $\frac{\partial Q_{\text{EM},j}(x_j; \boldsymbol{x}^{(n)})}{\partial x_j}$ to zero and enforcing the nonnegativity constraint is equivalent to following update:

$$x_j^{(n+1)} = \left[\frac{x_j^{(n)}}{a_j} e_j(\boldsymbol{x}^{(n)}) \right]_+, \tag{2.22}$$

where $e_j(\boldsymbol{x}^{(n)}) = \sum_{i=1}^{n_d} a_{ij} \frac{y_i}{\bar{y}_i(\boldsymbol{x}^{(n)})}$ and $a_j = \sum_{i=1}^{n_d} a_{ij}$.

However, the ML approach might lead to noisy image, especially in low count setting. Therefore, penalized-likelihood has been widely used to improve reconstruction quality of low-count emission tomography:

$$\hat{\boldsymbol{x}} = \arg \min_{\boldsymbol{x} \geq \boldsymbol{0}} f(\boldsymbol{x}) + \beta \mathsf{R}(\boldsymbol{x}) \tag{2.23}$$

where $\mathsf{R}(\boldsymbol{x})$ is a regularization term to control the noise and β is a regularization parameter. This regularization term can be interpreted as a *priori* information. By Bayes' theorem, a *posteriori* distribution of unknown image $\boldsymbol{x}$ with given measurement $\boldsymbol{y}$ is:

$$P(\boldsymbol{x}|\boldsymbol{y}) = \frac{P(\boldsymbol{y}|\boldsymbol{x})P(\boldsymbol{x})}{P(\boldsymbol{y})}. \tag{2.24}$$

When $P(\boldsymbol{x}) = e^{-\beta \mathsf{R}(\boldsymbol{x})}$, taking the logarithms of $-P(\boldsymbol{x}|\boldsymbol{y})$ becomes equivalent to the objective function in (2.23). Therefore, maximum *a posteriori* estimation is equivalent to penalized-likelihood reconstruction where $\mathsf{R}(\boldsymbol{x})$ is regarded as a prior information. A common choice of $\mathsf{R}(\boldsymbol{x})$ is based on proximity between nearby voxels:

$$\mathsf{R}(\boldsymbol{x}) = \sum_{k=1}^{K} \psi_k([\boldsymbol{C}\boldsymbol{x}]_k), \tag{2.25}$$

where $\boldsymbol{C}$ is a $K \times n_p$ finite differencing matrix. It is desirable for potential function ψ_k to include continuity, symmetry, and positivity [32, 33]. There are several available choices for potential function [34] and each option has its own advantage/disadvantage. In Chapter 3 and Chapter 6, we implemented a simple quadratic potential function:

$$\psi_k(t) = \frac{t^2}{2}. \tag{2.26}$$

Assuming that each ψ_k has a quadratic surrogate, following surrogate function q_k for ψ_k with

nonnegative curvature function $\check{c}_k(\cdot)$ satisfies the properties of majorization function in (2.10)-(2.12):

$$q_k(t; s) = \psi_k(s) + \dot{\psi}_k(s)(t - s) + \frac{1}{2}\check{c}_k(s)(t - s)^2. \tag{2.27}$$

To descent the cost function in (2.23) monotonically, we use optimization transfer method by finding separable quadratic surrogate (SQS) function $Q_R(\boldsymbol{x})$ for $R(\boldsymbol{x})$ as in derivation of EM algorithm. We first use (2.27) to construct a non-separable quadratic surrogate $R_Q(\boldsymbol{x}; \boldsymbol{x}^{(n)})$:

$$R(\boldsymbol{x}) = \sum_{k=1}^{K} \psi_k([\boldsymbol{C}\boldsymbol{x}]_k) \leq R_Q(\boldsymbol{x}; \boldsymbol{x}^{(n)}) = \sum_{k=1}^{K} q_k([\boldsymbol{C}\boldsymbol{x}]_k; [\boldsymbol{C}\boldsymbol{x}^{(n)}]_k). \tag{2.28}$$

Using De Pierro's additivity trick [35] $[\boldsymbol{C}\boldsymbol{x}]_k = \sum_{j=1}^{n_p} \xi_{kj}\left[\frac{c_{kj}}{\xi_{kj}}(x_j - x_j^{(n)}) + [\boldsymbol{C}\boldsymbol{x}^{(n)}]_k\right]$, where the nonnegative ξ_{kj} satisfies $\sum_{j=1}^{n_p} \xi_{kj} = 1$, $q_k([\boldsymbol{C}\boldsymbol{x}]_k; [\boldsymbol{C}\boldsymbol{x}^{(n)}]_k)$ obeys the following inequality:

$$q_k([\boldsymbol{C}\boldsymbol{x}]_k; [\boldsymbol{C}\boldsymbol{x}^{(n)}]_k) = q_k\left(\sum_{j=1}^{n_p} c_{kj}x_j; [\boldsymbol{C}\boldsymbol{x}^{(n)}]_k\right) \tag{2.29}$$

$$= q_k\left(\sum_{j=1}^{n_p} \xi_{kj}\left[\frac{c_{kj}}{\xi_{kj}}(x_j - x_j^{(n)}) + [\boldsymbol{C}\boldsymbol{x}^{(n)}]_k\right]; [\boldsymbol{C}\boldsymbol{x}^{(n)}]_k\right) \tag{2.30}$$

$$\leq \sum_{j=1}^{n_p} \xi_{kj}q_k\left(\frac{c_{kj}}{\xi_{kj}}(x_j - x_j^{(n)}) + [\boldsymbol{C}\boldsymbol{x}^{(n)}]_k; [\boldsymbol{C}\boldsymbol{x}^{(n)}]_k\right), \tag{2.31}$$

where inequality in (2.31) holds by the convexity inequality in (2.21) because q_k is convex. Therefore, the separable surrogate $Q_{R,j}(x_j; x_j^{(n)})$ for $R(\boldsymbol{x})$ is as follows:

$$R(\boldsymbol{x}) \leq R_Q(\boldsymbol{x}; \boldsymbol{x}^{(n)}) \leq R_{SQS}(\boldsymbol{x}; \boldsymbol{x}^{(n)}) = \sum_{j=1}^{n_p} Q_{R,j}(x_j; x_j^{(n)}) \tag{2.32}$$

$$= \sum_{j=1}^{n_p} \sum_{k=1}^{K} \xi_{kj}q_k\left(\frac{c_{kj}}{\xi_{kj}}(x_j - x_j^{(n)}) + [\boldsymbol{C}\boldsymbol{x}^{(n)}]_k; [\boldsymbol{C}\boldsymbol{x}^{(n)}]_k\right). \tag{2.33}$$

With separable surrogates $Q_{EM,j}$ and $Q_{R,j}$, we can monotonically decrease the cost function in

14

(2.23) by zeroing the derivative of surrogates at each iteration:

$$\frac{\partial(Q_{\text{EM},j}(x_j;\boldsymbol{x}^{(n)})) + \beta Q_{\text{R},j}(x_j;\boldsymbol{x}^{(n)}))}{\partial x_j} \tag{2.34}$$

$$= a_j - e_j\left(\boldsymbol{x}^{(n)}\right)\frac{x_j^{(n)}}{x_j} + \beta\sum_{k=1}^{K} c_{kj}\left[\dot{\psi}_k([\boldsymbol{C}\boldsymbol{x}^{(n)}]_k + \frac{c_{kj}}{\xi_{kj}}\check{c}_k([\boldsymbol{C}\boldsymbol{x}^{(n)}]_k)(x_j - x_j^{(n)})\right] \tag{2.35}$$

$$= a_j - e_j\left(\boldsymbol{x}^{(n)}\right)\frac{x_j^{(n)}}{x_j} + \beta\frac{\partial}{\partial x_j}\text{R}(\boldsymbol{x}^{(n)}) + \beta(x_j - x_j^{(n)})\sum_{k=1}^{K}\frac{c_{kj}^2}{\xi_{kj}}\check{c}_k([\boldsymbol{C}\boldsymbol{x}^{(n)}]_k). \tag{2.36}$$

Equating the derivative to zero and finding its root with respect to x_j using numerically stable method [36] leads to the following minimizer:

$$x_j^{(n+1)} = \begin{cases} \frac{\sqrt{\gamma^2+\alpha\nu}-\gamma}{\alpha}, & \alpha > 0, \gamma < 0 \\ \frac{\nu}{\sqrt{\gamma^2+\alpha\nu}+\gamma}, & \alpha > 0, \gamma \geq 0 \end{cases}, \tag{2.37}$$

where $\alpha = \beta\sum_{k=1}^{K}\frac{c_{kj}^2}{\xi_{kj}}\check{c}_k([\boldsymbol{C}\boldsymbol{x}^{(n)}]_k)$, $\gamma = \frac{1}{2}\left[a_j + \beta\frac{\partial}{\partial x_j}\text{R}(\boldsymbol{x}^{(n)}) - \beta x_j^{(n)}\sum_{k=1}^{K}\frac{c_{kj}^2}{\xi_{kj}}\check{c}_k([\boldsymbol{C}\boldsymbol{x}^{(n)}]_k)\right]$, and $\nu = e_j\left(\boldsymbol{x}^{(n)}\right)x_j^{(n)}$. A typical choice for ξ_{kj} is $\xi_{kj} = \frac{|c_{kj}|}{c_k}$, where $c_k = \sum_{j=1}^{n_p}|c_{kj}|$. With the quadratic potential function in (2.26), $\sum_{k=1}^{K}\frac{c_{kj}^2}{\xi_{kj}}\check{c}_k([\boldsymbol{C}\boldsymbol{x}^{(n)}]_k) = \sum_{k=1}^{K}|c_{kj}|c_k$ and $\frac{\partial}{\partial x_j}\text{R}(\boldsymbol{x}^{(n)}) = \sum_{k=1}^{K}c_{kj}\left(\sum_{j=1}^{n_p}c_{kj}x_j^{(n)}\right)$. Chapter 5 and 6 use modifications of this type of majorizer and EM algorithm for image reconstruction.

However, using such "hand-crafted" regularization as in (2.25) that is mostly based on proximity between neighboring pixels is unlikely to be the best approach because the designed prior information (smoothness) is not necessarily true in all regions of interest, especially in the region where a sharp edge exists. A recent trend is to unroll an iterative algorithm for solving an optimization problem having a cost function that consists of data fidelity term and regularization term and learn the trainable parameters (mostly associated with regularization term) from a training dataset. Applying such "learned" regularizers to model-based image reconstruction significantly improved image quality and quantification in medical image reconstruction with application of CT [37–39], MRI [40,41], and emission tomography [42,43] compared to "mathematically designed" (or hand-crafted) regularizers. One specific form of trained regularizer shown in [41] is as follows:

$$\text{R}(\boldsymbol{x}) = \sum_{k=1}^{K}\Phi_k\left(\boldsymbol{c}_k * \boldsymbol{x}\right), \tag{2.38}$$

where $\{\boldsymbol{c}_k\}$ are convolutional filters and $\{\Phi_k(\cdot)\}$ are non-linear potential functions. [41] unrolled a gradient descent scheme for a cost function that includes $\text{R}(\boldsymbol{x})$ in (2.38) and trained a parameter

$\lambda^{(n)}$ at each iteration that considers step size of update for data-fit term as follows:

$$\boldsymbol{x}^{(n+1)} = \boldsymbol{x}^{(n)} - \left(\sum_{k=1}^{K} \tilde{\boldsymbol{c}}_k^{(n)} * \Phi_k' \left(\boldsymbol{c}_k^{(n)} * \boldsymbol{x}^{(n)} \right) + \lambda^{(n)} \nabla f \left(\boldsymbol{x}^{(n)} \right) \right), \quad n = 0, \dots, N-1, \quad (2.39)$$

where $f(\boldsymbol{x})$ is a data-fit term, N is a total number of iterations, $\boldsymbol{c}_k^{(n)}$ is a trained convolutional filter for nth iteration, $\tilde{\boldsymbol{c}}_k^{(n)}$ is rotated $\boldsymbol{c}_k^{(n)}$ by 180°, and $\{\Phi_k'(\cdot)\}$ are derivative of potential functions. [41] used Gaussian radial basis functions [44] for $\{\Phi_k'(\cdot)\}$. The trainable parameters at each iteration $\boldsymbol{\theta}^{(n)}$ ($\{\boldsymbol{c}_k^{(n)}\}$, $\lambda^{(n)}$, parameters in $\{\Phi_k'^{(n)}(\cdot)\}$) can be trained using mean squared error loss function that measures the average squared difference between final estimated image and ground truth image:

$$L(\boldsymbol{\theta}) = \frac{1}{2S} \sum_{s=1}^{S} \left\| \boldsymbol{x}_s^{(N)} - \boldsymbol{g}_s \right\|_2^2, \quad (2.40)$$

where $\boldsymbol{\theta} = \boldsymbol{\theta}^{(0)}, \dots, \boldsymbol{\theta}^{(N-1)}$ is a set of parameters, $\boldsymbol{g}$ is a ground truth image, and S is a total number of training samples. Parameters at nth iteration can be updated using back-propagation algorithm [45] that applies chain-rule:

$$\frac{\partial L(\boldsymbol{\theta})}{\partial \boldsymbol{\theta}^{(n)}} = \frac{\partial \boldsymbol{x}^{(n+1)}}{\partial \boldsymbol{\theta}^{(n)}} \cdot \frac{\partial \boldsymbol{x}^{(n+2)}}{\partial \boldsymbol{x}^{(n+1)}} \cdots \frac{\partial \boldsymbol{x}^{(N)}}{\partial \boldsymbol{x}^{(N-1)}} \cdot \frac{\partial L(\boldsymbol{\theta})}{\partial \boldsymbol{x}^{(N)}} \quad (2.41)$$

$$\boldsymbol{\theta}^{(n)} := \boldsymbol{\theta}^{(n)} - \alpha \frac{\partial L(\boldsymbol{\theta})}{\partial \boldsymbol{\theta}^{(n)}}, \quad (2.42)$$

where α is learning rate that controls a step size of the update. Training all the trainable parameters with a single loss function as in (2.40)-(2.42) has been widely used in MRI community because MRI measurement is samples of simple fast Fourier tranform (FFT) of object's magnetization. However, in emission tomography, this training scheme is implementation-wise difficult because of computationally expensive forward and back-projections and limited capacity of GPU memory for fully 3D measurement (even 4D in time of flight information PET) [46]. As an alternative solution, parameters are trained iteration-by-iteration with loss function defined at each iteration:

$$L(\boldsymbol{\theta}^{(n)}) = \frac{1}{2S} \sum_{s=1}^{S} \left\| \boldsymbol{x}_s^{(n)} - \boldsymbol{g}_s \right\|_2^2 \quad (2.43)$$

$$\boldsymbol{\theta}^{(n)} := \boldsymbol{\theta}^{(n)} - \alpha \frac{\partial L(\boldsymbol{\theta}^{(n)})}{\partial \boldsymbol{\theta}^{(n)}}. \quad (2.44)$$

Chapter 5 and 6 use this type of training scheme and comparing it to training all parameters using single loss (end-to-end) is one of future directions of those chapters. Some studies used a trained neural network in image space without exploiting the physical imaging model. In this

case, training using end-to-end approach is feasible. For example, [47] applied a deep neural network mapping between reconstructed PET images with normal dose and reduced dose and [48] applied a multilayer perceptron mapping between reconstructed images using maximum a posteriori algorithm and a reference (true) image. However, that framework uses the acquisition data only to form the initial image, therefore, the reconstruction quality depends greatly on the training dataset and information from atypical imaging situations (that are not part of the training set) may not be recovered well, especially when the training dataset size is small [11].

CHAPTER 3

Reducing Bias in Y-90 PET Images by Enforcing Non-Negativity in Projection Space

Most existing PET image reconstruction methods impose a nonnegativity constraint in the image domain that is natural physically, but can lead to biased reconstructions. This bias is particularly problematic for Y-90 PET because of the low probability positron production and high random coincidence fraction. This chapter investigates a new PET reconstruction formulation that enforces nonnegativity of the projections instead of the voxel values. This formulation allows some negative voxel values, thereby potentially reducing bias. Unlike the previously reported related works that modifies the Poisson log-likelihood to allow negative values, the new formulation retains the classical Poisson statistical model. To relax the non-negativity constraint embedded in the standard methods for PET reconstruction, we used an Alternating Direction Method of Multipliers (ADMM). Because choice of ADMM parameters can greatly influence convergence rate, we applied an automatic parameter selection method to improve the convergence speed. We investigated the methods using lung to liver slices of XCAT phantom [5, 7]. We simulated low true coincidence count-rates with high random fractions corresponding to the typical values from patient imaging in Y-90 microsphere radioembolization. The new formulation was also tested on patient and phantom PET measurements (time-of-flight) and demonstrated improved contrast recovery [6] and the new method outperformed conventional EM reconstruction available in the clinic. This study was performed with the collaboration of the Siemens PET Physics Division that provided us access to their TOF projector to implement our reconstruction with real data from the clinic PET system.

3.1 Introduction

Interest in quantitative imaging of Y-90 is growing because transarterial radioembolization (RE) with Y-90 loaded microspheres is a promising and minimally invasive treatment that is FDA approved for unresectable primary and metastatic liver tumors. These cancers are a leading cause of cancer mortality and morbidity. Radioembolization is a therapy that irradiates liver tumors

---

This chapter is based on [5–7].
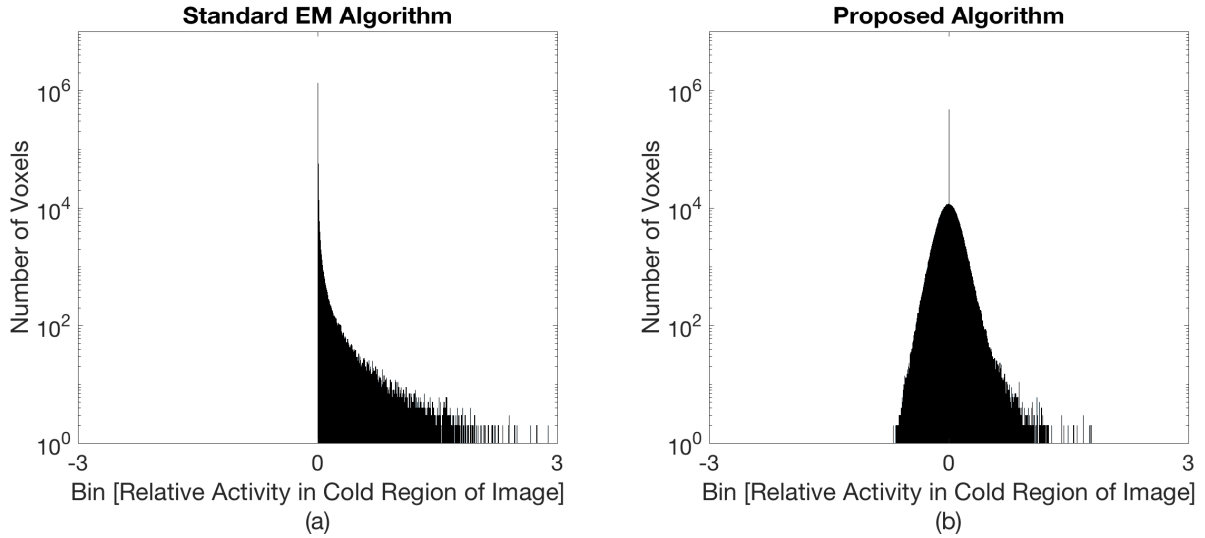
Figure 3.1: Reconstruction results when simulating realistic conditions of low count rates: (a) A histogram showing how the standard reconstruction algorithm (EM) can have a positive bias in the cold regions in the setting of lower count-rates. Cold region refers to the outside of liver where the true image has no counts. An example slice of the true image is shown in Fig. 3.3. (b) A histogram illustrating how the proposed method avoids the positive bias by allowing negative values.

with radioactive microspheres administered through a microcatheter placed in the hepatic arterial vasculature. Radioembolization is based on the principle that healthy liver and tumor are mainly vascularized by the portal vein and the hepatic artery respectively [49]. As a result, radioactive microspheres are preferentially located in the lesions after they are administered via the hepatic artery.

Accurate quantitative Y-90 imaging based dosimetry is important for establishing absorbed dose versus outcome relationships for developing future treatment planning strategies in radioembolization. Additionally, accurately assessing the microsphere distribution is important for finding unexpected extra-hepatic deposition. However, imaging of Y-90 is complex as it is an almost pure beta emitter, with no associated gamma-rays. As shown in Fig. 3.2, a very small portion of Y-90 decays to an exited state of Z-90 and the following de-excitation leads to a positron emission [50]. Therefore, Y-90 imaging involves PET via very low probability ($\sim 3.2 \times 10^{-5}$) positrons in the presence of increased singles events from bremsstrahlung photons [51] and gammas from natural radioactivity in Lu-based crystals used in some PET systems. Due to these attributes of Y-90, positive bias in cold regions and underestimation in regions of interest are reported in many Y-90 PET papers [20–22]. Those reports conclude that the bias is introduced by the current standard PET reconstruction algorithms that enforce a nonnegativity constraint in the image domain. Fig. 3.1(a) illustrates how the standard expectation maximization (EM) image reconstruction algorithm generates positive bias in a low count-rate setting.
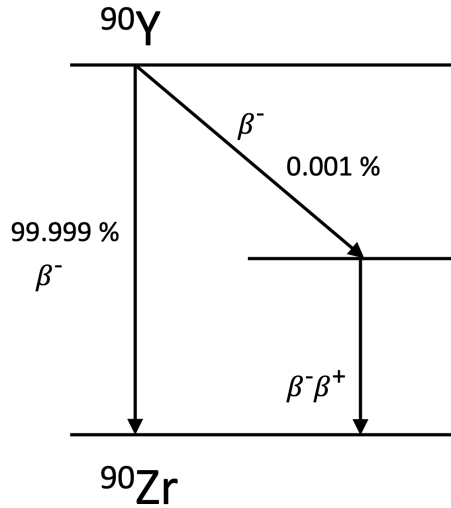
Figure 3.2: Y-90 decay scheme

Recent studies have demonstrated improved Y-90 PET imaging with time-of-flight (TOF) information and acquisitions that allow for randoms smoothing [4]. However, quantitative imaging under the low count-rates typical for Y-90 PET remains challenging. Though not specific to Y-90, others have previously proposed reconstruction algorithms to mitigate the bias issue in low-statistics PET/SPECT. AB-EMML (AB-expectation maximization maximum likelihood) [52] was devised for the deblurring problem, however, [53] used this method for low count-rate scans because AB-EMML allows negative values when the lower boundary is set below 0. NEG-ML [54] was introduced for non-attenuation corrected PET, but it was also shown to be effective to reduce the bias [55]. A modified version of NEG-ML was introduced in [56] that includes two factors giving more flexibility for Gaussian distribution switching point and allowing faster convergence.

Both the AB-EMML and the NEG-ML approaches use modifications of the log-likelihood for Poisson data. Because ML estimation (based on the correct statistical model) is known to be asymptotically efficient (lowest possible variance), modifying the log-likelihood may affect image noise properties and the modifications require additional parameters to tune. Our objective is similar to these previous works, namely reducing the bias observed in low statistics PET, especially for Y-90 PET. However, our proposed algorithm is distinct in avoiding modifying or approximating the Poisson log-likelihood used in the data fit term. We propose a method to relax the conventional image-domain nonnegativity constraint by instead imposing a positivity constraint on the predicted measurement mean. We adopt ADMM to perform reconstruction that enforces this constraint. Fig. 3.1(b) demonstrates how the proposed method overcomes the positive bias evident in Fig. 3.1(a).

Section 3.2 presents the formulation of our proposed PET reconstruction algorithm and reviews how the update in various algorithms changes when the cost function includes a regularization

term. Section 3.3 explains the simulation method in the setting of Y-90 radioembolization and the evaluation metrics used for the quantification assessment. Section 3.4 investigates how the various reconstruction methods work when the number of projection angles replicates 3D and fully 3D PET and examines the impact of parameter selection. Section 3.5 discusses the strengths and limitations of each method.

3.2   Methods

This section reviews a standard reconstruction method in emission tomography. Then we explain how we formulate a new constrained reconstruction approach and we present various methods that incorporate regularization.

3.2.0.1   SPS algorithm

The maximum likelihood (ML) estimate $\hat{x}$ of x_{true} minimizes the Poisson negative log-likelihood $f(x)$ for measurement y and estimated measurement means $\bar{y}(x)$:

$$f(x) \overset{c}{=} \sum_{i=1}^{n_d} \mathsf{q}_i([Ax]_i), \tag{3.1}$$

where

$$\mathsf{q}_i(t) = \begin{cases} t + \bar{r}_i - y_i \log(t + \bar{r}_i), & y_i > 0, \quad t + \bar{r}_i > 0 \\ t + \bar{r}_i, & y_i = 0 \\ \infty, & y_i > 0, \quad t + \bar{r}_i \leq 0. \end{cases} \tag{3.2}$$

x is unknown image that we want to estimate and $\bar{y}_i(x)$ [counts] is the measurement mean:

$$\bar{y}_i(x) = [Ax]_i + \bar{r}_i, \tag{3.3}$$

where the matrix A denotes the system model and $\bar{r}_i$ denotes the mean background events such as scatter and random coincidence. The typical approach for solving this formulation is to find a surrogate function $Q(x)$ of the log-likelihood that is easier to monotonically decrease than $f(x)$. The separable paraboloidal surrogate (SPS) algorithm for (2.8) uses a quadratic majorizer for $f(x)$ and updates x_j by minimizing the separable surrogate function $Q_{\text{SPS},j}$ using Newton's method:

$$x_j^{(n+1)} = \left[x_j^{(n)} - \frac{\left. \frac{\partial Q_{\text{SPS},j}(x_j;x^{(n)})}{\partial x_j} \right|_{x_j=x_j^{(n)}}}{\frac{\partial^2 Q_{\text{SPS},j}(x_j;x^{(n)})}{\partial x_j^2}} \right]_+, \tag{3.4}$$

where $[.]_+$ enforces the voxel nonnegativity constraint and (see [57]):

$$Q_{\text{SPS},j}(x_j; \boldsymbol{x}^{(n)}) \overset{c}{=} \sum_{i=1}^{n_d} \left(a_{ij}(1 - \frac{y_i}{\bar{y}_i^{(n)}})(x_j - x_j^{(n)}) + \frac{\check{c}_i^{(n)} a_i}{2}(x_j - x_j^{(n)})^2 \right) \tag{3.5}$$

$$\frac{\partial Q_{\text{SPS},j}(x_j; \boldsymbol{x}^{(n)})}{\partial x_j}\Big|_{x_j = x_j^{(n)}} = \sum_{i=1}^{n_d} \left(1 - \frac{y_i}{\bar{y}_i^{(n)}} \right) a_{ij} = \frac{\partial f(\boldsymbol{x}^{(n)})}{\partial x_j} \tag{3.6}$$

$$\frac{\partial^2 Q_{\text{SPS},j}(x_j; \boldsymbol{x}^{(n)})}{\partial x_j^2} = \sum_{i=1}^{n_d} \check{c}_i^{(n)} a_{ij} a_i \tag{3.7}$$

$$\check{c}_i^{(n)} = \frac{2}{(l_i^{(n)})^2} \left[l_i^{(n)} \dot{\mathsf{q}}_i(l_i^{(n)}) + \mathsf{q}_i(0) - \mathsf{q}_i(l_i^{(n)}) \right], \tag{3.8}$$

$\bar{y}_i^{(n)}$ denotes $\bar{y}_i(\boldsymbol{x}^{(n)})$ and $\boldsymbol{x}^{(n)}$ is the estimated $\boldsymbol{x}$ at the nth iteration. $l_i^{(n)}$ and a_i denote $[\boldsymbol{A}\boldsymbol{x}^{(n)}]_i$ and $\sum_{j=1}^{n_p} a_{ij}$ respectively. Considerations on the condition of $\bar{\boldsymbol{r}}$ ($\bar{r}_i > 0$), choosing the optimal curvature $\check{c}_i^{(n)}$ and deriving separable surrogate function are shown in [58] and [33]. The matrix-vector form of (3.4)-(3.7) is

$$\boldsymbol{x}^{(n+1)} = \left[\boldsymbol{x}^{(n)} - \left(\boldsymbol{D}^{(n)} \right)^{-1} \nabla f(\boldsymbol{x}^n) \right]_+, \tag{3.9}$$

where $\boldsymbol{D}^{(n)}$ is a diagonal matrix with diagonal elements $A^T \text{diag}\{\check{c}_i^{(n)}\} A \mathbf{1}$ where $\mathbf{1}$ denotes the vector of ones of length n_p and ∇f is in (3.6).

3.2.0.2 NEG-ML algorithm

The approach of NEG-ML algorithm is similar to the SPS algorithm in that is uses a quadratic majorizer of the data fit term. However, NEG-ML minimizes a modified data fit term $f_{\text{NEG-ML}}(\boldsymbol{x})$ where the Poisson distribution is replaced by Gaussian distribution when the estimated measurement is below than the parameter ψ:

$$f_{\text{NEG-ML}}(\boldsymbol{x}) \overset{c}{=} \sum_{i=1}^{n_d} \tilde{\mathsf{q}}_i([\boldsymbol{A}\boldsymbol{x}]_i), \tag{3.10}$$

where

$$\tilde{\mathsf{q}}_i(t) = \begin{cases} t + \bar{r}_i - y_i \log(t + \bar{r}_i), & t + \bar{r}_i \geq \psi \\ \frac{(y_i - t - \bar{r}_i)^2}{2\psi} - y_i \log \psi + \psi - \frac{(y_i - \psi)^2}{2\psi}, & t + \bar{r}_i < \psi. \end{cases} \tag{3.11}$$

Minimizing a separable surrogate function of (3.11) using Newton's method leads to the following NEG-ML iteration:

$$x_j^{(n+1)} = x_j^{(n)} - \frac{\sum_{i=1}^{n_d} a_{ij} \frac{\bar{y}_i^{(n)} - y_i}{\max(\psi, \bar{y}_i^{(n)})}}{\sum_{i=1}^{n_d} a_{ij} \frac{a_i}{\max(\psi, \bar{y}_i^{(n)})}}. \tag{3.12}$$

Derivation details are shown in [59].

3.2.1 Proposed formulation

As shown in previous section, the standard methods for reconstructing emission images are based on nonnegativity constraint in image domain: $\boldsymbol{x} \geq 0$. This is a natural constraint as the activity distribution cannot have negative values physically. However, this constraint can cause positive biases in regions of low or no activity, especially when the measured counts are low and the background events $\bar{r}_i$ are dominant.

To loosen the nonnegativity constraint in hope of reducing the positive bias, We propose to allow negative values in image domain while keeping positivity in projection space. We propose the following formulation:

$$\hat{\boldsymbol{x}} = \underset{\boldsymbol{x}}{\operatorname{argmin}} f(\boldsymbol{x}), \quad \text{subject to } \boldsymbol{A}\boldsymbol{x} + \bar{\boldsymbol{r}} > 0. \tag{3.13}$$

The constraint $\boldsymbol{A}\boldsymbol{x} + \bar{\boldsymbol{r}} > 0$ is reasonable because likelihood function $f(\boldsymbol{x})$ includes $\log(\boldsymbol{A}\boldsymbol{x} + \bar{\boldsymbol{r}})$ and the argument of a logarithm should be positive. We rewrite this optimization problem in the following unconstrained composite formulation:

$$\hat{\boldsymbol{x}} = \underset{\boldsymbol{x} \in \mathbb{R}^{n_p}}{\operatorname{argmin}} f(\boldsymbol{x}) + g(\boldsymbol{A}\boldsymbol{x} + \bar{\boldsymbol{r}}), \tag{3.14}$$

where

$$g(\eta_i) = \begin{cases} \infty, & y_i > 0, \ \eta_i < 0 \\ 0, & \text{else} \end{cases} \tag{3.15}$$

$$g(\boldsymbol{\eta}) = \sum_{i=1}^{n_d} g_i(\eta_i) \tag{3.16}$$

for a vector argument $\boldsymbol{\eta} \in \mathbb{R}^{n_d}$. To perform this minimization, we introduce an auxiliary variable $\boldsymbol{v}$

leading to the following equality constrained optimization problem:

$$\hat{\boldsymbol{x}} = \operatorname*{argmin}_{\boldsymbol{x} \in \mathbb{R}^{np}} \min_{\boldsymbol{v} \in \mathbb{R}^{n_d}} \mathbf{1}^T(\boldsymbol{v} + \bar{\boldsymbol{r}}) - \boldsymbol{y}^T \log(\boldsymbol{v} + \bar{\boldsymbol{r}}) + g(\boldsymbol{v} + \bar{\boldsymbol{r}}) \tag{3.17}$$

$$\text{subject to } \boldsymbol{v} = \boldsymbol{A}\boldsymbol{x}. \tag{3.18}$$

We form an augmented Lagrangian based on that formulation:

$$\Psi(\boldsymbol{x}, \boldsymbol{v}, \boldsymbol{\lambda}) = \mathbf{1}^T(\boldsymbol{v} + \bar{\boldsymbol{r}}) - \boldsymbol{y}^T \log(\boldsymbol{v} + \bar{\boldsymbol{r}}) + g(\boldsymbol{v} + \bar{\boldsymbol{r}}) + \boldsymbol{\lambda}^T(\boldsymbol{A}\boldsymbol{x} - \boldsymbol{v}) + \frac{\rho}{2}\|\boldsymbol{A}\boldsymbol{x} - \boldsymbol{v}\|_2^2, \tag{3.19}$$

where $\boldsymbol{\lambda}$ is a dual variable and $\rho > 0$ is called the penalty parameter and it affects the convergence rate but not the final minimum. Letting $\boldsymbol{d} = \boldsymbol{A}\boldsymbol{x} - \boldsymbol{v}$, $\boldsymbol{u} = \frac{\boldsymbol{\lambda}}{\rho}$, we rewrite $\boldsymbol{\lambda}^T(\boldsymbol{A}\boldsymbol{x} - \boldsymbol{v}) + \frac{\rho}{2}\|\boldsymbol{A}\boldsymbol{x} - \boldsymbol{v}\|_2^2$ in a simpler form:

$$\begin{aligned}
\boldsymbol{\lambda}^T(\boldsymbol{A}\boldsymbol{x} - \boldsymbol{v}) + \frac{\rho}{2}\|\boldsymbol{A}\boldsymbol{x} - \boldsymbol{v}\|_2^2 &= \boldsymbol{\lambda}^T \boldsymbol{d} + \frac{\rho}{2}\|\boldsymbol{d}\|_2^2 \\
&= \frac{\rho}{2}\|\boldsymbol{d} + \frac{\boldsymbol{\lambda}}{\rho}\|_2^2 - \frac{1}{2\rho}\|\boldsymbol{\lambda}\|_2^2 \\
&= \frac{\rho}{2}\|\boldsymbol{A}\boldsymbol{x} - \boldsymbol{v} + \boldsymbol{u}\|_2^2 - \frac{\rho}{2}\|\boldsymbol{u}\|_2^2. \tag{3.20}
\end{aligned}$$

Then the augmented Lagrangian becomes the following equivalent expression:

$$\Psi(\boldsymbol{x}, \boldsymbol{v}, \boldsymbol{u}) = \mathbf{1}^T(\boldsymbol{v} + \bar{\boldsymbol{r}}) - \boldsymbol{y}^T \log(\boldsymbol{v} + \bar{\boldsymbol{r}}) + g(\boldsymbol{v} + \bar{\boldsymbol{r}}) + \frac{\rho}{2}\|\boldsymbol{A}\boldsymbol{x} - \boldsymbol{v} + \boldsymbol{u}\|_2^2 - \frac{\rho}{2}\|\boldsymbol{u}\|_2^2. \tag{3.21}$$

Finding the saddle point of (3.21) is equivalent to solving the problem (3.17)-(3.18):

$$\hat{\boldsymbol{x}} = \operatorname*{argmin}_{\boldsymbol{x} \in \mathbb{R}^{np}} \min_{\boldsymbol{v} \in \mathbb{R}^{n_d}} \max_{\boldsymbol{u} \in \mathbb{R}^{n_d}} \Psi(\boldsymbol{x}, \boldsymbol{v}, \boldsymbol{u}). \tag{3.22}$$

ADMM [60] approaches the saddle point of the augmented Lagrangian function by updating variables $\boldsymbol{x}, \boldsymbol{v}, \boldsymbol{u}$ in the following sequential way:

$$\boldsymbol{x}^{(n+1)} = \operatorname*{argmin}_{\boldsymbol{x}} \frac{\rho}{2}\|\boldsymbol{A}\boldsymbol{x} - \boldsymbol{v}^{(n)} + \boldsymbol{u}^{(n)}\|_2^2 \tag{3.23}$$

$$\boldsymbol{v}^{(n+1)} = \operatorname*{argmin}_{\boldsymbol{v}} \left(\mathbf{1}^T(\boldsymbol{v} + \bar{\boldsymbol{r}}) - \boldsymbol{y}^T \log(\boldsymbol{v} + \bar{\boldsymbol{r}}) + g(\boldsymbol{v} + \bar{\boldsymbol{r}}) + \frac{\rho}{2}\|\boldsymbol{A}\boldsymbol{x}^{(n+1)} - \boldsymbol{v} + \boldsymbol{u}^{(n)}\|_2^2 \right) \tag{3.24}$$

$$\boldsymbol{u}^{(n+1)} = \boldsymbol{u}^{(n)} + (\boldsymbol{A}\boldsymbol{x}^{(n+1)} - \boldsymbol{v}^{(n+1)}). \tag{3.25}$$

In the implementation, we initialize $\boldsymbol{v}^{(0)} = \boldsymbol{A}\boldsymbol{x}^{(0)}$ and $\boldsymbol{u}^{(0)} = \boldsymbol{0}$. ADMM is an extension of the method of multipliers algorithm where (3.23), (3.24) can be viewed as a finding primal optimal

points in a sequential fashion and (3.25) as finding a dual optimal point.

3.2.1.1 x − update

An established minimization method to solve the quadratic problem in (3.23) is the conjugate gradient (CG) algorithm. In our implementation, we used just one iteration of CG, which is equivalent to one iteration of steepest descent (SD):

$$g^{(n)} = \rho A^T (Ax^{(n)} - v^{(n)} + u^{(n)}) \tag{3.26}$$

$$\zeta_n = \frac{||g^{(n)}||^2}{\rho ||Ag^{(n)}||^2} \tag{3.27}$$

$$x^{(n+1)} = x^{(n)} - \zeta_n g^{(n)}. \tag{3.28}$$

3.2.1.2 v − update

For the v-update, we first find the minimizer $\hat{v}$ of (3.24) excluding the $g(v + \bar{r})$ term using its separability:

$$\mathbf{1}^T(v + \bar{r}) - y^T \log(v + \bar{r}) + \frac{\rho}{2}||Ax^{(n+1)} - v + u^{(n)}||_2^2 \tag{3.29}$$

$$= \sum_{i=1}^{n_d} \left(v_i + \bar{r}_i - y_i \log(v_i + \bar{r}_i) + \frac{\rho}{2}([Ax^{(n+1)}]_i - v_i + u_i^{(n)})^2 \right) = \sum_{i=1}^{n_d} k(v_i). \tag{3.30}$$

Zeroing the derivative of $k(v_i)$ and finding the root leads to the minimizer:

$$\hat{v}_i = \begin{cases} [Ax^{(n+1)}]_i + u_i^{(n)} - \frac{1}{\rho}, & y_i = 0 \\ \sqrt{\beta^2 + \gamma} - \beta, & y_i > 0, \ \beta < 0 \\ \frac{\nu}{\sqrt{\beta^2 + \gamma} + \beta}, & y_i > 0, \ \beta \geq 0, \end{cases} \tag{3.31}$$

where

$$\beta = \frac{1}{2}(\frac{1}{\rho} + \bar{r}_i - u_i^{(n)} - [Ax^{(n+1)}]_i) \tag{3.32}$$

$$\gamma = \bar{r}_i(u_i^{(n)} + [Ax^{(n+1)}]_i) - \frac{\bar{r}_i - y_i}{\rho}. \tag{3.33}$$

Lastly, we consider $g(v + \bar{r})$ constraint, leading to the final v update:

$$v_i^{(n+1)} = [\hat{v}_i + \bar{r}_i]_+ - \bar{r}_i. \tag{3.34}$$

Note that both (3.32) and (3.26) require computing $\boldsymbol{A}\boldsymbol{x}^{(n)}$ so an efficient implementation saves this product so only one new forward project per iteration is needed.

3.2.1.3 Parameter ρ selection

Manually selecting parameter ρ of ADMM algorithm often leads to slow convergence. [60] introduced an approach to adaptively tune the parameter by comparing the primal and dual residual. We followed the comparison criteria choice in [60].

3.2.2 Regularization

We also derived and implemented algorithms for minimizing cost functions that include a regularization term $\mathsf{R}(\boldsymbol{x})$ to penalize the image roughness and control noise:

$$\mathsf{R}(\boldsymbol{x}) = \sum_{k=1}^{K} \psi_k([\boldsymbol{C}\boldsymbol{x}]_k), \tag{3.35}$$

where $\boldsymbol{C}$ is a $K \times n_p$ finite differencing matrix. It is preferable for potential function ψ_k to include continuity, symmetry, and positivity [61]. There are several available choices for potential function and each option has its own advantage/disadvantage. For the results in this paper, we used a simple quadratic potential function:

$$\psi(t) = \frac{t^2}{2}. \tag{3.36}$$

We designed $\boldsymbol{C}$ to generate finite differences in 3-dimensions. Including a regularization term in the cost function for emission tomography leads to the following minimization problems:

$$\hat{\boldsymbol{x}} = \underset{\boldsymbol{x}}{\mathrm{argmin}}\, f(\boldsymbol{x}) + \beta \mathsf{R}(\boldsymbol{x}) \tag{3.37}$$

$$\text{subject to } \boldsymbol{A}\boldsymbol{x} + \bar{\boldsymbol{r}} \geq 0 \text{ (proposed)} \tag{3.38}$$

$$\text{or } \boldsymbol{x} \geq 0 \text{ (conventional)}, \tag{3.39}$$

where β is a parameter specifying how much we want to penalize the roughness. The following subsections briefly list solutions to (3.37) - (3.39) with the various approaches.

3.2.2.1 Regularized SPS algorithm

Finding optimal $\boldsymbol{x}$ for (3.37) with the standard constraint $\boldsymbol{x} \geq 0$ is an extension of the SPS algorithm. We used the standard separable surrogate function $Q_{\mathsf{R},j}$ for $\beta\mathsf{R}(\boldsymbol{x})$ [35]:

$$Q_{\mathsf{R},j}(x_j; x^{(n)}) \overset{c}{=} \beta \sum_{k=1}^{K} \left(c_{kj}[\boldsymbol{C}\boldsymbol{x}^{(n)}]_k(x_j - x_j^{(n)}) + \frac{1}{2}|c_{kj}|c_k(x_j - x_j^{(n)})^2 \right), \tag{3.40}$$

$$x_j^{(n+1)} = \left[x_j^{(n)} - \frac{\frac{\partial Q_{\mathsf{SPS},j}(x_j;\boldsymbol{x}^{(n)})}{\partial x_j}\big|_{x_j=x_j^{(n)}} + \frac{\partial Q_{\mathsf{R},j}(x_j;\boldsymbol{x}^{(n)})}{\partial x_j}\big|_{x_j=x_j^{(n)}}}{\frac{\partial^2 Q_{\mathsf{SPS},j}(x_j;\boldsymbol{x}^{(n)})}{\partial x_j^2} + \frac{\partial^2 Q_{\mathsf{R},j}(x_j;\boldsymbol{x}^{(n)})}{\partial x_j^2}} \right]_+ \tag{3.41}$$

$$= \left[x_j^{(n)} - \frac{\sum_{i=1}^{n_d} \left(1 - \frac{y_i}{\bar{y}_i^{(n)}}\right)a_{ij} + \beta \sum_{k=1}^{K} c_{kj}[\boldsymbol{C}\boldsymbol{x}^{(n)}]_k}{\sum_{i=1}^{n_d} \breve{c}_i^{(n)} a_{ij} a_i + \beta \sum_{k=1}^{K} |c_{kj}|c_k} \right]_+, \tag{3.42}$$

where c_k denotes $\sum_{j=1}^{n_p} |c_{kj}|$.

3.2.2.2 Regularized NEG-ML

NEG-ML also use the quadratic majorizer of the modified likelihood function; therefore, the scheme for $\boldsymbol{x}$-update of regularized NEG-ML is analogous to regularized SPS algorithm:

$$x_j^{(n+1)} = x_j^{(n)} - \frac{\sum_{i=1}^{n_d} a_{ij} \frac{\bar{y}_i^{(n)} - y_i}{\max(\psi, \bar{y}_i^{(n)})} + \beta \sum_{k=1}^{K} c_{kj}[\boldsymbol{C}\boldsymbol{x}^{(n)}]_k}{\sum_{i=1}^{n_d} a_{ij} \frac{a_i}{\max(\psi, \bar{y}_i^{(n)})} + \beta \sum_{k=1}^{K} |c_{kj}|c_k}, \tag{3.43}$$

where ψ is a parameter indicating the likelihood function switching point between the Poisson distribution and the Gaussian distribution. We set the convergence-related step-size as 1 in our implementation.

3.2.2.3 Proposed algorithm with regularization

Including $\mathsf{R}(\boldsymbol{x})$ in the cost function requires only modifications to (3.21) and (3.26)-(3.27) for the $\boldsymbol{x}$-update in Section 3.2.1.1:

$$\Psi(\boldsymbol{x}, \boldsymbol{v}, \boldsymbol{u}) = \boldsymbol{1}^T(\boldsymbol{v} + \bar{\boldsymbol{r}}) - \boldsymbol{y}^T \log(\boldsymbol{v} + \bar{\boldsymbol{r}}) + \beta\mathsf{R}(\boldsymbol{x}) + g(\boldsymbol{v} + \bar{\boldsymbol{r}}) + \frac{\rho}{2}||\boldsymbol{A}\boldsymbol{x} - \boldsymbol{v} + \boldsymbol{u}||_2^2 - \frac{\rho}{2}||\boldsymbol{u}||_2^2$$

(3.44)

$$\boldsymbol{g}^{(n)} = \rho\boldsymbol{A}^T(\boldsymbol{A}\boldsymbol{x}^{(n)} - \boldsymbol{v}^{(n)} + \boldsymbol{u}^{(n)}) + \beta\boldsymbol{C}^T\boldsymbol{C}\boldsymbol{x}^{(n)}$$

(3.45)

$$\zeta_n = \frac{||\boldsymbol{g}^{(n)}||^2}{\rho||\boldsymbol{A}\boldsymbol{g}^{(n)}||^2 + \beta||\boldsymbol{C}\boldsymbol{g}^{(n)}||^2}.$$

(3.46)

3.3 Experimental method

This section describes the simulation setting and what evaluation metrics are used to assess the efficacy of each algorithm.

3.3.1 Simulation

3.3.1.1 True image

We simulated extremely low-count scans, typical for Y-90 PET following radioembolization, with the extended cardiac-torso (XCAT) (Fig. 3.3). We set the image size to $128 \times 128 \times 100$ with a voxel size $4.0 \times 4.0 \times 4.0$ (mm^3) and chose 100 slices ranging from lung to liver. The activity concentration ratio between healthy liver and a 42mL lesion was 1:5 to simulate a typical uptake ratio. We also placed a 42mL zero valued cold spot in the liver. In one case activity was assigned to the entire liver, while in the other case only to part of the liver as lobar or segmental treatment is common. Activity assigned to the lungs simulated a lung shunt of 5%. The rest of the phantom is 'cold'.

3.3.1.2 Projection

Our experiment uses the framework of Michigan Image Reconstruction Toolbox (MIRT). We first set the projection size to 128×100 with 168 projection angles and the detector width to 8mm when specifying the system model. For realistic simulation, we replicate the true and random counts observed in the patient imaging following radioembolization. Table 3.1 shows the low count conditions that we simulated corresponding to a relatively high Y-90 administration (Patient A) and a relatively low administration (Patient B) for patients treated at our clinic with glass microspheres. We use smaller area of liver (Fig. 3.3(b)) in the Patient B case because lower Y-90 administration
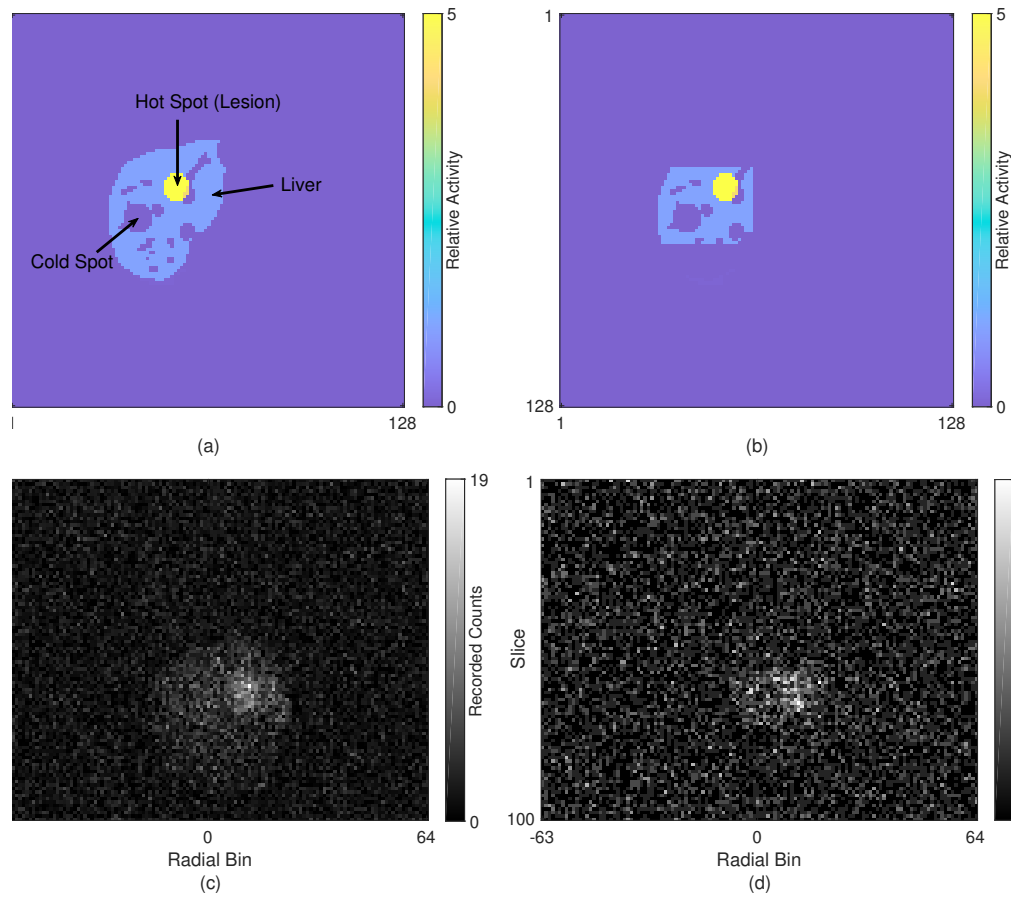
Figure 3.3: True image and the corresponding projection: (a),(c) and (b),(d) are slices of true image and projection views at one angle simulating the conditions of patient A and B data respectively. Activity concentration ratio between healthy liver and hot spot (lesion) is 1:5 to simulate the typical uptake ratio.

and consequent lower true counts are usually induced by treatment of smaller region in the liver. Simulated projections are shown in Fig. 3.3(c) and (d).

We also investigated increasing the number of projection angles by 10 times (while keeping total counts the same) to emulate fully 3D-PET (TOF) and test how each algorithm would work in the fully 3D-PET setting [59]. Section 3.4.2 discusses the results for this case.

Table 3.1: Administered activity and randoms fractions for two patients treated at our clinic with Y-90 radioembolization.

	Patient A	Patient B
Y-90 Injection(GBq)	3.9	0.9
True prompts	675,498	96,890
Random prompts	3,275,353	1,692,504
Total prompts	3,950,851	1,789,394
Random Fraction* (%)	83	95

*Random Fraction = (Random prompts / Total prompts)$\times$ 100

3.3.2 Evaluation metrics

We eroded each volume of interest (VOI) by 2 pixels to exclude resolution effects from the evaluation. We evaluated liver quantification by calculating activity recovery:

$$\text{Activity recovery in liver } (\%) = \frac{\text{Estimated mean counts}}{\text{True mean counts}} \times 100 \ \% \tag{3.47}$$

$$= \frac{\frac{1}{M J_{\text{Liver}}} \sum_{m=1}^{M} \sum_{j\in\text{Liver}} \hat{\boldsymbol{x}}_m[j]}{\frac{1}{J_{\text{Liver}}} \sum_{j\in\text{Liver}} \boldsymbol{x}_{\text{true}}[j]} \times 100 \ \%, \tag{3.48}$$

where M is the number of realizations and J_{Liver} is the number of voxels in the volume of liver. Estimated mean counts is calculated from the multiple realizations. We used 10 realizations in our experiment ($M = 10$). $\hat{\boldsymbol{x}}_m[j]$ indicates the jth voxel value at mth realization and $\boldsymbol{x}_{\text{true}}[j]$ denotes the jth voxel value of true counts.

Quantification in hot and cold spot (where true value of voxel is zero) are evaluated based on contrast recovery:

$$\text{Contrast recovery in hot spot } (\%) = \frac{C_i/C_{\text{BKG}} - 1}{R - 1} \times 100 \ \% \tag{3.49}$$

$$= \frac{\frac{\frac{1}{M J_{\text{Hotspot}}} \sum_{m=1}^{M} \sum_{j\in\text{Hotspot}} \hat{\boldsymbol{x}}_m[j]}{\frac{1}{J_{\text{Liver}}} \sum_{j\in\text{Liver}} \boldsymbol{x}_{\text{true}}[j]} - 1}{\frac{\frac{1}{J_{\text{Hotspot}}} \sum_{j\in\text{Hotspot}} \boldsymbol{x}_{\text{true}}[j]}{\frac{1}{J_{\text{Liver}}} \sum_{j\in\text{Liver}} \boldsymbol{x}_{\text{true}}[j]} - 1} \times 100 \ \% \tag{3.50}$$

$$\text{Contrast recovery in cold spot } (\%) = (1 - \frac{C_i}{C_{\text{BKG}}}) \times 100 \ \% \tag{3.51}$$

$$= \left(1 - \frac{\frac{1}{M J_{\text{Coldspot}}} \sum_{m=1}^{M} \sum_{j\in\text{Coldspot}} \hat{\boldsymbol{x}}_m[j]}{\frac{1}{J_{\text{Liver}}} \sum_{j\in\text{Liver}} \boldsymbol{x}_{\text{true}}[j]}\right) \times 100 \ \%. \tag{3.52}$$

C_i is the mean counts for object i and C_{BKG} is mean background (eroded liver) counts. R is the

true lesion-to-normal liver activity concentration ratio. We also study the counts bias the in field of view (FOV):

$$\text{FOV bias (\%)} = \frac{(\text{Total estimated counts} - \text{Total true counts})}{\text{Total true counts}} \times 100 \% \tag{3.53}$$

$$= \frac{\left(\frac{1}{M} \sum_{m=1}^{M} \sum_{j=1}^{n_p} \hat{\boldsymbol{x}}_m[j] - \sum_{j=1}^{n_p} \boldsymbol{x}_{\text{true}}[j]\right)}{\sum_{j=1}^{n_p} \boldsymbol{x}_{\text{true}}[j]} \times 100 \%. \tag{3.54}$$

Lastly, we calculate the image ensemble noise across realizations averaged over the liver to evaluate the variability across realizations:

$$\text{Noise (\%)} = \frac{\sqrt{\frac{1}{J_{\text{Liver}}} \sum_{j \in \text{Liver}} \left(\frac{1}{M-1} \sum_{m=1}^{M} (\hat{\boldsymbol{x}}_m[j] - \frac{1}{M} \sum_{m'=1}^{M} \hat{\boldsymbol{x}}_{m'}[j])^2\right)}}{\frac{1}{J_{\text{Liver}}} \sum_{j \in \text{Liver}} \boldsymbol{x}_{\text{true}}[j]} \times 100 \%, \tag{3.55}$$

3.4 Results

We compare the proposed method with regularization (ADMM-Reg) to the standard EM (1 subset), regularized SPS (SPS-Reg), NEG-ML and regularized NEG-ML (NEG-ML-Reg) algorithms. We used uniform image for the initial $\boldsymbol{x}$. For comparison, we also report evaluation results of our proposed method with the modified constraint $\boldsymbol{A}\boldsymbol{x} + \bar{\boldsymbol{r}}/2 \geq 0$. Changing the constraint requires a slight modification in (3.34):

$$v_i^{(n+1)} = [\hat{v}_i + \frac{\bar{r}_i}{2}]_+ - \frac{\bar{r}_i}{2}. \tag{3.56}$$

We exclude regularized EM in the comparison because regularized SPS and regularized EM converge to the same point.

In the plots shown in following subsections, β for regularization is 2^{-3} which is a value considering both the quantification in lesion and the benefit in noise. [59] reported that ψ value near the mean counts in the sinogram increases the bias, therefore, ψ value should be large enough for bias-free reconstruction. We report the evaluation result of NEG-ML with $\psi = 4$ in the plots, however, Section 3.4.3 enumerates all evaluation results with varying ψ and β values.

3.4.1 Evaluation result on 3-D PET emulation

This section reports the evaluation results when a simulation replicates patient B condition and uses 168 projection angles. Fig. 3.4 shows the results with plots showing how activity/contrast recovery versus iterations in VOIs evolve with iterations. Fig. 3.4 also includes a plot of noise versus iterations.
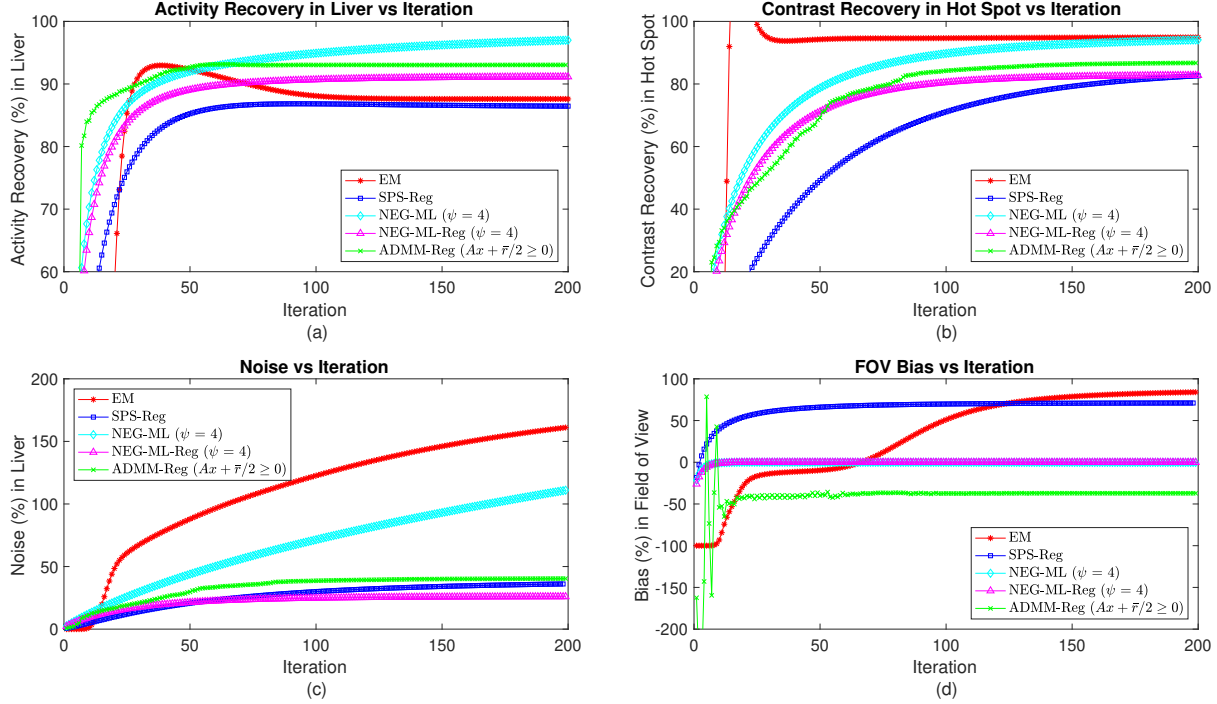
Figure 3.4: Results from simulating Patient B conditions. Proposed algorithm (green) gives higher contrast and better activity recovery than other regularized algorithms but NEG-ML-Reg (magenta) has lower noise in liver and FOV bias.

NEG-ML without regularization achieves higher activity/contrast recovery in VOIs than regularized methods, however, it keeps increasing the noise with the iterations. This is undesirable because the algorithm needs to stop before convergence to have an acceptable noise level. Proposed algorithm gives higher activity/contrast recovery than other regularized algorithms, however, NEG-ML-Reg has lower noise in liver and FOV bias.

3.4.2 Result on fully 3-D PET emulation

We also emulate the fully 3-D (TOF) PET by increasing the number of projection angles (from 168 to 1680) for the same Patient B conditions of Section 3.4.1. The results shown in Fig. 3.5 indicate that the converged evaluation results of NEG-ML-Reg (magenta) were changed compared to Fig. 3.4 (activity recovery in liver: $91.2\% \rightarrow 82.4\%$, contrast recovery in hot spot: $82.9\% \rightarrow 54.3\%$) while other algorithms including our proposed method remain similar.

Fig. 3.6 compares the images reconstructed using regularized algorithms when the number of projection angles changes (First row: 168, Second row: 1680). SPS-Reg and proposed algorithm (ADMM-Reg) generate almost identical images in two cases, however, the image from NEG-ML-Reg becomes blurry when the number of projection angles increases. The mean sinogram count

32
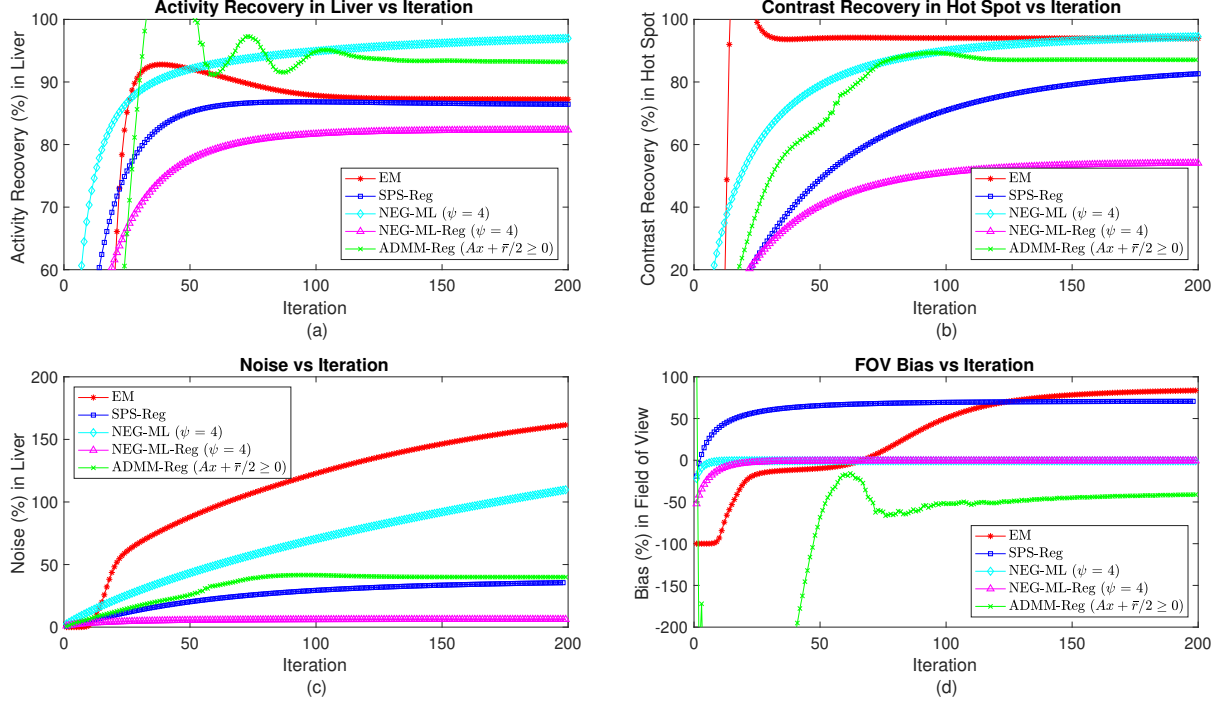
Figure 3.5: Evaluation result on simulation of fully 3D-PET (number of projection angles is 1680). Proposed algorithm converges to similar point in Fig. 3.4, whereas NEG-ML-Reg changes its converged point.

decreased when we increased the number of projection angles so NEG-ML-Reg must make more approximations when calculating $\max(\psi, \bar{y}_i^{(n)})$ in (3.43). Therefore, the impact of parameter ψ on reconstruction depends on the count level of sinogram, implying that a parameter ψ value optimized at a certain count level could generate an unexpected result whenever there is a change in the amount of administered activity, radionuclide or detector geometry.

3.4.3 Effect of algorithm parameter

We compare regularized algorithms by evaluating the reconstructed images at the 400th iteration in Table 3.2. Table 3.2 summarizes how changing β value for regularization, projection angles, ψ value for NEG-ML-Reg, random coincidence fraction and total true coincidence counts affects the reconstruction outputs. We also report evaluation results of our proposed method with the constraint $\boldsymbol{Ax} + \bar{\boldsymbol{r}} \geq 0$.

Better quantification result in Patient A case compared to Patient B case corresponds to the general knowledge that higher true coincidence counts and lower random coincidence fractions help to estimate the image precisely. We can also observe that higher β value for regularization decreases the noise, however, it worsens the other VOI metrics.

33
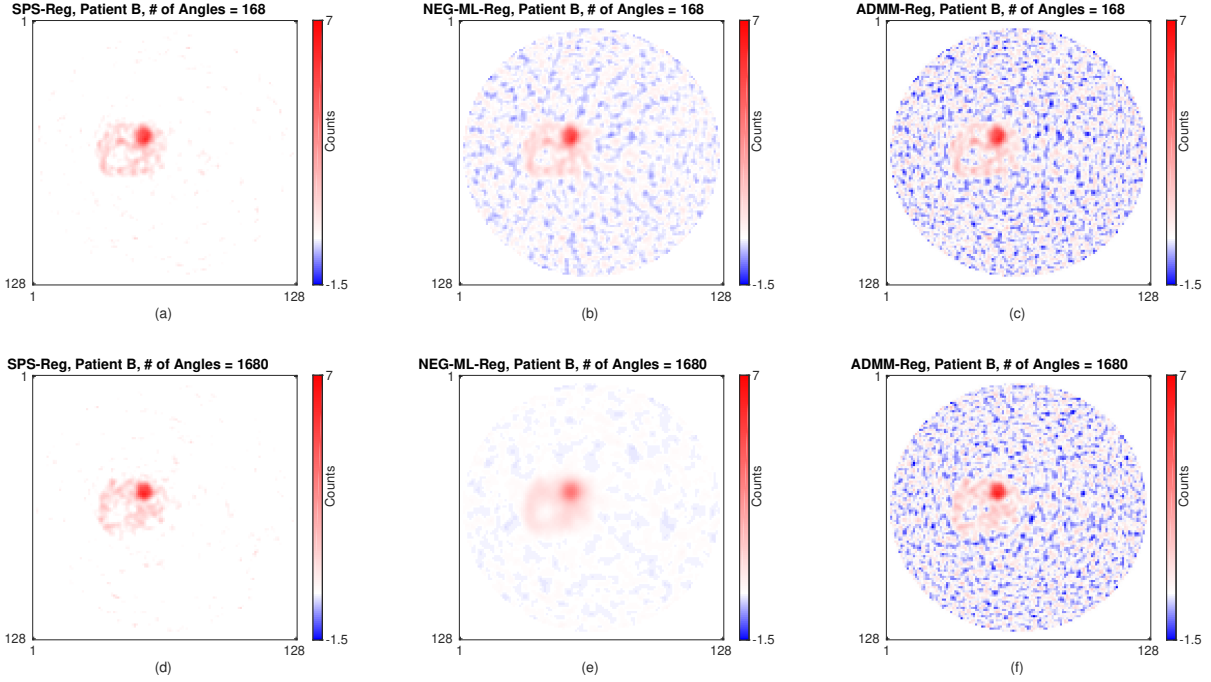
Figure 3.6: Reconstructed images using regularized SPS, NEG-ML-Reg with $\psi = 4$ and proposed algorithm. True image corresponds to Fig. 3.3(b). First row and second row are the results when the number of projection angle is 168 and 1680 respectively. Regularized SPS and proposed algorithm do not change much when the number of angles is increased. However, NEG-ML-Reg ($\psi = 4$) gets blurred.

The algorithms that allow negative values in image domain (NEG-ML-Reg, ADMM-Reg) generally give better quantification result than the standard algorithm (SPS-Reg). A trend found in NEG-ML-Reg results is that lower ψ value leads to higher activity/contrast recovery. However, at the same time, FOV bias also increases. Moreover, increasing the number of projection angles always decreases the activity/contrast recovery of NEG-ML-Reg while SPS-Reg and our method (ADMM-Reg) remain fairly stable. This finding agrees with the results shown in the previous subsections. The constraint $\boldsymbol{Ax} + \bar{\boldsymbol{r}} \geq 0$ of our proposed method (ADMM-Reg) generally gives better quantification than $\boldsymbol{Ax} + \bar{\boldsymbol{r}}/2 \geq 0$ except FOV bias. $\boldsymbol{Ax} + \bar{\boldsymbol{r}} \geq 0$ gives 1-5% improvement in VOI metrics except FOV bias compared to $\boldsymbol{Ax} + \bar{\boldsymbol{r}}/2 \geq 0$, however, $\boldsymbol{Ax} + \bar{\boldsymbol{r}}/2 \geq 0$ reduces FOV bias significantly in Patient B case.

3.5 Discussion

Conventional nonnegativity constraint in image domain leads to positive value of estimated projection $\bar{y}_i^{(n)}$ for $y_i = 0$ case in (3.2) because a_{ij} is nonnegative and $\bar{r}_i$ is positive. This mismatch

between $\bar{y}_i^{(n)}$ and y_i leads to positive bias in the cold region. Our proposed relaxation of nonnegativity constraint frees this restriction, thereby improving estimation in cold region. Improved estimation in cold region enables the reconstruction algorithm to estimate right counts in hot and warm region.

As shown in the previous section, a main advantage of proposed algorithm is that we retain the original Poisson log-likelihood so there is no parameter that must be manually optimized. Choosing a number of iterations in $\boldsymbol{x}$-update for one ADMM iteration is an algorithm parameter. We chose 1 iterations in $\boldsymbol{x}$-update for one ADMM iteration. We can assign any value to ρ and the algorithm adapts its value automatically as explained in Section 3.2.1.3. However, NEG-ML-Reg has a data-fit term parameter ψ that affects the results significantly and the optimal ψ value is different for each imaging condition. The NEG-ML-Reg algorithm can potentially be modified to automatically adapt the parameter ψ (i.e., multiplying some constant to the mean sinogram value), but any modification will need theoretical and experimental grounds beyond the scope of this paper. Nonetheless, setting ψ to very small value (i.e., $\psi = 10^{-3}$) makes NEG-ML-Reg robust to any count level as shown in the table 3.2. In this case, we observed that NEG-ML-Reg generates similar quantification in VOIs with proposed algorithm. However, NEG-ML-Reg with very small ψ gives high FOV bias and the algorithm does not have a room for modification to mitigate the FOV bias whereas our proposed method can reduce the FOV bias by slightly modifying the constraint (e.g., $\boldsymbol{A}\boldsymbol{x} + \bar{\boldsymbol{r}} \geq 0 \rightarrow \boldsymbol{A}\boldsymbol{x} + \bar{\boldsymbol{r}}/2 \geq 0$) without greatly impairing the other evaluation metrics.

Fig. 3.7(a) shows how cost function value (3.37) of each method decreases with iterations when we simulate the measurement with patient B condition and 168 projection angles. Because NEG-ML-Reg solves the minimization of modified cost function (3.11) problem, our proposed method (ADMM-Reg) and NEG-ML-Reg converge to the different cost function value. Our proposed method (ADMM-Reg) with the constraint $\boldsymbol{A}\boldsymbol{x} + \bar{\boldsymbol{r}} \geq 0$ achieves the lowest cost function value. Fig. 3.7(b) shows the measurement $\boldsymbol{y}$ (first row) and estimated measurements $\bar{\boldsymbol{y}}(\boldsymbol{x}^{(n)})$ at 400th iteration. The SPS-Reg estimate is always above $\bar{\boldsymbol{r}}$ because of the nonnegativity of system matrix element a_{ij} and the nonnegative constraint in image domain. Because NEG-ML-Reg does not enforce any constraint, $\bar{\boldsymbol{y}}(\boldsymbol{x}^{(400)})$ of NEG-ML-Reg has many negative valued predicted sinogram values. Lastly, we can check that estimates from our proposed method with constraint $\boldsymbol{A}\boldsymbol{x} + \bar{\boldsymbol{r}}/2 \geq 0$ lie above $\bar{\boldsymbol{r}}/2$. This confirms that our proposed method finds $\hat{\boldsymbol{x}}$ within the larger set that satisfies $\boldsymbol{A}\boldsymbol{x} + \bar{\boldsymbol{r}}/2 \geq 0$ rather than the conventional set ($\boldsymbol{x} \geq 0$).

A drawback of the proposed algorithm is that it requires more computation cost compared to the standard method and NEG-ML(-Reg) because of the need to compute matrix multiplication in (3.27) as well as auxiliary and dual variable. With our computer (Intel Core i7, 32 GB memory), 400 iterations of NEG-ML-Reg required 661 seconds for 168 projection views whereas proposed algorithm took 1,116 seconds. Finding an acceleration method with a convergence guarantee is a future work topic.
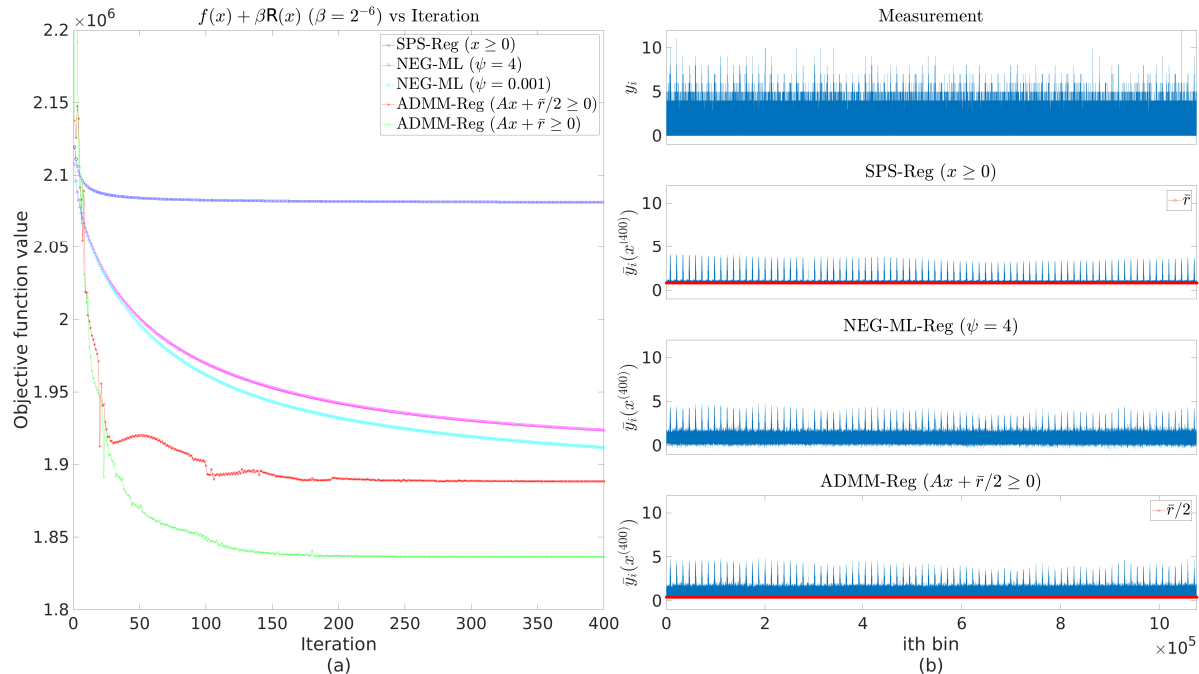
Figure 3.7: (a) Cost function value versus iteration. Proposed method with the constraint $\boldsymbol{Ax} + \bar{\boldsymbol{r}} \geq 0$ achieves the lowest cost function. (b) Measurement and estimated measurements. Standard method with conventional constraint (SPS-Reg) always predicts $\bar{y}_i(\boldsymbol{x})$ above $\bar{\boldsymbol{r}}$. Our proposed method finds $\hat{\boldsymbol{x}}$ within the larger set that satisfies the constraint (e.g., $\boldsymbol{Ax} + \bar{\boldsymbol{r}}/2 \geq 0$) rather than the conventional set ($\boldsymbol{x} \geq 0$).

3.6   Conclusion

This paper has presented a new PET reconstruction formulation with a relaxed nonnegativity constraint. The experimental results show that the proposed method reduces the bias in VOI when the true coincidence count-rate is low and the random fraction is high. The key of the proposed algorithm is incorporating the new constraint and adopting ADMM as a solver. Lastly our proposed method is not limited to Y-90 PET but has application in other imaging situations with low true count rates and high random fractions such as ion beam therapy [62].

Table 3.2: Comparison between regularized algorithms at the 400th iterations. We calculate the evaluation metrics using the results from 10 realizations.

Condition	β	NPA	Algorithm		ARL	CRH	CRC	FOVB	IEN
Patient A	2^{-3}	168	SPS-Reg		92.5	91.3	85.9	15.7	39.2
			NEG-ML-Reg	$\psi = 4$	94.8	91.2	94.6	**-0.9**	**38.8**
				$\psi = 10^{-3}$	**96.2**	91.5	**95.3**	-11.5	41.2
			ADMM-Reg	$Ax + \bar{r}/2 \geq 0$	95.4	**91.9**	94.6	-7.1	39.9
				$Ax + \bar{r} \geq 0$	**96.2**	91.7	**95.3**	-14.1	41.5
		1680	SPS-Reg		92.6	91.3	86.1	15.8	38.9
			NEG-ML-Reg	$\psi = 4$	90.7	80.0	84.1	**0.0**	**12.1**
				$\psi = 10^{-3}$	96.1	91.6	95.8	-11.4	40.9
			ADMM-Reg	$Ax + \bar{r}/2 \geq 0$	95.5	91.6	**96.3**	-7.0	41.5
				$Ax + \bar{r} \geq 0$	**96.4**	**91.7**	96.0	-15.3	41.6
	2^{-6}	168	SPS-Reg		92.8	95.4	85.4	16.8	62.7
			NEG-ML-Reg	$\psi = 4$	96.5	95.9	97.9	**-1.0**	80.7
				$\psi = 10^{-3}$	**97.6**	**96.4**	**98.6**	-11.4	82.8
			ADMM-Reg	$Ax + \bar{r}/2 \geq 0$	96.0	95.8	97.2	-2.3	**65.4**
				$Ax + \bar{r} \geq 0$	97.5	96.1	98.5	-13.7	80.6
		1680	SPS-Reg		92.9	95.6	85.7	16.9	62.3
			NEG-ML-Reg	$\psi = 4$	95.5	92.1	95.1	**0.0**	**38.5**
				$\psi = 10^{-3}$	97.7	96.5	99.1	-11.4	82.3
			ADMM-Reg	$Ax + \bar{r}/2 \geq 0$	96.5	96.5	100.6	-2.0	113.7
				$Ax + \bar{r} \geq 0$	**98.3**	**96.6**	**100.1**	-17.5	114.9
Patient B	2^{-3}	168	SPS-Reg		86.4	85.5	81.5	71.2	38.4
			NEG-ML-Reg	$\psi = 4$	91.2	82.9	84.7	**-0.1**	**26.1**
				$\psi = 10^{-3}$	94.2	87.0	90.5	-60.3	40.4
			ADMM-Reg	$Ax + \bar{r}/2 \geq 0$	93.1	86.9	**91.3**	-37.2	40.5
				$Ax + \bar{r} \geq 0$	**94.3**	**87.1**	90.7	-67.4	40.6
		1680	SPS-Reg		86.4	85.7	80.9	70.8	38.0
			NEG-ML-Reg	$\psi = 4$	82.4	54.3	59.4	**-0.7**	**6.2**
				$\psi = 10^{-3}$	94.2	87.2	89.2	-62.9	39.9
			ADMM-Reg	$Ax + \bar{r}/2 \geq 0$	93.0	87.1	**90.0**	-37.4	39.9
				$Ax + \bar{r} \geq 0$	**94.4**	**87.3**	89.3	-72.1	40.0
	2^{-6}	168	SPS-Reg		86.1	92.5	81.2	81.5	81.6
			NEG-ML-Reg	$\psi = 4$	96.1	92.6	93.7	**-0.1**	**79.7**
				$\psi = 10^{-3}$	97.0	94.9	96.7	-64.6	108.9
			ADMM-Reg	$Ax + \bar{r}/2 \geq 0$	92.7	94.3	**99.0**	-10.1	117.6
				$Ax + \bar{r} \geq 0$	**97.1**	**95.1**	98.1	-88.4	122.8
		1680	SPS-Reg		85.9	92.7	79.9	81.0	81.0
			NEG-ML-Reg	$\psi = 4$	90.6	81.3	82.2	**-0.6**	**22.5**
				$\psi = 10^{-3}$	97.0	95.1	94.8	-67.9	107.8
			ADMM-Reg	$Ax + \bar{r}/2 \geq 0$	92.5	94.5	**97.1**	-9.2	119.4
				$Ax + \bar{r} \geq 0$	**97.5**	**95.5**	96.3	-99.9	122.3

*NPA: Number of Projection Angles, ARL: Activity Recovery in Liver,
CRH: Contrast Recovery in Hot spot, CRC: Contrast Recovery in Cold spot,
FOVB: FOV Bias, IEN: Image Ensemble Noise

CHAPTER 4

Y-90 SPECT Reconstruction With a Model for Tissue-Dependent Bremsstrahlung Production

While the yield of positrons used in Y-90 PET is independent of tissue media, Y-90 SPECT imaging is complicated by the tissue dependence of bremsstrahlung photon generation. The probability of bremsstrahlung production is proportional to the square of the atomic number of the medium. Hence, the same amount of activity in different tissue regions of the body will produce different numbers of bremsstrahlung photons. Existing reconstruction methods disregard this tissue-dependency, potentially impacting both qualitative and quantitative imaging of heterogeneous regions of the body such as bone with marrow cavities. In this proof-of-concept study, we propose a new maximum-likelihood (ML) method that incorporates bremsstrahlung generation probabilities into the system matrix, enabling images of the desired Y-90 distribution to be reconstructed instead of the 'bremsstrahlung distribution' that is obtained with existing methods. The tissue-dependent probabilities are generated by Monte Carlo simulation while bone volume fractions for each SPECT voxel are obtained from co-registered CT. First, we demonstrate the tissue dependency in a SPECT/CT imaging experiment with Y-90 in bone equivalent solution and water. Visually, the proposed reconstruction approach better matched the true image and the Y-90 PET image than the standard bremsstrahlung reconstruction approach. An XCAT phantom simulation including bone and marrow regions also demonstrated better agreement with the true image using the proposed reconstruction method. Quantitatively, compared with the standard reconstruction, the new method improved estimation of the liquid bone:water activity concentration ratio by 40% in the SPECT measurement and the cortical bone:marrow activity concentration ratio by 58% in the XCAT simulation.

4.1   Introduction

Novel therapeutic applications have sparked growing interest in quantitative imaging of Y-90, an almost pure beta emitter (average decay energy, 0.94 MeV; mean tissue penetration, 2.5 mm;

This chapter is based on [8, 9].

half-life, 64 h) that is used in internal radionuclide therapy. Applications where Y-90 imaging has been used include microsphere radioembolization of hepatic malignancies [63], peptide receptor radionuclide therapy of neuroendocrine tumors [64] and ibritumomab radioimmunotherapy [65] of non-Hodgkins lymphoma. Additionally, Y-90 imaging has been reported in radiation synovectomy, a treatment option for inflammation of the synovium membrane found in joints such as the knee [66]. In such therapies, the lack of gamma photons simplifies radioprotection of surrounding organs and personnel, but it makes imaging of Y-90 complex; it involves SPECT via bremsstrahlung photons associated with the Y-90 betas or PET via a very low abundance positron associated with Y-90 decay [67, 68]. PET has the advantage of superior resolution over bremsstrahlung SPECT, but a disadvantage is the high noise associated with low (true) count-rates in the presence of high randoms [63]. For this reason, and because of the wider accessibility of SPECT, interest in bremsstrahlung imaging of Y-90 continues.

While the yield of positrons used in Y-90 PET is independent of the tissue media, the yield of bremsstrahlung photons used in SPECT is tissue dependent. The Y-90 bremsstrahlung yield consists of 2 components: internal bremsstrahlung (IB) and external bremsstrahlung (EB) [69–71]. The bremsstrahlung energy spectra corresponding to both components extend from zero to the beta endpoint energy, 2.3 MeV for Y-90. IB arises during the beta decay process itself, while EB photons are produced as beta particles pass through the media containing the radioisotope and are accelerated in the Coulomb fields of atomic nuclei and electrons of the medium. The IB energy spectrum is thus a property of the emitter, while the EB energy spectrum depends on both the energy spectrum of the beta emitter and the material properties of the surrounding medium. Most significantly, the cross section describing the production of EB, based on the Bethe-Heitler formula [72], is proportional to Z^2 where Z is the atomic number of the tissue medium.

As a consequence of the Z^2 dependence of the EB production probability, the same amount of Y-90 activity in different tissue regions of the body will generate significantly different numbers of bremsstrahlung photons, which impacts both qualitative and quantitative assessment of Y-90 SPECT images. The difference in bremsstrahlung production probabilities (per beta decay) is particularly significant when comparing bone and soft tissue.

Although specialized reconstruction methods have been developed for Y-90 SPECT imaging [73–75], these methods have not accounted for the tissue-dependent bremsstrahlung yield. This paper reports simulations and experimental measurements to demonstrate the effect and implement and test a reconstruction formulation that accounts for the tissue dependency of bremsstrahlung generation in the SPECT system model. The method relies on co-registered CT to determine the tissue composition of each SPECT voxel, which is facilitated by the availability of hybrid SPECT-CT.

4.2 Methods

4.2.1 Image reconstruction with a tissue dependent system model

Maximum likelihood (ML) image reconstruction performs the following optimization with respect to an image $\boldsymbol{x}$:

$$\hat{\boldsymbol{x}} = \underset{\boldsymbol{x} \geq \boldsymbol{0}}{\operatorname{argmin}} f(\boldsymbol{x}), \quad f(\boldsymbol{x}) = \sum_{i=1}^{n_d} \bar{y}_i(\boldsymbol{x}) - y_i \log \bar{y}_i(\boldsymbol{x}), \tag{4.1}$$

where n_d is the number of rays, $f(\boldsymbol{x})$ is the Poisson negative log-likelihood between measurement $\boldsymbol{y}$ and estimated measurement means $\bar{\boldsymbol{y}}(\boldsymbol{x})$, and $\bar{\boldsymbol{y}}(\boldsymbol{x}) = \boldsymbol{A}\boldsymbol{x} + \bar{\boldsymbol{r}}$. The matrix $\boldsymbol{A}$ denotes the system model, incorporating factors such as attenuation coefficients. $\bar{\boldsymbol{r}}$ denotes the mean background events such as scatter and random coincidence.

We incorporate the tissue-dependent probability into the image reconstruction by multiplying the system matrix $\boldsymbol{A}$ by a matrix $\boldsymbol{B}$ that models the bremsstrahlung spectra produced in each voxel as a bone volume fraction (BVF) weighted mixture of the bone-only and tissue-only spectra. We consider only two media, bone and soft-tissue where the bremsstrahlung generation probability differs highly, but the method can be easily extended to include more media. The new system model $\tilde{\boldsymbol{A}}$ can be expressed as:

$$\tilde{\boldsymbol{A}} = \boldsymbol{A}\boldsymbol{B} = \begin{bmatrix} a_{11} & a_{12} & \dots & a_{1n_p} \\ a_{21} & a_{22} & \dots & a_{2n_p} \\ a_{31} & a_{32} & \dots & a_{3n_p} \\ \dots & \dots & \dots & \dots \\ a_{n_d1} & a_{n_d2} & \dots & a_{n_dn_p} \end{bmatrix} \begin{bmatrix} b_1 & 0 & \dots & 0 \\ 0 & b_2 & \dots & 0 \\ \dots & \dots & \dots & 0 \\ 0 & 0 & \dots & b_{n_p} \end{bmatrix}, \tag{4.2}$$

where n_p is the number of voxels of the unknown image $\boldsymbol{x}$ and $\boldsymbol{B}$ is a diagonal matrix with diagonal elements:

$$b_j = 1 - \mathrm{BVF}_j + q_{\mathrm{bone}} \cdot \mathrm{BVF}_j. \tag{4.3}$$

q_{bone} is the bremsstrahlung photon generation probability ratio between bone and tissue. BVF_j is a BVF of jth voxel in SPECT and we use CT information (attenuation coefficients) to determine the
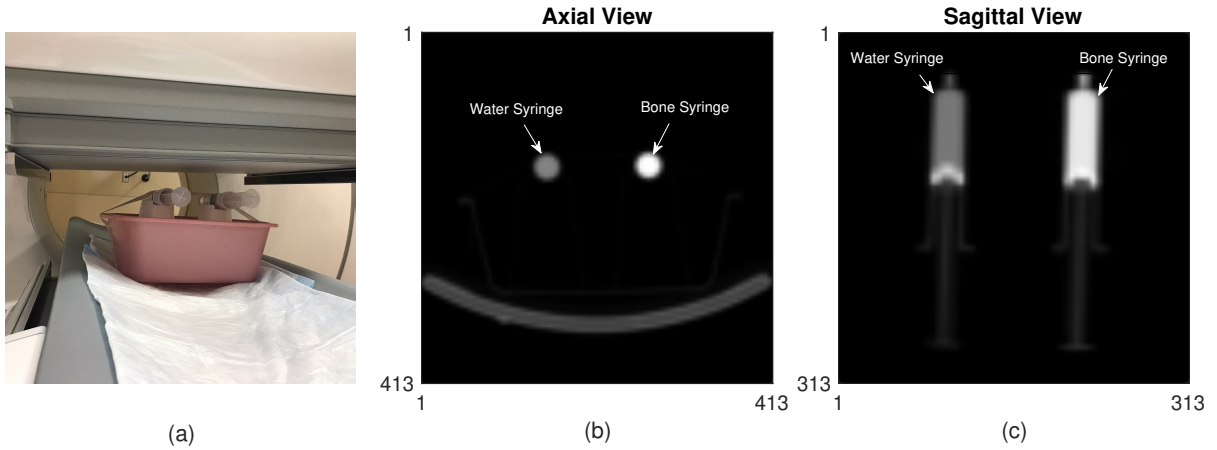
Figure 4.1: SPECT/CT measurement of bone and liquid syringes with same Y-90 concentration: (a) Setup (b)-(c) CT images.

BVF of each voxel in SPECT:

$$\text{BVF} = g(\boldsymbol{\eta}) \tag{4.4}$$

$$\eta_k = \begin{cases} 1, & \mu_k \geq c \\ 0, & \mu_k < c, \end{cases} \tag{4.5}$$

where $\boldsymbol{\eta}$ is a mask image indicating bone voxels and g denotes an interpolating function to relate CT sized mask image with SPECT sized BVF image. μ_k is the kth voxel of the attenuation map and a constant c is the threshold value to determine if a voxel is bone or tissue. We set c value as 80% of the maximum value of the attenuation map.

4.2.2 Bremsstrahlung yield in different tissue

To obtain the tissue dependent (external) bremsstrahlung probabilities to include in the above system model, we performed simulations using the *pencyl* program of the PENELOPE (version 2014) Monte Carlo electron/photon transport package [76]. The PENELOPE database of bremsstrahlung differential cross sections are based on the partial-wave database compiled by [77]. For the present simulations, the Y-90 beta emission spectrum from the *BetaShape* program [78] was coupled with PENELOPE. The PENELOPE database of pre-defined materials, which is adapted from the database of the ESTAR program of [79], was used for media definition. The cutoff energy for particle transport termination with remaining energy assumed to be locally absorbed was set at 10 keV for both electrons and photons. PENELOPE generated EB emission spectra by simulating a Y-90 point source in an infinite geometry for the medium of interest: ICRP cortical bone, marrow,
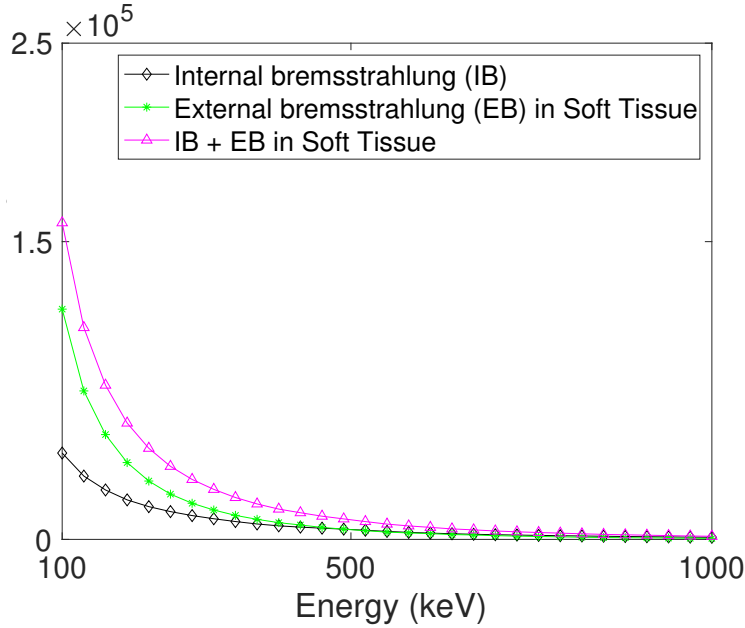
Figure 4.2: PENELOPE-generated EB spectrum combined with the theoretical absolute IB spectrum to produce total Y-90 bremsstrahlung emission spectrum for soft tissue.

tissue and lung tissue. Additionally, for comparison with bone, we generated the EB spectrum for Y-90 in K_2HPO_4 solution to justify the choice of this salt as a bone equivalent medium in the experiment described below. We constructed the bremsstrahlung energy spectrum by tallying the emitted photon energy at the point of generation, before any potential self-absorption. The Y-90 IB spectrum, based on the Knipp, Uhlenbeck and Bloch (KUB) theory was taken from the work of [69]. We combined the PENELOPE-generated EB spectra (in absolute units of photons/eV/decay) with the theoretical absolute IB spectrum to produce total Y-90 bremsstrahlung emission spectra for the different media. Fig. 4.2 shows an example of combined (EB + IB) spectrum for soft tissue.

4.2.3 Experimental measurement and phantom simulation

To demonstrate the impact of tissue dependent bremsstrahlung generation on SPECT imaging and to evaluate the performance of bremsstrahlung SPECT reconstruction with the above tissue dependent system model, we performed an experimental measurement and a phantom simulation study with Y-90 in bone and tissue media.

4.2.3.1 SPECT/CT measurement with Y-90 in tissue and bone equivalent media

The experiment was performed with Y-90 in tissue-equivalent (water) and bone equivalent material. The bone equivalent liquid solution was prepared by dissolving K_2HPO_4 salt (dipotassium

hydrogen phosphate) in DI water to form a saturated solution of K_2HPO_4. Anhydrous K_2HPO_4 (298.5 g) was dissolved in 200 mL of DI water by use of magnetic stirring with the mixture covered until solution was achieved (1 hour). This solution mimics density and effective Z number of cranium bone [80]. A chelator (2.5 uM EDTA; appropriate amount from a 1 M EDTA diammonium salt hydrate stock solution) was added to the solution to avoid adherence of Y-90 to plastic walls [81]. 40 mL of the bone equivalent solution was mixed with 25 MBq of Y-90 in a 60 mL plastic syringe. A second syringe with water (to mimic tissue) was prepared with the same geometry and Y-90 concentration as in the bone-equivalent syringe.

The bone and tissue equivalent syringes were positioned as shown in Fig. 4.1(a) and imaged with a Siemens Intevo SPECT/CT system equipped with a high energy general purpose collimator. A 105 - 195 keV bremsstrahlung acquisition window was selected based on our previous work [75]. The following acquisition parameters were used: $180°$ and 64 views per head with 15 sec/view; step-and-shoot; a 128×128 matrix with a pixel size of 4.8-mm. The CT component of acquisition used full circle rotation, 130-kV, 80-mAs and was reconstructed with a $512 \times 512 \times 196$ matrix (0.98-mm $\times$ 0.98-mm $\times$ 2-mm voxel size).

The CT-based attenuation map (at 150-keV, the center energy of the acquisition window) generated with the camera software was saved for attenuation correction and to determine the voxel-level BVFs for the new system model of Section 4.2.1. At 150 keV bremsstrahlung generation probability in bone equivalent liquid is 1.4 times the probability in water according to the simulation results discussed in section 4.3.1. Therefore q_{bone} in (6) was also set as 1.4 for reconstructing images with the proposed model. We reconstructed images with in-house 3D OS-EM [82] including attenuation, collimator detector response and without and with tissue-dependent probabilities (with and without matrix $\boldsymbol{B}$ in (4.2)). The reconstruction parameters (15 iterations 8 subsets and no post-smoothing) were chosen based on previous phantom studies [75]. In addition, for comparison we also reconstructed images using Siemens Flash3D OS-EM software, including attenuation correction and collimator detector response.

Additionally, for comparison, Y-90 PET/CT was also performed for the same source geometry. Data was acquired with a Siemens Biograph mCT scanner and was reconstructed with Siemens 3D-OS-EM software including point-spread function and time-of-flight information using 1 iteration, 21 subsets and a 5-mm FWHM Gaussian post-filter. The matrix size was 200×200 (pixel size 4.07-mm). These PET parameters were chosen based on a previous phantom study [83].

4.2.3.2 XCAT simulations

A clinically realistic geometry was simulated using the region from spine to upper femur of the XCAT phantom [84]. We considered a case where the true activity concentration ratio is 1:1 for bone:marrow. However, when generating the projection measurement $\boldsymbol{y}$ in (4.1), we changed the
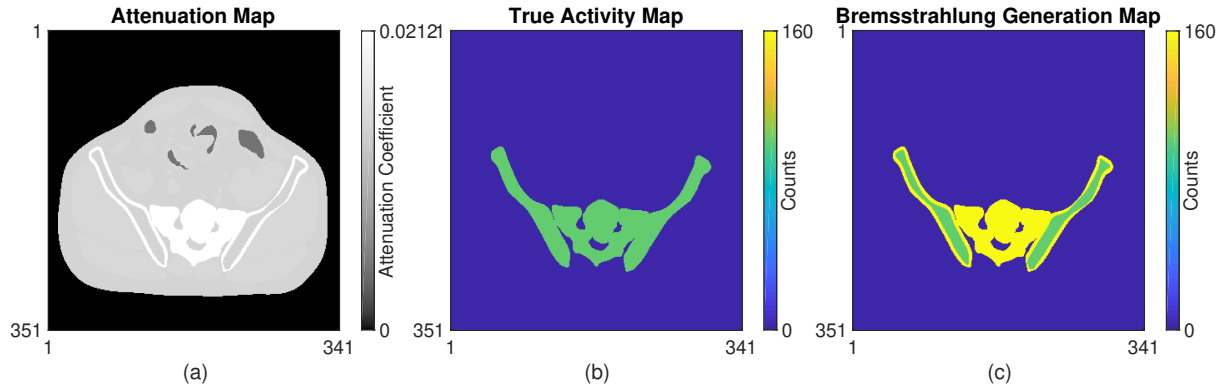
Figure 4.3: A transaxial slice of XCAT showing sacrum bone and iliac bone with marrow cavity (a) attenuation map (b) true activity map (c) bremsstrahlung photon map. We set activity ratio between bone and marrow as 1:1. When generating the projections, we set activity ratio between bone and marrow as 1.6:1.

value of voxels corresponding to ICRP bone to represent the 1.6 times higher bremsstrahlung photon generation probability in bone relative to marrow (at 150 keV bremsstrahlung generation probability in bone is 1.6 times the probability in marrow according to the PENELOPE results discussed in Section 4.3.1). Fig. 4.3(c) shows the activity map with different bremsstrahlung generation probability when the true activity map is Fig. 4.3(b). SPECT projection data for this digital phantom were generated using an analytical projector, which included non-uniform attenuation and the collimator detector response of the SPECT camera. Images were reconstructed with in-house developed 3D OS-EM (35 iterations 8 subsets) including attenuation, collimator detector response and without and with tissue-dependent probabilities (q_{bone} in equation (4.3) set as 1.6).

4.3   Results

4.3.1   Bremsstrahlung yield in different tissue

Fig. 4.4 and table 4.1 compare the total (external + internal) bremsstrahlung yield in the different media. While the yield in lung and different soft tissue media (soft tissue, red marrow and yellow marrow) are very similar, the yield in bone is substantially higher. In the energy range of the SPECT acquisition window (100 - 200 keV) bremsstrahlung production is 1.6-1.7 times as high in bone as in other tissue. Fig. 4.5(a) compares the bremsstrahlung yield for the K_2HPO_4 solution vs. cranium bone and for water vs. soft-tissue to demonstrate equivalence of the media used in the experiment to true bone and tissue. Additionally, mass attenuation coefficients over a range of energies were generated by inputting the compositions to the XCOM database and the corresponding linear

---

https://physics.nist.gov/PhysRefData/Xcom/html/xcom1.html

44
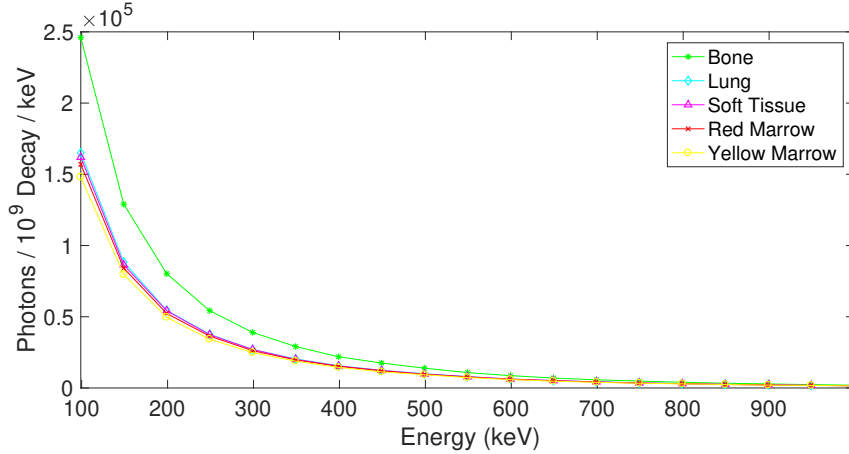
Figure 4.4: Penelope electron shower results for total bremsstrahlung yield in the different ICRP tissue media

attenuation coefficients compared in Fig. 4.5(b) also demonstrate equivalence.

Table 4.1: Total bremsstrahlung yield in different media as a function of energy.

keV	Photons/keV/10^9 decays					
	Bone	Marrow	Bone:Marrow	Liquid Bone	Water	Liquid Bone:Water
50	6.87E+05	4.06E+05	1.69	6.61E+05	4.66E+05	1.42
100	2.43E+05	1.45E+05	1.67	2.34E+05	1.66E+05	1.41
150	1.28E+05	7.84E+04	1.64	1.24E+05	8.85E+04	1.40
200	7.89E+04	4.92E+04	1.61	7.71E+04	5.55E+04	1.39
500	1.37E+04	9.12E+03	1.50	1.34E+04	1.01E+04	1.32
1000	2.01E+03	1.48E+03	1.35	1.92E+03	1.55E+03	1.24

4.3.2 SPECT measurement with tissue and bone equivalent media

Fig. 4.6(a)-(d) are the syringe images reconstructed using commercial PET and SPECT software. The PET image shows that the two syringes have similar Y-90 activity concentration (true concentrations are equal) because PET depends on positron emission, which is not tissue dependent. However, the SPECT image shows that the bone syringe has significantly higher concentration than the water syringe because of the higher bremsstrahlung yield in bone. Fig. 4.7(a) is the profile at the center of the syringes (in relative units). The peaks of the profile corresponding to the two syringes in PET are identical whereas in SPECT the peak of the bone syringe is 1.4 times higher than that of the water syringe, which is attributed to the 1.4 times higher bremsstrahlung production probability in liquid bone compared with water in the energy range of the SPECT acquisition window (Table 4.1).

45
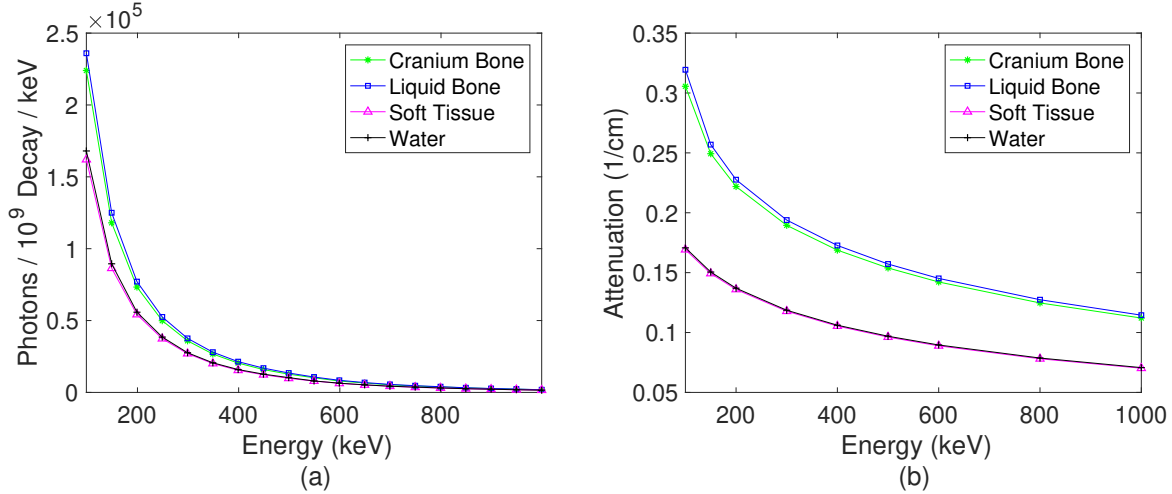
Figure 4.5: Comparison of bremsstrahlung yield (left) and attenuation coefficient (right) for bone vs. liquid bone and tissue vs. water, demonstrating equivalence of media used in the experiment to true bone and tissue.

Fig. 4.6(e)-(h) are the SPECT images reconstructed using the Michigan image reconstruction toolbox without and with incorporating tissue-dependent probabilities into the system matrix. The image reconstructed with the new model shows that the two syringes have similar concentration of Y-90. Also, the peaks of the profile corresponding to the two syringes become identical (as in the PET profile) when we incorporate the tissue-dependent probability as shown in Fig. 4.7(b).

For quantitative evaluation of SPECT images, we compared the liquid bone to water count concentration ratio in two syringes to the true activity concentration ratio (equal to 1.0). The new model gives a ratio of 1.03 while the standard model gives a ratio of 1.43 because of overestimating the counts in the bone syringe.

4.3.3 XCAT simulations

We compared SPECT reconstructions using the new model and standard model. For visualization and evaluation, we interpolated SPECT image to match the CT image size. Visually, there is substantially better agreement between the SPECT reconstruction and the true activity map when the system model included the tissue dependent probability (Fig. 4.8 and 4.9).

As in the experiment, for a quantitative evaluation, we compared the bone to marrow count concentration ratio to the true activity concentration ratio (equal to 1.0). The new model gives a ratio of 1.06 while the standard model gives a ratio of 1.64 because of overestimating the counts in the bone region. Here, we used a small VOI (56 voxels per slice, 3 slices) at the center of the bone and marrow regions to exclude partial volume effects.

46
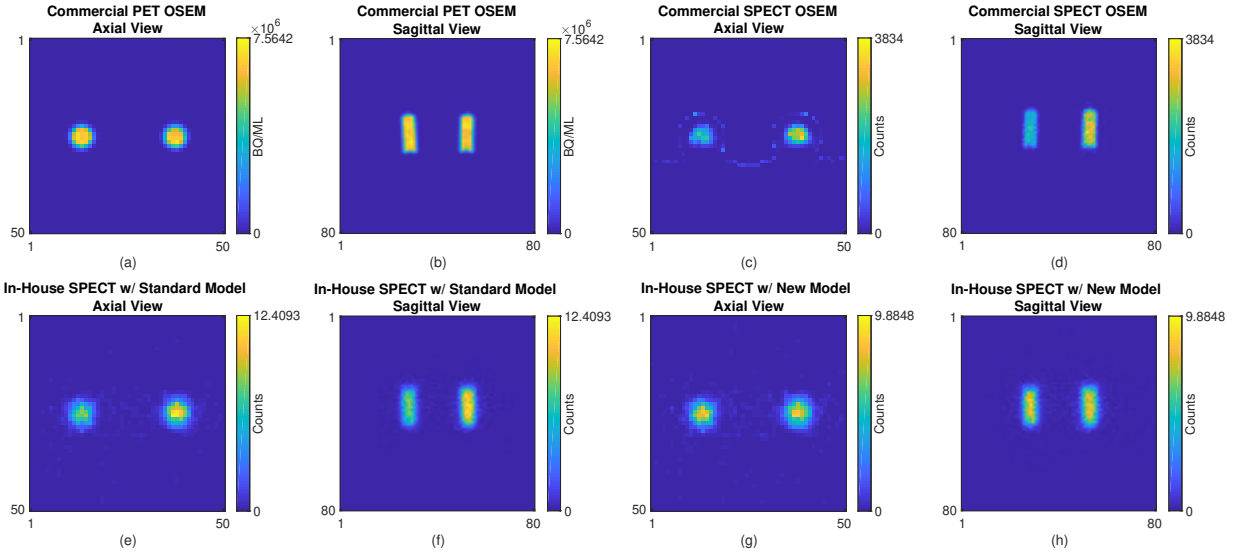
Figure 4.6: Reconstructed images corresponding to the experiment of Fig. 4.1: (a)-(d) Commercial PET and SPECT, (e)-(h) In-house SPECT with standard model and in-house SPECT with new model

Table 4.2: EB and IB stand for external and IB, respectively. Comparison of including and excluding IB in liquid bone and water. Without modeling the IB, we would set q_{bone} as 1.6 rather than 1.4.

keV	Photons/keV/10^9 decays					
	Bone	Marrow	Bone:Marrow	Liquid Bone	Water	Liquid Bone:Water
50	6.87E+05	4.06E+05	1.69	6.61E+05	4.66E+05	1.42
100	2.43E+05	1.45E+05	1.67	2.34E+05	1.66E+05	1.41
150	1.28E+05	7.84E+04	1.64	1.24E+05	8.85E+04	1.40
200	7.89E+04	4.92E+04	1.61	7.71E+04	5.55E+04	1.39
500	1.37E+04	9.12E+03	1.50	1.34E+04	1.01E+04	1.32
1000	2.01E+03	1.48E+03	1.35	1.92E+03	1.55E+03	1.24

4.4 Discussion and conclusions

In this study we showed the impact of tissue-dependent bremsstrahlung generation on both qualitative and quantitative Y-90 SPECT/CT imaging and investigated a new reconstruction formalism to correct for this effect. The new reconstruction system model uses Monte Carlo (PENELOPE) derived bremsstrahlung generation probabilities and CT-derived bone volume fractions in each voxel. We used a potassium salt, which we showed is equivalent to cranium bone in terms of bremsstrahlung yield and attenuation coefficient, to experimentally demonstrate the tissue dependency. In the SPECT/CT measurement with equal concentrations of Y-90 in bone and tissue equivalent liquids,
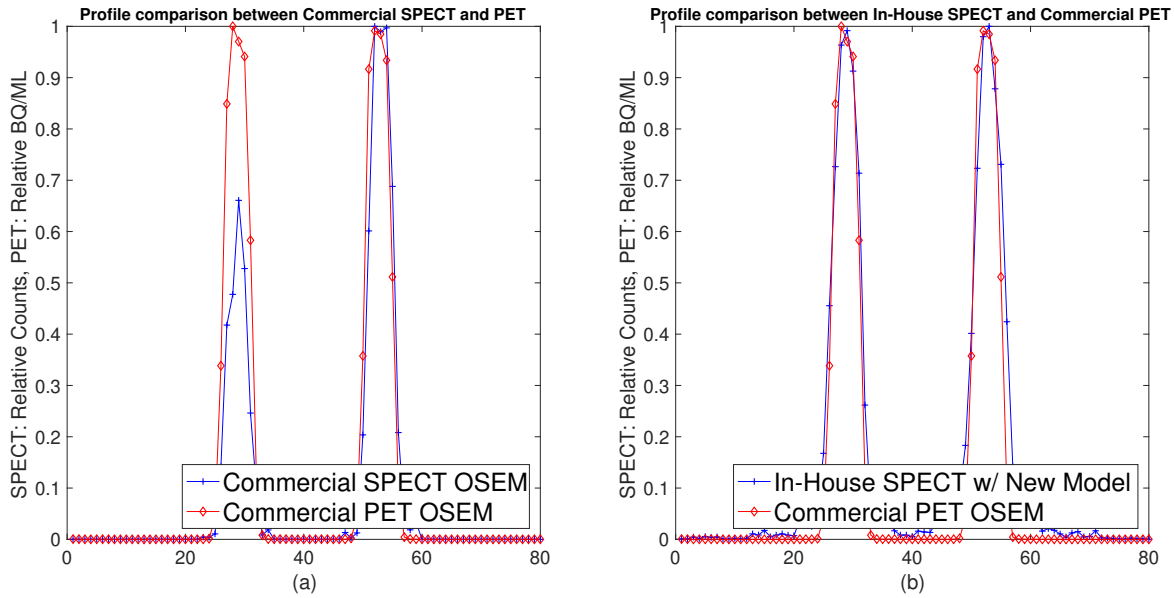
Figure 4.7: Profile at the center of syringe: (a) Commercial PET and SPECT (b) In-house SPECT with standard model and in-house SPECT with new model

the count concentration in the bone region was significantly higher than in the tissue region with standard reconstruction, but approached the true distribution with the new reconstruction model. Similar improvements were also demonstrated for the XCAT phantom when activity in bone was 'artificially' increased relative to marrow to mimic the higher bremsstrahlung generation probability. For quantifying the activity concentration ratio in two media the new reconstruction performed 40% (the proposed method had 3% error whereas the standard method had 43% error) better than the standard reconstruction in the experimental study and 58% (the proposed method had 6% error whereas the standard method had 64% error) better than the standard reconstruction in the XCAT study. This improvement is made without additional heavy computational cost or memory consumption. With our computer (Intel Core i7- 7700K), 35 iterations (with 8 subsets) of standard model required 16.4 seconds whereas proposed algorithm took 16.6 seconds.

Prior to the recent study of [71] where the importance of IB was highlighted, Y-90 SPECT (simulation) studies ignored the contribution of IB. However, as we did in the current study, including this component, which is not Z dependent, is important for getting the exact value of q_{bone}. Table 4.4 shows how the yield ratio for the two media would be changed if we only included the Z-dependent EB component. For the experiment with liquid bone, we would set the q_{bone} as 1.6 rather than 1.4. based on this yield ratio. However, setting q_{bone} as 1.6 would result in the underestimation of counts in bone syringe ($1.03 \rightarrow 0.94$).

Dividing standard reconstruction by the matrix $\boldsymbol{B}$ in (4.2) could be an alternative approach
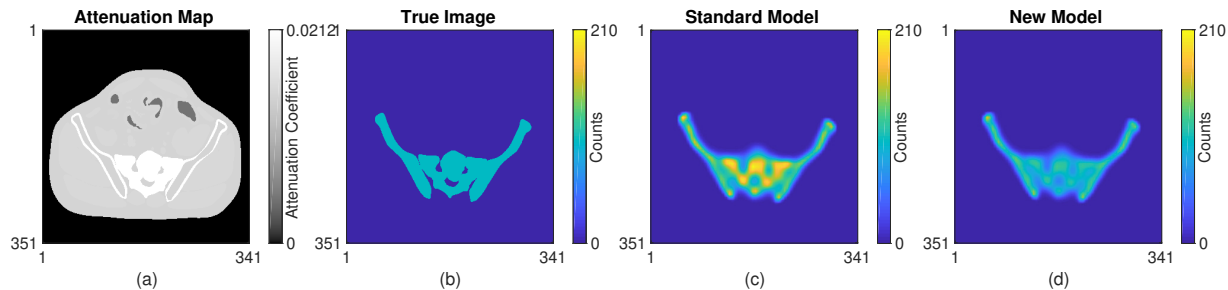
Figure 4.8: Attenuation map (a), true image (b) and reconstruction results corresponding to XCAT.
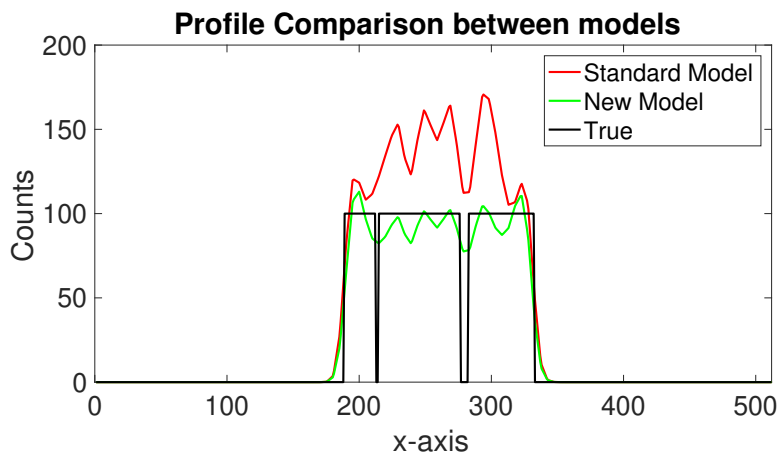
Figure 4.9: Horizontal line profile across the slice in Fig. 4.8.

for incorporating the tissue dependent effects although this approach does not correctly model the statistical (Poisson) nature of the acquisition. We evaluated this post-reconstruction approach using the experiment data with bone and tissue equivalent syringes in Fig. 4.1. We found that this alternative method gives the same quantification result as our proposed method (liquid bone to water count concentration: 1.03). However, there was a difference between images generated by this approach and our proposed method (difference in voxel counts of the two image ranges from -4.1% - 4.0% of each voxel count). Moreover, it would lead to different result compared to our method when $f(\boldsymbol{x})$ in (4.1) includes the regularization term for penalizing the image roughness and controlling noise in extreme imaging cases (e.g., low-count setting) because the weight of likelihood term and that of regularization term for the updates can differ due to including/excluding $\boldsymbol{B}$. Additionally, the computation cost of the alternative approach is equivalent to our method, therefore there is no disadvantage to using our more accurate formulation.

SPECT-CT misalignment due to motion may reduce the benefits of the proposed method where CT information was used to determine voxel-level bone volume fractions. Evaluating the new

49

method using XCAT simulations that include motion is potential future work. Moreover, this paper is a proof-of-concept study to demonstrate that the bremsstrahlung generation probabilities can be included in the reconstruction model to improve qualitative and quantitative Y-90 SPECT/CT imaging. However, further investigation of the impact on clinical studies is required. For large homogeneous organs such as the liver, the new model is likely not needed, however, our proposed method becomes important in heterogeneous regions with bone-tissue interfaces.

To conclude, Y-90 SPECT imaging of heterogeneous regions is significantly enhanced by including tissue-dependent bremsstrahlung generation probabilities in the SPECT system matrix without adding substantial computation cost.

CHAPTER 5

Improved Low-Count Quantitative PET Reconstruction With an Iterative Neural Network

Image reconstruction in low-count PET is particularly challenging because gammas from natural radioactivity in Lu-based crystals cause high random fractions that lower the measurement signal-to-noise-ratio (SNR). In model-based image reconstruction (MBIR), using more iterations of an unregularized method may increase the noise, so incorporating regularization into the image reconstruction is desirable to control the noise. New regularization methods based on learned convolutional operators are emerging in MBIR. We modify the architecture of an iterative neural network, *BCD-Net*, for PET MBIR, and demonstrate the efficacy of the trained BCD-Net using XCAT phantom data that simulates the low true coincidence count-rates with high random fractions typical for Y-90 PET patient imaging after Y-90 microsphere radioembolization. Numerical results show that the proposed BCD-Net significantly improves PET reconstruction performance compared to MBIR methods using non-trained regularizers, total variation (TV) and non-local means (NLM). BCD-Net significantly improved CNR and RMSE compared to TV (NLM) regularized MBIR. Moreover, BCD-Net successfully generalizes to data that differs from training data. Improvements were also demonstrated for the clinically relevant phantom measurement data where we used training and testing datasets having very different activity distributions and count-levels.

5.1   Introduction

Image reconstruction in low-count PET is particularly challenging because dominant gammas from natural radioactivity in Lu-based crystals cause high random fractions, lowering the measurement signal-to-noise-ratio (SNR) [20]. To accurately reconstruct images in low-count PET, regularized model-based image reconstruction (MBIR) solves the following optimization problem consisting of *1)* a data fidelity term $f(\boldsymbol{x})$ that models the physical PET imaging system, and *2)* a

---

This chapter is based on [10–12].

regularization term R($\boldsymbol{x}$) that penalizes image roughness and controls noise [85]:

$$\hat{\boldsymbol{x}} = \arg \min_{\boldsymbol{x} \geq \boldsymbol{0}} f(\boldsymbol{x}) + \mathsf{R}(\boldsymbol{x}) \qquad (5.1)$$

$$f(\boldsymbol{x}) := \boldsymbol{1}^T(\boldsymbol{A}\boldsymbol{x} + \bar{\boldsymbol{r}}) - \boldsymbol{y}^T \log(\boldsymbol{A}\boldsymbol{x} + \bar{\boldsymbol{r}}).$$

Here, $f(\boldsymbol{x})$ is the Poisson negative log-likelihood for measurement $\boldsymbol{y}$ and estimated measurement means $\bar{\boldsymbol{y}}(\boldsymbol{x}) = \boldsymbol{A}\boldsymbol{x} + \bar{\boldsymbol{r}}$, the matrix $\boldsymbol{A}$ denotes the system model, and $\bar{\boldsymbol{r}}$ denotes the mean background events such as scatter and random coincidences. Recently, applying learned regularizers to R($\boldsymbol{x}$) is emerging for MBIR [86].

While there is much ongoing research on machine learning or deep-learning techniques applied to CT [37, 38, 87–89] and MRI [40, 41, 90–92] reconstruction problems, fewer studies have applied these techniques to PET. Most past PET studies used deep learning in image space without exploiting the physical imaging model in (5.1). For example, [47] applied a deep neural network (NN) mapping between reconstructed PET images with normal dose and reduced dose and [48] applied a multilayer perceptron mapping between reconstructed images using maximum a posteriori algorithm and a reference (true) image, however, their framework uses the acquisition data only to form the initial image. Therefore, the reconstruction quality depends greatly on the training dataset and information from atypical imaging situations (that are not part of the training set) may not be recovered well, especially when the training dataset size is small [11]. Recently, [93] trained a NN to reconstruct a 2D image directly from PET sinogram and [42, 43] proposed a PET MBIR framework using a deep-learning based regularizer. Our proposed MBIR framework, *BCD-Net*, also uses a regularizer that penalizes differences between the unknown image and "denoised" images given by a regression neural network in an iterative manner. In particular, whereas [42, 43] trained only a single image denoising NN, the proposed method is an iterative framework that includes multiple trained NNs. This iterative framework enables the NNs in the later stages to learn how to recover fine details. Our proposed BCD-Net also differs from [42, 43] in that our denoising NNs are defined by an optimization formulation with a mathematical motivation (whereas, for the trained regularizer, [42, 43] brought U-Net [94] and DnCNN that were [95] developed for medical image segmentation and general Gaussian denoising, respectively) and characterized by fewer parameters, thereby avoiding over-fitting and generalizing well to unseen data especially when training samples are limited.

Iterative NNs [40,41,89,90,96,97] are a broad family of methods that originate from an unrolling algorithm for solving an optimization problem and BCD-Net [98] is a specific example of an iterative NN. BCD-Net is constructed by unfolding a block coordinate descent (BCD) MBIR algorithm using "learned" convolutional analysis operators [99], leading to significantly improved image recovery accuracy in extreme imaging applications, e.g., low-dose CT [39], highly undersampled MRI [98],

denoising low-SNR images [98], etc. A preliminary version of this paper was presented at the 2018 Nuclear Science Symposium and Medical Imaging Conference [12]. We significantly extended this work by applying our proposed method to measured PET data with newly developed techniques. We also added detailed analysis of our proposed method as well as comparisons to related works.

To show the efficacy of our proposed BCD-Net method in low-count PET imaging, we performed both digital phantom simulation and experimental measurement studies with activity distributions and count-rates that are relevant to clinical Y-90 PET imaging after liver radioembolization. Novel therapeutic applications have sparked growing interest in quantitative imaging of Y-90, an almost pure beta emitter that is widely used in internal radionuclide therapy. In addition to the FDA approved Y-90 microsphere radioembolization and Y-90 ibritumomab radioimmunotherapy, there are 50 active clinical trials for Y-90 labeled therapies (www.clinicaltrials.gov). However, the lack of gamma photons complicates imaging of Y-90; it involves SPECT via bremsstrahlung photons produced by the betas [74] or PET via a very low abundance positron in the presence of bremsstrahlung that leads to low signal-to-noise [100]. This paper applies a BCD-Net that is trained for realistic low-count PET imaging environments and compares its performance with those of non-trained regularizers. Our proposed BCD-Net applies to PET imaging in general, particularly in other imaging situations that also have low counts. Using shorter scan times and lower tracer activity in diagnostic PET has cost benefits and reduces radiation exposure, but at the expense of reduced counts that makes traditional iterative reconstruction challenging.

Section 5.2 develops the proposed BCD-Net architecture for PET MBIR. Section 5.2 also explains the simulation studies in the setting of Y-90 radioembolization and provides details on how we perform the physical phantom measurement. Section 5.3 presents how the different reconstruction methods perform with the simulation and measurement data. Section 5.4 discusses what training and imaging factors most affect generalization performance of BCD-Net. Section 5.5 concludes with future works.

5.2 Methods

This section presents the problem formulation of the BCD-Net and gives a detailed derivation that inspires the final form of BCD-Net. We also provide several techniques for BCD-Net that we specifically devised for PET measurement data where each measurement has different count-level (and noise-level). Then we review the related works that we compare with BCD-Net such as MBIR methods using conventional non-trained regularizers. This section also describes the simulation setting and details on the measurement data and what evaluation metrics are used to assess the efficacy of each reconstruction algorithm.
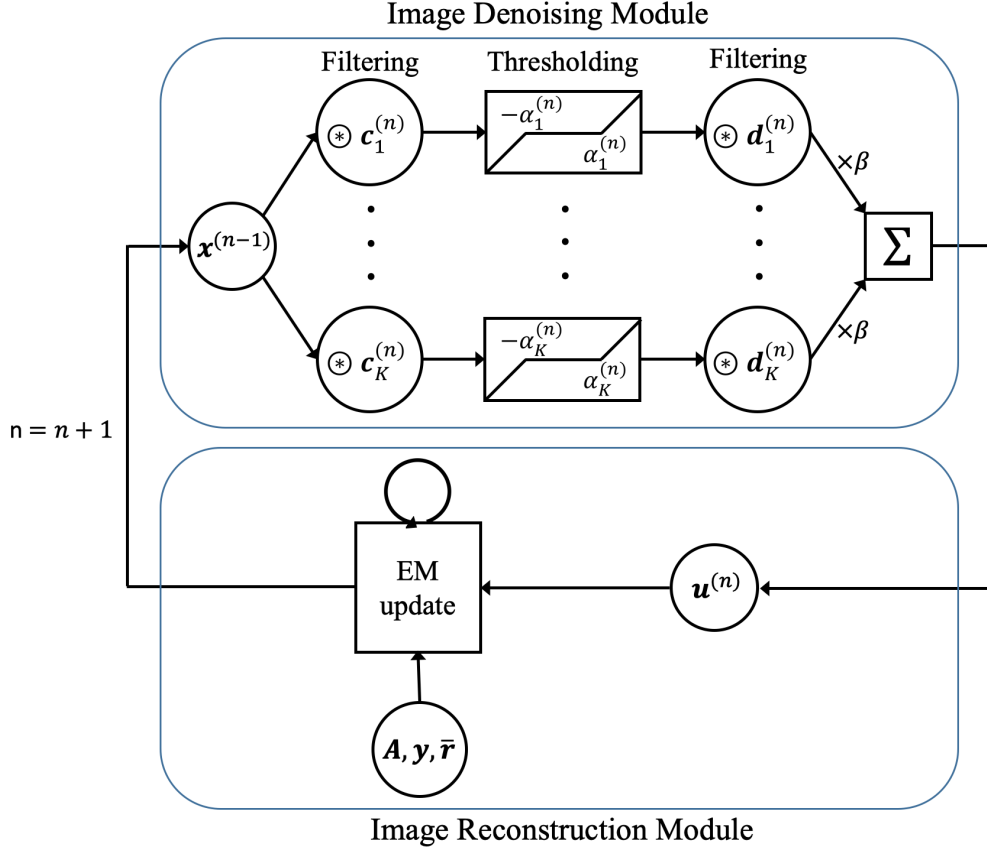
Figure 5.1: Architecture of the proposed BCD-Net for PET. The proposed BCD-Net has an iterative NN architecture: each BCD-Net iteration uses three inputs – fixed measurement and mean background $\{\boldsymbol{y}, \bar{\boldsymbol{r}}\}$, and the image $\boldsymbol{x}^{(n-1)}$ reconstructed at the previous BCD-Net iteration – and provides the reconstructed image $\boldsymbol{x}^{(n)}$.

5.2.1 BCD algorithm for MBIR using "learned" convolutional regularization

Conventional PET regularizers penalize differences between neighboring pixels [101]. That approach is equivalent to assuming that convolving the image with the [1,-1] finite difference filter along different directions produces sparse outputs. Using such "hand-crafted" filters is unlikely to be the best approach. A recent trend is to use training data to learn filters $\boldsymbol{c}_k$ that produce sparse outputs when convolved with images of interest [99, 102, 103]. Such learned filters can be used to define a regularizer that prefers images having sparse outputs, as follows:

$$
\mathsf{R}(\boldsymbol{x}) = \min_{\{\boldsymbol{z}_k\}} \beta \left(\sum_{k=1}^{K} \frac{1}{2} \left\| \boldsymbol{c}_k * \boldsymbol{x} - \boldsymbol{z}_k \right\|_2^2 + \alpha_k \left\| \boldsymbol{z}_k \right\|_1 \right),
\tag{5.2}
$$

where β is regularization parameter, $\{\boldsymbol{c}_k \in \mathbb{R}^R : k = 1, \dots, K\}$ is a set of convolutional filters, $\{\boldsymbol{z}_k \in \mathbb{R}^{n_p} : k = 1, \dots, K\}$ is a set of sparse codes, $\{\alpha_k \in \mathbb{R} : k = 1, \dots, K\}$ is a set of

thresholding parameters controlling the sparsity of $\{z_k\}$, n_p is the number of image voxels, and R and K denote the size and number of learned filters, respectively. BCD-Net is inspired by this type of "learned" regularizer. Ultimately, we hope that the learned regularizer can better separate true signal from noisy components compared to hand-crafted filters.

A natural BCD algorithm solves (5.1) with regularizer (5.2) by alternatively updating $\{z_k\}$ and $\boldsymbol{x}$:

$$\{\boldsymbol{z}_k^{(n+1)}\} = \underset{\{\boldsymbol{z}_k\}}{\operatorname{argmin}} \frac{1}{2} \left\| \boldsymbol{c}_k * \boldsymbol{x}^{(n)} - \boldsymbol{z}_k \right\|_2^2 + \alpha_k \left\| \boldsymbol{z}_k \right\|_1$$

$$= \mathcal{T}(\boldsymbol{c}_k * \boldsymbol{x}^{(n)}, \alpha_k) \tag{5.3}$$

$$\boldsymbol{x}^{(n+1)} = \underset{\boldsymbol{x} \geq 0}{\operatorname{argmin}} f(\boldsymbol{x}) + \frac{\beta}{2} \left(\sum_{k=1}^{K} \left\| \boldsymbol{c}_k * \boldsymbol{x} - \boldsymbol{z}_k^{(n+1)} \right\|_2^2 \right), \tag{5.4}$$

where $\mathcal{T}(\cdot, \cdot)$ is the element-wise soft thresholding operator: $\mathcal{T}(\boldsymbol{t}, q)_j := \operatorname{sign}(t_j) \max(|t_j| - q, 0)$.

Assuming that learned filters $\{\boldsymbol{c}_k\}$ satisfy the tight-frame condition, $\sum_{k=1}^{K} \|\boldsymbol{c}_k * \boldsymbol{x}\|_2^2 = \|\boldsymbol{x}\|_2^2 \ \forall \boldsymbol{x}$, we rewrite the updates in (5.3)-(5.4) as follows:

$$\boldsymbol{u}^{(n+1)} = \sum_{k=1}^{K} \tilde{\boldsymbol{c}}_k * \left(\mathcal{T} \left(\boldsymbol{c}_k * \boldsymbol{x}^{(n)}, \alpha_k \right) \right) \tag{5.5}$$

$$\boldsymbol{x}^{(n+1)} = \underset{\boldsymbol{x} \geq 0}{\operatorname{argmin}} f(\boldsymbol{x}) + \frac{\beta}{2} \left\| \boldsymbol{x} - \boldsymbol{u}^{(n+1)} \right\|_2^2, \tag{5.6}$$

where $\tilde{\boldsymbol{c}}_k$ denotes a rotated version of $\boldsymbol{c}_k$. For efficient image reconstruction (5.6) in PET, we use the standard EM-surrogate of Poisson log-likelihood function [35]:

$$f(\boldsymbol{x}) + \frac{\beta}{2} \left\| \boldsymbol{x} - \boldsymbol{u}^{(n+1)} \right\|_2^2$$

$$= \sum_{i=1}^{n_d} [\boldsymbol{A}\boldsymbol{x}]_i + \bar{r}_i - y_i \log([\boldsymbol{A}\boldsymbol{x}]_i + \bar{r}_i) + \frac{\beta}{2} \sum_{j=1}^{n_p} (x_j - u_j^{(n+1)})^2$$

$$\leq \sum_{j=1}^{n_p} \left\{ -e_j(\boldsymbol{x}^{(n')})(x_j^{(n')}) \log(x_j) + a_j x_j + \frac{\beta}{2} (x_j - u_j^{(n+1)})^2 \right\}$$

$$= \sum_{j=1}^{n_p} Q_j(x_j)$$

where n' denotes n'th inner-iteration in (5.6), $e_j(\boldsymbol{x}^{(n')}) = \sum_{i=1}^{n_d} a_{ij} \frac{y_i}{\bar{y}_i(\boldsymbol{x}^{(n')})}$, a_{ij} denotes an element of the system model at ith row and jth column, and n_d is the number of rays. Equating $\frac{\partial Q_j(x_j)}{\partial x_j}$ to

Algorithm 1 BCD-Net for PET MBIR

Require:
$\{\boldsymbol{c}_k^{(n)}, \boldsymbol{d}_k^{(n)}, \alpha_k^{(n)} : n = 1, \ldots, T\}, \boldsymbol{y}, \bar{\boldsymbol{r}}, \boldsymbol{A}, \beta$

Initialize:
$\boldsymbol{x}^{(0)}$ using EM algorithm
Calculate $a_j = \sum_{i=1}^{n_d} a_{ij}$
for $n = 0, \ldots, T - 1$ **do**
$\quad \boldsymbol{u}^{(n+1)} = \sum_{k=1}^{K} \boldsymbol{d}_k^{(n+1)} * \left(\mathcal{T} \left(\boldsymbol{c}_k^{(n+1)} * \boldsymbol{x}^{(n)}, \alpha_k^{(n+1)} \right) \right)$
$\quad$ **for** $n' = 0, \ldots, T' - 1$ **do**
$\quad\quad \lambda = \frac{1}{2}(a_j - \beta u_j^{(n+1)})$
$\quad\quad \nu = x_j^{(n')} \left(\sum_{i=1}^{n_d} a_{ij} \frac{y_i}{\bar{y}_i(\boldsymbol{x}^{(n')})} \right)$
$\quad\quad x_j^{(n'+1)} = \begin{cases} \frac{\sqrt{\lambda^2 + \beta\nu} - \lambda}{\beta}, & \lambda < 0 \\ \frac{\nu}{\sqrt{\lambda^2 + \beta\nu} + \lambda}, & \lambda \geq 0 \end{cases}$
$\quad$ **end for**
$\quad \boldsymbol{x}^{(n+1)} = \boldsymbol{x}^{(T')}$
end for

---

zero is equivalent to finding the root of the following quadratic formula:

$$\beta x_j^2 + \left(a_j - \beta u_j^{(n+1)} \right) x_j - e_j(\boldsymbol{x}^{(n')}) x_j^{(n')} = 0,$$

and finding the root [36] leads to the minimizer:

$$x_j^{(n'+1)} = \begin{cases} \frac{\sqrt{\lambda^2 + \beta\nu} - \lambda}{\beta}, & \lambda < 0 \\ \frac{\nu}{\sqrt{\lambda^2 + \beta\nu} + \lambda}, & \lambda \geq 0, \end{cases}$$

where $\lambda = \frac{1}{2}(a_j - \beta u_j^{(n+1)})$, $\nu = e_j(\boldsymbol{x}^{(n')}) x_j^{(n')}$, $a_j = \sum_{i=1}^{n_d} a_{ij}$.

5.2.2 BCD-Net for PET MBIR and its training

To further improve denoising capability by providing more trainable parameters, we extend the convolutional autoencoder in (5.5), by replacing $\{\tilde{\boldsymbol{c}}_k\}$ with separate decoding filters $\{\boldsymbol{d}_k\}$. We *define* BCD-Net to use the following updates for each iteration:

$$\boldsymbol{u}^{(n+1)} = \sum_{k=1}^{K} \boldsymbol{d}_k^{(n+1)} * \left(\mathcal{T} \left(\boldsymbol{c}_k^{(n+1)} * \boldsymbol{x}^{(n)}, \alpha_k^{(n+1)} \right) \right) \tag{5.7}$$

$$\boldsymbol{x}^{(n+1)} = \underset{\boldsymbol{x} \geq \boldsymbol{0}}{\operatorname{argmin}} f(\boldsymbol{x}) + \frac{\beta}{2} \left\| \boldsymbol{x} - \boldsymbol{u}^{(n+1)} \right\|_2^2, \tag{5.8}$$

where separate encoding and decoding filters $\{c_k\}$ and $\{d_k\}$ are learned for each iteration. Fig. 5.1 shows the corresponding BCD-Net architecture. We refer to the u and x updates in (5.7)-(5.8) as two *modules*: 1) image denoising module and 2) image reconstruction module. The final output image is from the reconstruction module. Algorithm (1) gives detailed pseudocode of the proposed method. T denotes the total number of outer-iterations and T' denotes the number of inner iterations used for (5.8). We use $x^{(n)}$ as the initial image when solving (5.8).

The image denoising module consists of encoding and decoding filters $\{c_k^{(n)}\}$, $\{d_k^{(n)}\}$ and thresholding values $\{\alpha_k^{(n)}\}$. We train these parameters to "best" map from noisy images into high-quality reference images (e.g., true images if available) in the sense of mean squared error (Section 5.4 compares the ℓ_1 loss):

$$\underset{\{c_k\},\{d_k\},\{\alpha_k\}}{\text{argmin}} \sum_{l=1}^{L} \left\| x_{\text{true},l} - \sum_{k=1}^{K} d_k * \left(\mathcal{T}\left(c_k * x_l^{(n)}, \alpha_k \right) \right) \right\|_2^2, \tag{5.9}$$

where L is the total number of training samples, $\{x_{\text{true},l} \in \mathbb{R}^{n_p} : l = 1, \dots, L\}$ is a set of true images and $\{x_l^{(n)} \in \mathbb{R}^{n_p} : l = 1, \dots, L\}$ is a set of images estimated by image reconstruction module in the nth iteration. We train the set of filters and thresholding values iteration-by-iteration, therefore, there is no need to consider the system matrix or sinograms when training using (5.9). Moreover, we do not enforce the tight-frame condition when training the filters.

One can further extend the convolutional autoencoder in (5.7) to a general regression NN, e.g., a deep U-Net [94]. We investigated if the iterative BCD-Net combined with U-Net denoisers (by replacing the denoising module in (5.7) with a U-Net) performs better than the proposed BCD-Net using convolutional autoencoder denoiser (5.7). Section 5.2.7.2 gives the details of the U-Net implementation.

5.2.3   BCD-Net for measurement data in PET

5.2.3.1   Normalization and scaling scheme

Different PET images can have very different intensity values due to variations in scan time and activity, and it is important for trained methods to be able to generalize to a wide range of count levels. Towards this end, we implemented normalization and scaling techniques in BCD-Net. [42] extended [43] by implementing "local linear fitting" to ensure that the denoising NN output has similar intensity as the input patch from the current estimated image. Our approach is different in that we normalize and scale the image with a global approach, not a patch-based approach. In

particular, we modify the architecture in (5.7)-(5.8) as:

$$\boldsymbol{u}^{(n+1)} = \sum_{k=1}^{K} \boldsymbol{d}_k^{(n+1)} * \left(\mathcal{T}_{\alpha_k^{(n+1)}} \left(\boldsymbol{c}_k^{(n+1)} * g_1(\boldsymbol{x}^{(n)}) \right) \right) \tag{5.10}$$

$$\boldsymbol{x}^{(n+1)} = \underset{\boldsymbol{x} \geq \boldsymbol{0}}{\operatorname{argmin}} \; f(\boldsymbol{x}) + \frac{\beta}{2} \left\| \boldsymbol{x} - g_2(\boldsymbol{u}^{(n+1)}) \right\|_2^2, \tag{5.11}$$

where the normalization function $g_1(\cdot)$ is defined by $g_1(\boldsymbol{v}) := \frac{1}{\sum_j \bar{v}_j} \bar{\boldsymbol{v}}$ to ensure that $\mathbf{1}^T g_1(\boldsymbol{v}) = 1$, and the scaling function $g_2(\cdot)$ is defined by $g_2(\boldsymbol{v}) := \operatorname{argmin}_s f(s \cdot \boldsymbol{v}) \boldsymbol{v}$. We solve the optimization problem over s using Newton's method:

$$
\begin{aligned}
s^{(n+1)} &= s^{(n)} - \frac{\nabla_s f(s^{(n)} \cdot \boldsymbol{v})}{\nabla_s^2 f(s^{(n)} \cdot \boldsymbol{v})} \\
&= s^{(n)} - \frac{\sum_{i=1}^{n_d} [\boldsymbol{A}\boldsymbol{v}]_i - y_i \frac{[\boldsymbol{A}\boldsymbol{v}]_i}{s^{(n)}[\boldsymbol{A}\boldsymbol{v}]_i + \bar{r}_i}}{\sum_{i=1}^{n_d} y_i \left(\frac{[\boldsymbol{A}\boldsymbol{v}]_i}{(s^{(n)}[\boldsymbol{A}\boldsymbol{v}]_i + \bar{r}_i)} \right)^2}.
\end{aligned}
\tag{5.12}
$$

To be consistent with the modified convolutional autoencoder in (5.10), we also apply this image-based normalization technique when training the convolutional filters and thresholding values:

$$\underset{\{\boldsymbol{c}_k\},\{\boldsymbol{d}_k\},\{\alpha_k\}}{\operatorname{argmin}} \sum_{l=1}^{L} \left\| g_1(\boldsymbol{x}_{\text{true},l}) - \sum_{k=1}^{K} \boldsymbol{d}_k * \left(\mathcal{T}_{\alpha_k} \left(\boldsymbol{c}_k * g_1(\boldsymbol{x}_l^{(n)}) \right) \right) \right\|_2^2.$$

5.2.3.2 Adaptive regularization parameter scheme

The best regularization parameter value can also vary greatly between scans, depending on the count level. Therefore, instead of choosing one specific value for the regularization parameter, we set the β value for each iteration based on evaluation on current gradients of data-fidelity term and regularization term:

$$
\begin{aligned}
\beta^{(n')} &= \frac{\left\| \nabla_{\boldsymbol{x}} f(\boldsymbol{x}^{(n')}) \right\|_2}{\left\| \nabla_{\boldsymbol{x}} \mathsf{R}(\boldsymbol{x}^{(n')}) \right\|_2} \cdot c \\
&= \frac{\left\| a_j - e_j(\boldsymbol{x}^{(n')}) \right\|_2}{\left\| \boldsymbol{x}^{(n')} - g_2(\boldsymbol{u}^{(n+1)}) \right\|_2} \cdot c, \quad n' = 1, \dots, T',
\end{aligned}
\tag{5.13}
$$

where c is a constant specifying how we balance between the data-fidelity term and regularization term and n' denotes n'th inner-iteration in solving (5.11).

Table 5.1: Details on XCAT simulation data: variations between training and testing data.

	Training data	Testing data
Concentration ratio (hot:warm)	9:1	4:1
Total net trues	200 K	500 K
Random fraction (%)	90.9	87.5

Table 5.2: Details on phantom measurement data: activity concentration ratio between hot and warm regions and randoms fractions for two phantom studies.

	Sphere	Liver-torso
Total activity (GBq)	0.65	1.9
Concentration ratio (hot:warm)	8.9:1	5.4:1
Total prompts	3.2 - 6.3 M	2.3 M
Total randoms	2.9 - 5.7 M	2.1 M
Total net trues	308 - 599 K	220 K
Random fraction(%)	90.3 - 90.5	90.7

5.2.4 Conventional MBIR methods: Non-trained regularizers

We compared the proposed BCD-Net with two MBIR methods that use standard non-trained regularizers.

5.2.4.1 Total-variation (TV)

TV regularization penalizes the sum of absolute value of differences between adjacent voxels:

$$\mathsf{R}(\boldsymbol{x}) = \beta \left\| \boldsymbol{C} \boldsymbol{x} \right\|_1,$$

where $\boldsymbol{C}$ is finite differencing matrix. Recent work [104] applied Primal-Dual Hybrid Gradient (PDHG) [105] for PET MBIR using TV regularization and demonstrated that PDHG-TV is superior than clinical reconstruction (e.g., OS-EM) for low-count datasets in terms of several image quality evaluation metrics such as contrast recovery and variability.

5.2.4.2 Non-local means (NLM)

NLM regularization penalizes the differences between nearby patches in image:

$$\mathsf{R}(\boldsymbol{x}) = \beta \sum_{i,j \in S_i} p \left(\left\| \boldsymbol{N}_i \boldsymbol{x} - \boldsymbol{N}_j \boldsymbol{x} \right\|_2^2 \right),$$

Table 5.3: Details on typical patient measurement data: total trues and randoms fractions.

	Patient A
Total activity (GBq)	2.55
Total prompts	2.7 M
Total randoms	2.3 M
Total net trues	380 K
Random fraction(%)	85.8

where $p(t)$ is a potential function of a scalar variable t, S_i is the search neighborhood around the ith voxel, and $\mathbf{N}_i$ is a patch extraction operator at the ith voxel. We used the Fair potential function for $p(t)$:

$$p(t) = \sigma_f^2 \left(\sqrt{\frac{t}{\sigma_f^2 N_f}} + \log\left(1 + \sqrt{\frac{t}{\sigma_f^2 N_f}} \right) \right),$$

where σ_f is a design parameter and N_f is the number of voxels in the patch $\mathbf{N}_i \mathbf{x}$. Unlike conventional local filters that assume similarity between only adjacent voxels, NLM filters can average image intensities over distant voxels. As in [106], we used ADMM to accelerate algorithmic convergence with an adaptive penalty parameter selection method [60].

5.2.5 Experimental setup: Digital phantom simulation and experimental measurement

5.2.5.1 Y-90 PET/CT XCAT simulations

We used the XCAT [84] phantom (Fig. 5.2) to simulate Y-90 PET following radioembolization. We set the image size to $128 \times 128 \times 100$ with a voxel size $4.0 \times 4.0 \times 4.0$ (mm^3) and chose 100 slices ranging from lung to liver. To simulate extremely low count scans with high random fractions, typical for Y-90 PET, we set total true coincidences and random fractions based on numbers from patient PET imaging performed after radioembolization [5]. To test the generalization capability of the trained BCD-Net, we changed all imaging factors between training and testing dataset. Here, imaging factors include activity distribution (shape and size of tumor and liver background, concentration ratio between hot and warm region) and count-level (total true coincidences and random fraction). Fig. 5.2 and Table 5.1 provide details on how we changed the testing dataset from the training dataset. We trained BCD-Net using five pairs ($L = 5$) of 3D true images and estimated images at each iteration (1 true image, 5 realizations). We generated multiple realizations to train the denoising NN to deal with the Poisson noise. We also generated 5 realizations (1 true image, 5 realizations) as a testing dataset to evaluate the noise across realizations.

5.2.5.2 Y90 PET/CT physical phantom measurements and patient scan

For training BCD-Net, we used PET measurements of a sphere phantom (Fig. 5.4) where six 'hot' spheres (2,4,8,16,30 and 113 mL, 0.5 MBq/ml) are placed in a 'warm' background (0.057 MBq/ml) with total activity of 0.65 GBq. The phantom was scanned for 40 (3 acquisitions) - 80 (1 acquisition) $(L = 4)$ minutes on a Siemens Biograph mCT PET/CT. For testing BCD-Net and other reconstruction algorithms, we used an anthropomorphic liver/lung torso phantom (Fig. 5.4) with total activity and distribution that is clinically realistic for imaging following radioembolization with Y-90 microspheres: 5% lung shunt, 1.17 MBq/mL in liver, 3 hepatic lesions (4 and 16 mL spheres, 29 mL ovoid) of 6.6 MBq/ml. The phantom with total activity of 1.9 GBq was scanned for 30 minutes on a Siemens Biograph mCT PET/CT. Fig. 5.4 and Table 5.2 provide details on the count-level (random fraction) and activity distribution differences between training (sphere phantom) and testing (liver phantom) dataset. We also tested BCD-Net with an actual Y-90 patient scan and Table 5.3 provides count-level information.

We acquired all measurement data with time of flight TOF information. The measurement data size is $200{\times}168{\times}621{\times}13$. The last dimension of measurement indicates the number of time bin. The reconstructed image size is $200{\times}200{\times}112$ with a voxel size $4.07{\times}4.07{\times}2.03$ (mm^3). To reconstruct the image with measurement data, we used a SIEMENS TOF system model ($\boldsymbol{A}$ in (5.1)) along with manufacturer given attenuation/normalization correction, PSF modelling, and randoms/scatters estimation.

5.2.6 Evaluation metrics

For the XCAT phantom simulation, we evaluated each reconstruction with contrast recovery (CR) (volume-of-interest (VOI): cold region), noise across realizations, root mean squared error (RMSE), and contrast to noise ratio (CNR). For the physical phantom measurement, we used CR (VOI: hot spheres) and CNR averaged over multiple hot spheres. For the patient measurement, we used the field of view (FOV) activity bias since the total activity in FOV is known (equal to the injected activity because the microspheres are trapped) wheareas the activity distribution is
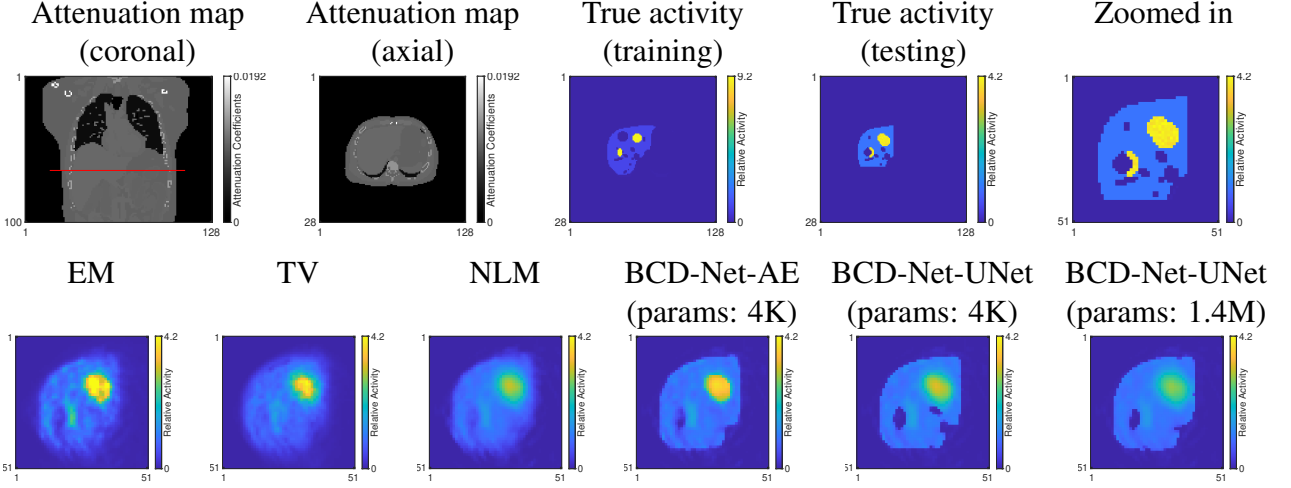
Figure 5.2: XCAT phantom simulation: (First row) coronal and axial view of attenuation map and true relative activity distribution corresponding to axial attenuation map. (Second row) reconstructed images of one slice from different reconstruction methods. BCD-Net-AE/UNet is the BCD-Net with autoencoder/UNet denoiser and params indicates the number of trainable parameters.

unknown:

$$\text{CR (VOI: cold region)} = \left(1 - \frac{C_{\text{VOI}}}{C_{\text{BKG}}}\right) \times 100 \ (\%)$$

$$\text{CR (VOI: hot sphere)} = \frac{\frac{C_{\text{VOI}}}{C_{\text{BKG}}} - 1}{R_{\text{True}} - 1} \times 100 \ (\%)$$

$$\text{Noise} = \frac{\sqrt{\frac{1}{J_{\text{Liver}}} \sum_{j \in \text{Liver}} \left(\frac{1}{M-1} \sum_{m=1}^{M} (\hat{\boldsymbol{x}}_m[j] - \frac{1}{M} \sum_{m'=1}^{M} \hat{\boldsymbol{x}}_{m'}[j])^2\right)}}{\frac{1}{J_{\text{Liver}}} \sum_{j \in \text{Liver}} \boldsymbol{x}_{\text{true}}[j]} \times 100 \ \%$$

$$\text{RMSE} = \sqrt{\frac{\sum_j (\boldsymbol{x}_{\text{true}}[j] - \hat{\boldsymbol{x}}[j])^2}{J_{\text{FOV}}}} \times 100 \ (\%)$$

$$\text{CNR} = \frac{C_{\text{Lesion}} - C_{\text{BKG}}}{\text{STD}_{\text{BKG}}}$$

$$\text{FOV bias} = \frac{\sum_j \hat{\boldsymbol{x}}[j] - \boldsymbol{x}_{\text{true}}[j]}{\sum_j \boldsymbol{x}_{\text{true}}[j]} \times 100 \ (\%),$$

where C_{VOI} is mean counts in the VOI, R_{True} is true ratio between hot and warm region, M is the number of realizations and J_{Liver} is the number of voxels in the volume of liver, STD_{BKG} is standard deviation between voxel values in uniform background liver, and J_{FOV} is the total number of voxels in the FOV.
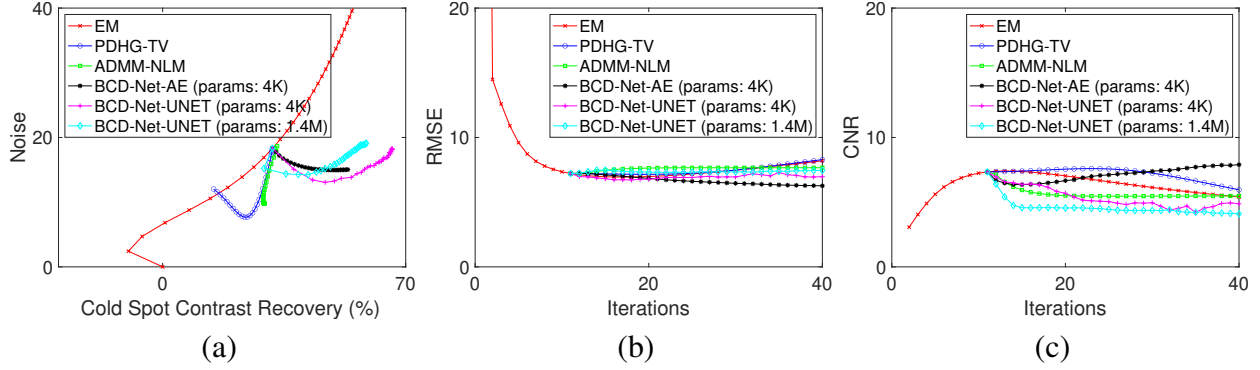
Figure 5.3: (a) Plot of noise in background liver vs contrast recovery in cold spot (b) RMSE vs iteration (c) Contrast to noise ratio vs iteration. We initialized regularized methods with the 10th iterate of EM reconstruction.

5.2.7 Training details

We trained the denoising network in each iteration with a stochastic gradient descent method using the PyTorch [107] deep-learning library.

5.2.7.1 BCD-Net with convolutional autoencoder

We trained a BCD-Net with a convolutional autoencoder where each iteration has 78 sets of thresholding values and convolutional encoding/decoding filters ($K = 78$). We set the size of each filter as $3 \times 3 \times 3$ ($R = 3^3$), and set the initial thresholding values by sorting the initial estimate of image and getting a 10% largest value of sorted initial image. We used the Adam optimization method [108] to train the NN with a learning rate of 10^{-2}. We used 500 epochs to train the denoising NN at each iteration. We applied the learning rate decay scheme (e.g., decreasing the learning rate as a factor of 0.1 at 400 epochs). Due to the large size of 3D input, we set the batch size as 1.

5.2.7.2 BCD-Net with U-Net

We implemented a 3-D version of U-Net. The 'encoder' part of U-Net consists of multiple sets of 1) average pooling layer, 2) $3 \times 3 \times 3$ convolutional layer, 3) batch normalization (BN) layer, 4) ReLU layer and the 'decoder' part of U-Net consists of multiple sets of 1) upsampling with trilinear interpolation [43], 2) $3 \times 3 \times 3$ convolutional layer, 3) BN layer, 4) ReLU layer. We used a ReLU layer as the last step to enforce the image non-negativity constraint [43]. There are long skip connections between encoder part and decoder part. For training the U-Net, we used the same training dataset that we used for training the convolutional autoencoder. We also used the Adam optimization method with learning rate of 10^{-3} and using identical settings (number of epochs, learning rate decay, batch size) as those of the convolutional autoencoder. We trained and tested two
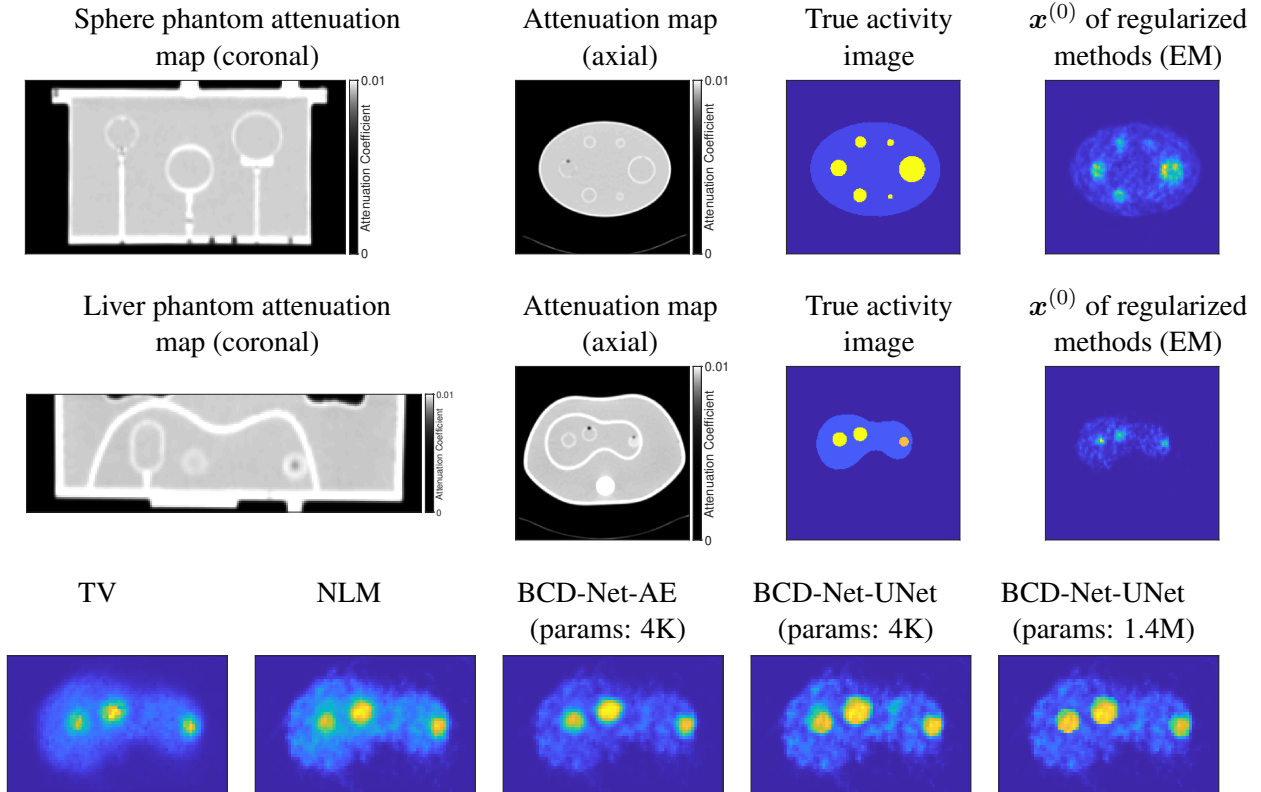
Figure 5.4: Y90 PET/CT physical phantom measurement: (First row: training data, Second row: testing data) Attenuation map, true activity, and $x^{(0)}$ of regularized methods of sphere and liver phantom used for training and testing BCD-Net. (Third row) Reconstructed images of one slice from different reconstruction methods.

different U-Nets sizes. At each BCD-Net iteration, the U-Net has either about 4 K (similar size to the convolutional autoencoder) or 1.4 M trainable parameters. We set the number of convolutional filter channels of the first encoder layer as 12 with 4 times of contraction/expansion for the U-Net with 1.4 M parameters and 5 with 1 time of contraction/expansion for the U-Net with 4 K parameters.

5.3 Results

5.3.1 Reconstruction setup

We compared the proposed BCD-Net method to the standard EM (1 subset), TV-based MBIR with PDHG algorithm (PDHG-TV), and NLM-based MBIR with ADMM algorithm (ADMM-NLM). For regularized MBIR methods including BCD-Net, we used 10 EM algorithm iterations to get the initial image $x^{(0)}$. For each regularization method, we finely tuned the regularization parameter β (within range $[2^{-15}, 2^{15}]$) to maximize the CNR. For NLM, we additionally tuned
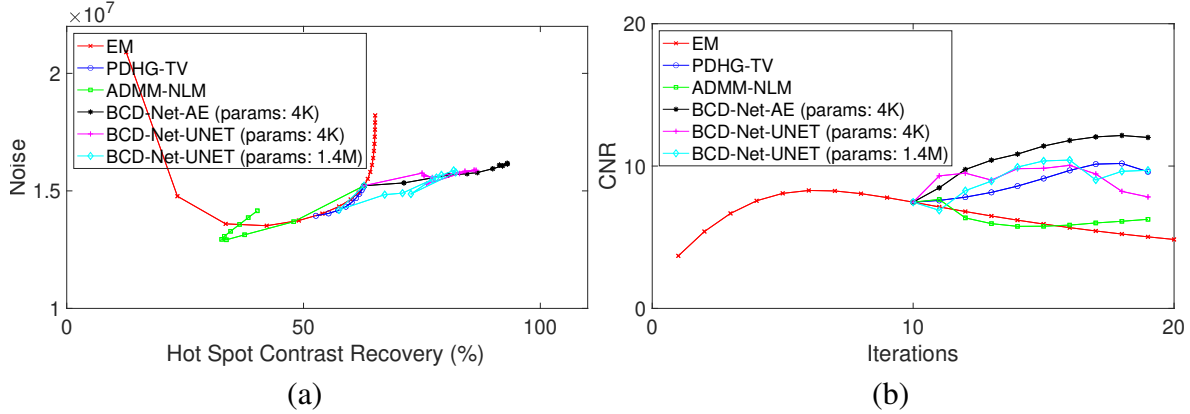
Figure 5.5: (a) Plot of noise in background liver vs contrast recovery in hot spheres (b) Contrast to noise ratio vs iteration. We initialized regularized methods with the 10th iterate of EM reconstruction.

the window and search sizes. For the XCAT simulation data, we used 40 iterations for EM and 30 iterations ($T = 30$) for PDHG-TV, ADMM-NLM, and BCD-Net. We used 1 inner-iteration ($T' = 1$) for the reconstruction module (5.8) for each outer-iteration of BCD-Net. For the measured data, we used 20 iterations for EM and 10 iterations ($T = 10$) for PDHG-TV, ADMM-NLM, and BCD-Net. We used 1 inner-iteration ($T' = 1$) for the reconstruction module (5.11) during each outer-iteration of BCD-Net. We set $c = 0.005$ in (5.13) in both the phantom measurement and patient studies.

5.3.2 Results: Reconstruction (testing) on simulation data

Fig. 5.2-5.3 shows that the proposed iterative NN, BCD-Net, significantly improves overall reconstruction performance over the other non-trained regularized MBIR methods. Fig. 5.3 reports averaged evaluation metrics over realizations. Fig. 5.3 shows that BCD-Net with a trained convolutional autoencoder achieves the best results in most evaluation metrics. In particular, BCD-Net with a convolutional autoencoder improves CNR and RMSE compared to PDHG-TV and ADMM-NLM. BCD-Net also improved contrast recovery in the cold region while not increasing noise compared to the initial EM reconstruction, whereas PHDG-TV and ADMM-NLM improved noise while degrading the CR. For Fig. 5.2, we selected the iteration number for EM to obtain the highest CNR and the last iteration number for other methods. Fig. 5.2shows that BCD-Net's reconstructed image with a convolutional autoencoder is closest to the true image whereas PHDG-TV and ADMM-NLM exceedingly blur the cold region. BCD-Net with the U-Net denoiser shows good recovery for the cold region, however, it blurs the hot region. Moreover, the larger sized U-Net (params: 1.4 M) denoiser worsens the performance of BCD-Net possibly due to over-fitting the training dataset.

65
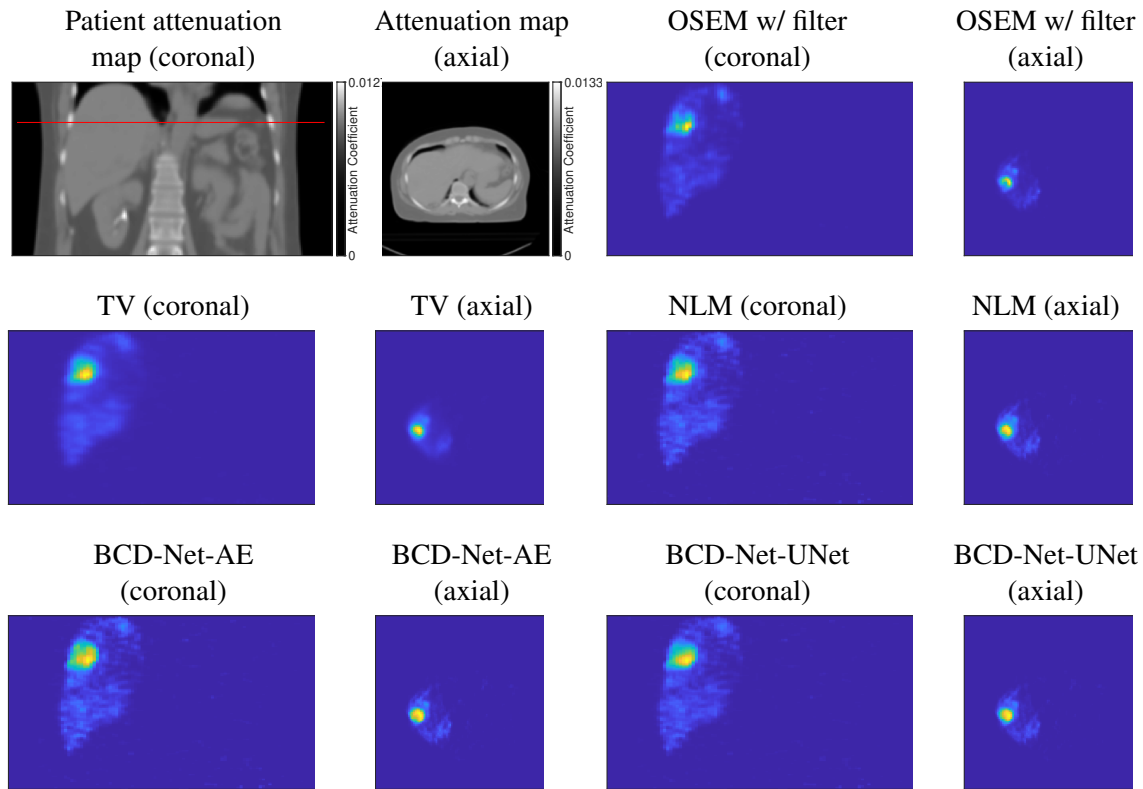
Figure 5.6: Y90 PET/CT patient measurement: Attenuation map and reconstructed images of one slice (coronal and axial view) using OSEM, TV, NLM, and BCD-Net. We visualized the reconstructed image of BCD-Net-UNet with 4 K parameters

5.3.3 Results: Reconstruction (testing) on measurement data

5.3.3.1 Phantom study

Similar to the simulation results, Fig. 4-5 shows that, BCD-Net improved overall reconstruction performance over the other reconstruction methods. Fig. 5.4 shows that reconstructed images using PHDG-TV and ADMM-NLM show uniform texture in background liver compared to EM, however, those exceedingly blur around hot spheres. The blurred hot region is more evident in the quantification results in Fig. 5.5. BCD-Net gives more visibility for hot spheres with noisier texture in uniform liver region. Fig. 5.5 shows that BCD-Net with a convolutional autoencoder improves CNR compared to PDHG-TV and ADMM-NLM. BCD-Net with autoencoder also improved contrast recovery in hot spheres while slightly increasing noise compared to the initial EM reconstruction. In Fig. 5.5(a), BCD-Net with U-Net denoiser shows a fluctuation with iterations, however, the plot trend is similar to that of BCD-Net with autoencoder.
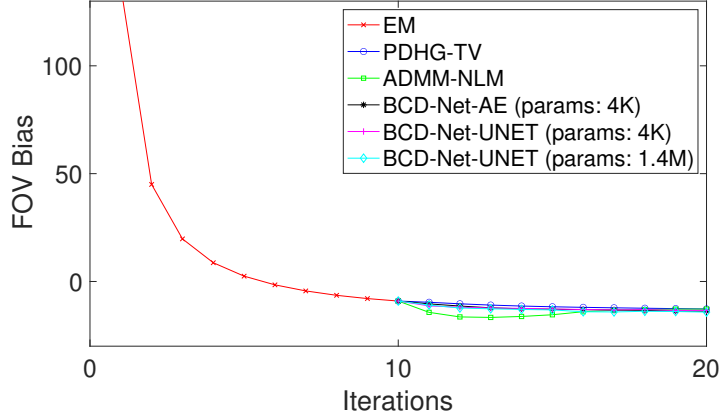
Figure 5.7: Field of view bias vs iteration. BCD-Net shows similar results compared to other methods.

5.3.3.2 Patient study

Because of the unknown true activity distribution, we quantitatively evaluated each reconstruction method with FOV activity bias. In this quantitative evaluation, BCD-Net showed similar results compared to other methods. See Fig. 5.6-5.7. Fig. 5.6 shows that the quality of image using different methods in patient study is similar to that of phantom measurement study shown in Fig. 5.4.

5.4 Discussion

In this study we showed the efficacy of trained BCD-Net on both qualitative and quantitative Y-90 PET/CT imaging and compared between conventional non-trained regularizers. The proposed approach uses learned denoising NNs to lift estimated signals and thresholding operations to remove unwanted signals. In particular, the iterative framework of BCD-Net enables one to train the filters and thresholding values to deal with the different image roughness at its each iteration. We experimentally demonstrate its generalization capabilities with simulation and measurement data. In the XCAT PET/CT simulation with activity distributions and count-rates mimicking Y-90 PET imaging, total counts in the VOI were significantly underestimated with standard reconstruction and other MBIR methods using non-trained regularization, yet approached the true activity with the proposed approach. Improvements were also demonstrated for the measurement data where we used training and testing datasets having very different activity distribution and count-levels. The architecture and size of denoising NN significantly affect the performance of BCD-Net. In both simulation and measurement experiments, the convolutional autoencoder outperformed the U-Net architectures. Using a U-Net with more trainable parameters degraded the performance, especially

Table 5.4: Impact of imaging variable on generalization capability of BCD-Net.

Changed imaging variable	Training	Testing	RMSE	Drop (%)
Identical	-		4.74	-
Shape and size	See Fig. 5.2		5.49	15.9
Concentration ratio	9:1	4:1	5.55	17.1
Concentration ratio	1.7:1	4:1	5.81	22.5
Trues Count-level	2×10^5	5×10^5	5.01	5.7
Trues Count-level	11×10^5	5×10^5	5.71	20.5

in the simulation study, due to the small size of dataset. Size of the denoising NN should be set with consideration of training dataset size. Our approach is not limited to Y-90 PET but is generalizable, as we showed by applying to low count SPECT. In [11] where we applied the proposed method to Lu-177 low count SPECT, BCD-Net significantly improved contrast between hot lesions and warm liver while reducing noise, thereby improving CNR. BCD-Net improved lesion CNR by 21.8/32.9/96.0 (%), AR by 9.2/4.0/35.0 (%), and RMSE by 0.6/9.5/9.3 (%) compared to EM/TV/U-Net. U-Net denotes non-iterative deep neural network denoiser (single forward pass). Bias - noise plots showed that BCD-Net decreases noise while improving AR unlike the conventional regularizer and EM. In patient studies, qualitative comparison showed that low-count BCD-Net reconstruction better matched the high-count images compared to other reconstructions.

We tested which imaging variable most affects the generalization performance of the proposed BCD-Net. Table 5.4 shows how BCD-Net performs when training and testing data had the same activity distribution and count-level (only difference is Poisson noise) and how the performance of BCD-Net is degraded when each imaging variable is changed between training and testing dataset. We changed one of three factors (shape and size of tumor and liver, concentration ratio, count-level) in training dataset compared to testing dataset. The result shows that generalization performance of the proposed BCD-Net depends largely on all imaging variables. However, training with higher contrast and lower count-level dataset (compared to testing dataset) gave less degradation of performance compared to the opposite cases. This result suggests that it is better to have noisier data in training dataset than testing dataset. In other words, training for extra noise reduction than needed is better than less noise reduction than needed.

We also investigated how each factor in training of denoising module (5.7), i.e., convolutional autoencoder, impacts the generalization capability of BCD-Net. Fig. 5.8(a)-(b) show the impact of number and size of filters on performance. Plots show that the proposed BCD-Net achieved lower training RMSE when using larger number and size of filters; however, it did not decrease testing RMSE compared to smaller number and size of filters and BCD-Net with larger size of filter exceedingly blurs image thereby resulting in higher RMSE. See Fig. 5.8(e). This result well

(a) Impact of number of filter
(Fixed $R = 3^3$)

(b) Impact of size of filter
(Fixed $K = 2^5$)

(c) Trained with ℓ_1 loss   (d) $K = 2^4$ (e) $R = 9^3$
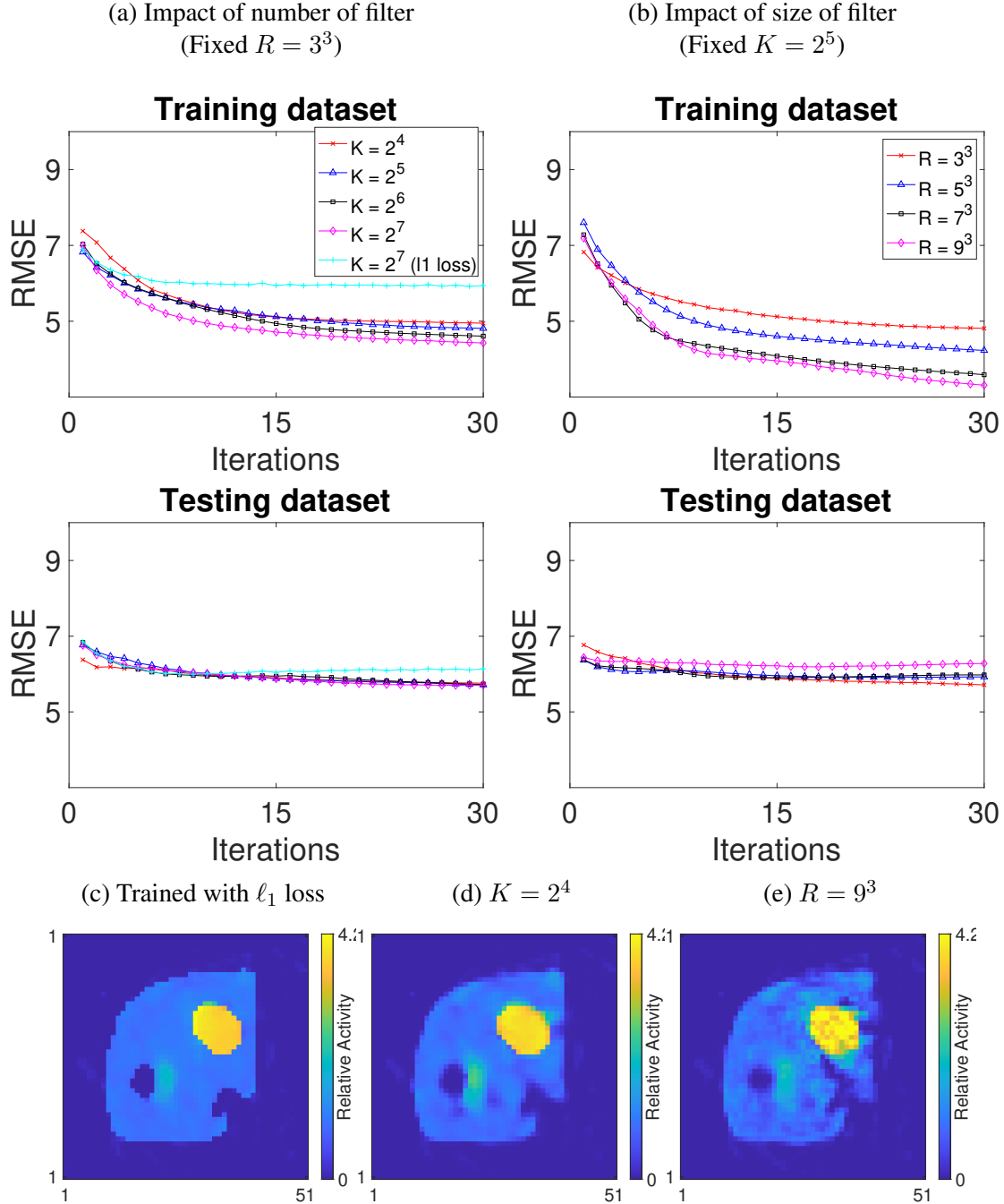
Figure 5.8: (a)-(b) Impact of number/size of filter and training loss on testing dataset RMSE. (c) Reconstructed image from BCD-Net with filters and thresholding values trained with ℓ_1-loss.

corresponds to the result in Section 5.3 related to the parameter dimension of NN. We also tested ℓ_1 training loss to see if it improves the performance over the ℓ_2 loss (MSE) in (5.9). However, it led to unnaturally piece-wise constant images and details in small cold regions were ignored.

Fig. 5.9 shows how the regularization parameter β in (5.13) changes with iterations in training
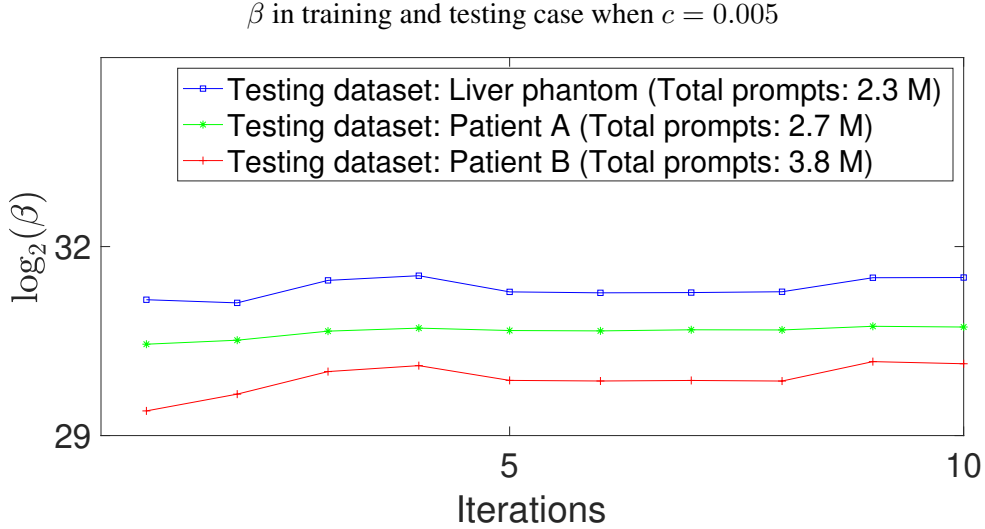
Figure 5.9: Efficacy of adaptive selection of regularization parameter β.

and testing datasets. The β value in each iteration converges to different limits in training and testing cases. The adaptive scheme automatically increases the β value when the count-level decreases. This behavior concurs with the general knowledge that more regularization is needed when the noise-level increases. These empirical results underscore the importance of such adaptive regularization parameter selection schemes proposed in Section 5.2.3.2 in PET imaging.

To analyze what is being learned by the denoising network, Fig. 5.10 (presented in [12]) visualizes each step in a denoising network. When visualizing, we sorted the thresholding values in the ascending order, therefore the upper ones are least shrunk outputs and the lower ones are most shrunk outputs. In both Fig. 5.10(a)-(b), some filters and thresholding values are trained to smooth the image and detect edges with small gradients (see upper ones) and some filters and thresholding values are trained to detect edges with large gradients (see lower ones).

5.5 Conclusion

It is important for a "learned" regularizer to have generalization capability to help ensure good performance when applying it to an unseen dataset. For low-count PET reconstruction, the proposed iterative NN, BCD-Net, showed reliable generalization capability even when the training dataset is small. The proposed BCD-Net achieved significant qualitative and quantitative improvements over the conventional MBIR methods using "hand-crafted" non-trained regularizers: TV and NLM. In particular, these conventional MBIR methods have a trade-off between noise and recovery accuracy, whereas the proposed BCD-Net improves CR for hot regions while not increasing the noise when the regularization parameter is appropriately set. Visual comparisons of the reconstructed images also show that the proposed BCD-Net significantly improves PET image reconstruction performance
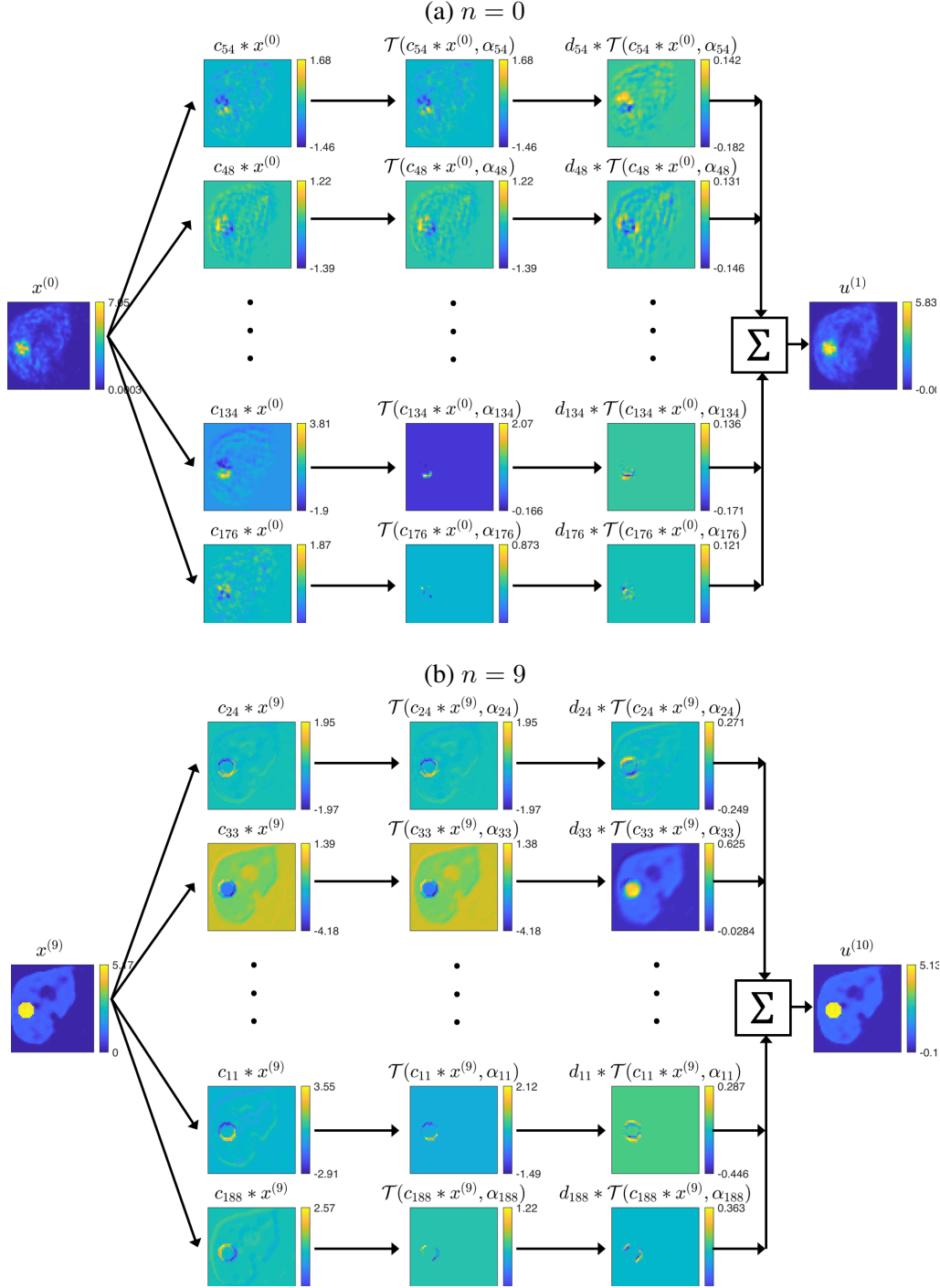
Figure 5.10: Visualization of each step in denoising network (filtering-thresholding-filtering) at (a) early outer-iteration ($n = 0$) and (b) later outer-iteration ($n = 9$).

compared to MBIR methods using non-trained regularizers.

Future work includes investigating performance of BCD-Net trained with end-to-end training principles and adaptive selection of trainable parameter numbers depending on the size of training

71

dataset.

CHAPTER 6

SPECT Reconstruction With Trained Regularizer Using CT-Side Information

Improving low-count SPECT can lead to shorter scans and enable pre-therapy theranostic imaging for dosimetry based treatment planning in therapies with radionuclides such as Lu-177 (208 keV gamma: 10%) that have low photon yields. Conventional mathematically designed regularization methods tend to perform poorly in the low-count setting, so incorporating trained regularization into the model-based image reconstruction is desirable to improve image quality and quantification. However, most existing trained regularizers do not fully exploit the information from dual-modality system like SPECT-CT. For SPECT reconstruction, we propose a trained regularizer that uses segmentation based on CT image. The trained regularizer incorporates the CT information using the segmentation mask generated by a trained segmentation network. To train the segmentation network, we used Liver Tumor Segmentation Challenge dataset where a segmentation mask indicates liver and tumor region. To train the SPECT regularizer, we used four Lu-177 patient studies with multiple acquisitions on a Symbia SPECT-CT. Patient images are acquired at 1-5 days after 7.4 GBq Lu-177 DOTATATE therapy for neuroendocrine tumors. To test the trained network, we used the Lu-177 phantom and patient studies not used for training. We compared between standard unregularized EM algorithm, conventional regularization using CT-side information, and our proposed method. The proposed method significantly improved contrast-to-noise-ratio and activity quantification compared with other methods. Enhancing low-count SPECT as demonstrated here has potential application in pre-treatment theranostic imaging, imaging at late time points after therapy, whole body SPECT, and reducing SPECT acquisition times in general.

6.1 Introduction

Improving low-count SPECT to reduce noise, to reduce scan time or enable whole-body imaging is particularly relevant when imaging radionuclides that have low photon intensities such as ^{177}Lu (208 keV gamma: 10%) [23] and ^{90}Y ($\leq$ 5% bremsstrahlung yield) [8]. In dosimetry applications

---

This chapter is based on [13].

73

low count-rates are encountered when imaging at later time points to determine pharmacokinetics following a therapeutic administration. Furthermore, ultra-low count rates are encountered when imaging pre-therapy for dosimetry based treatment planning. However, low count-rate quantitative imaging is challenging due to high noise that is particularly problematic for voxel level dose estimation. To improve reconstruction for low-count SPECT, regularized model-based image reconstruction (MBIR) has been widely used. Applying "learned" regularizers to MBIR significantly improved image quality and quantification in medical image reconstruction with application of CT [37–39] and MRI [40, 41] compared to "mathematically designed" regularizers. Several studies have applied these techniques to emission tomography [10, 11, 42, 43]. Although there has been much research on incorporating anatomical information into emission tomography [109–133] most existing trained regularizers for emission tomography do not fully exploit the information from dual-modality system like SPECT-CT or PET-MR.

Incorporating anatomical information into emission tomography can be beneficial because anatomical images have better resolution than emission images and offer accurate boundary information. Since PET or SPECT tracer distribution is likely smooth within organ boundaries, many existing methods that use anatomical information for emission tomography are based on regularizers that encourage spatial smoothness inside boundary region and enforce less smoothing across boundaries. Since many learning-based methods for medical image reconstruction are "unrolled" versions of iterative optimization methods [134], we revisited "using anatomical information" for SPECT reconstruction. Specifically, the present work is a trained version of [110] and [126]. Those two works used a modified quadratic regularizer with finite differences between neighboring voxel values. "Modified" means that it uses CT-side information as a regularization weight (zero-valued at boundary) to prevent penalizing the voxel value differences where the boundary is located. In the present work, instead of using finite differencing matrix, we used trained convolutional operators. Moreover, since trained convolutional filters can differ from finite differencing operators, CT-side information is not incorporated as boundary indicator image. We determine the regularization weight directly from filtered segmentation mask (indicates whether each voxel belongs to liver or tumor class). The segmentation mask is generated by the fully automatic segmentation network where its input is CT image.

To show its efficacy, we applied the proposed method to patient studies using ^{177}Lu DOTATATE, a targeted radionuclide therapy (TRT) that was recently FDA approved for treatment of neuroendocrine tumors (NETs). This therapy is administered to patients in four cycles with fixed activity. Internally administered TRT with radio-labelled targeting molecules that deliver cytotoxic radiation to tumor has been used successfully to treat multiple cancers. ^{177}Lu is preferentially delivered to tumor cells by DOTATATE, which binds to the somatostatin receptors expressed by most well-differentiated NETs [16]. A randomized trial [17] demonstrated a markedly longer progression

74
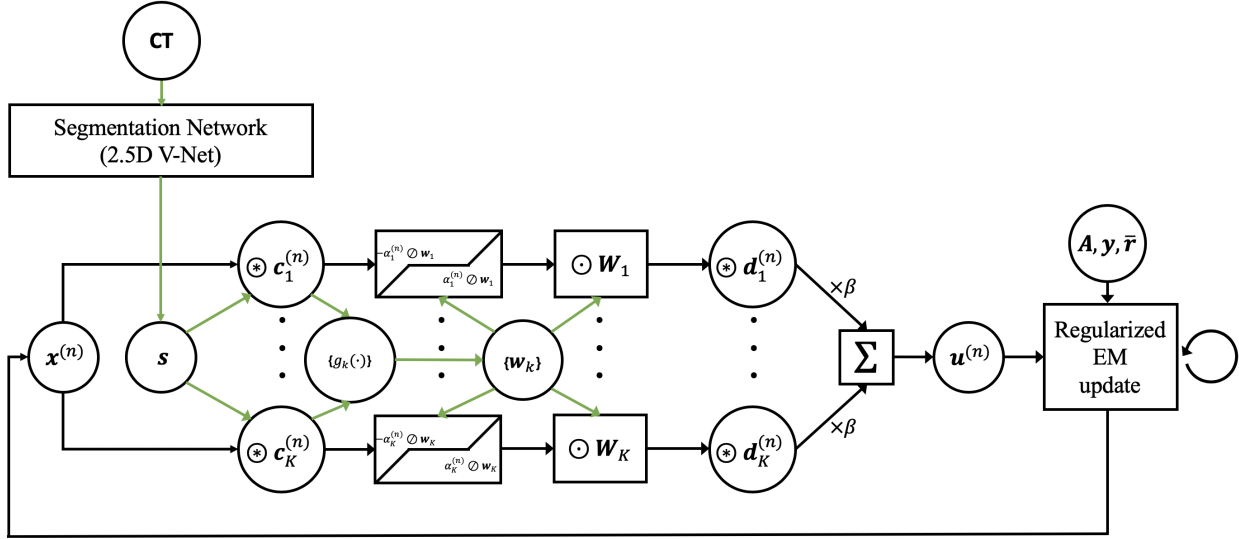
Figure 6.1: High-level block diagram of our proposed method. Influence of CT-side information for SPECT reconstruction is indicated with green arrows.

free survival (PFS) with ^{177}Lu DOTATATE than the control group receiving the non-radioactive DOTATATE, the current standard of care. ^{177}Lu, used increasingly in TRT, emits both beta particles that deliver the therapeutic effect and gamma rays suitable for SPECT imaging of the activity distribution. The proposed method can be adapted to therapies with other radionuclides and targeting agents that can benefit from SPECT-CT imaging based treatment planning such as radioligand therapy with ^{177}Lu PSMA for prostate cancer.

Section 6.2 describes the proposed method, which we develop with trained regularizer using CT-side information for SPECT MBIR. Section 6.2 also provides details on how we perform the physical phantom measurement and how we created training and testing dataset. Section 6.3 presents how the different reconstruction methods perform with the Lu-177 SPECT measurement data. Section 6.4 discusses how the proposed method takes advantage of CT-side information. Section 6.5 concludes with future works.

6.2 Methods

This section presents the problem formulation of the proposed method and gives a detailed derivation that inspires the final form. Then we review the related works that we compare with the proposed method such as conventional regularized MBIR methods using CT-side information. This section also provides details on the measurement data and what evaluation metrics are used to assess the efficacy of each reconstruction algorithm.

6.2.1 A trained regularization method using CT-side information

Regularized MBIR has been widely used to improve reconstruction quality of low-count SPECT:

$$\hat{\boldsymbol{x}} = \arg \min_{\boldsymbol{x} \geq \boldsymbol{0}} f(\boldsymbol{x}) + \beta \mathsf{R}(\boldsymbol{x}) \tag{6.1}$$

$$f(\boldsymbol{x}) := \mathbf{1}^T (\boldsymbol{A}\boldsymbol{x} + \bar{\boldsymbol{r}}) - \boldsymbol{y}^T \log(\boldsymbol{A}\boldsymbol{x} + \bar{\boldsymbol{r}}),$$

where $\boldsymbol{x}$ is the unknown SPECT image, $f(\boldsymbol{x})$ is Poisson negative log-likelihood for measurement $\boldsymbol{y}$ and estimated measurement means $\bar{\boldsymbol{y}}(\boldsymbol{x}) = \boldsymbol{A}\boldsymbol{x} + \bar{\boldsymbol{r}}$, the matrix $\boldsymbol{A}$ denotes the system model, $\bar{\boldsymbol{r}}$ denotes the mean background events such as the additive scatter contribution, $\mathsf{R}(\boldsymbol{x})$ is a regularization term to control the noise, and β is the regularization parameter. Most existing mathematically designed SPECT regularizers penalize differences between neighboring pixels [106, 135]. Using such "hand-crafted" filters is not likely to be optimal. Recently, applying "trained" regularizers to MBIR significantly improved image quality and quantification in medical image reconstruction. However, most existing trained regularizers for emission tomography do not fully exploit the information from dual-modality system like SPECT-CT or PET-MR. In the present work, instead of using single-modality based regularizer $\mathsf{R}(\boldsymbol{x})$, we propose to use multi-modality based regularizer $\mathsf{R}(\boldsymbol{x}; \boldsymbol{s})$ which is exploiting anatomical side information provided by segmentation "mask" variable $\boldsymbol{s}$. A segmentation network generates $\boldsymbol{s}$, where its input is CT image acquired simultaneously with SPECT measurement. The regularization term is composed of trained convolutional operations and a 1-norm to promote sparsity:

$$\mathsf{R}(\boldsymbol{x}; \boldsymbol{s}) = \min_{\boldsymbol{z}} \sum_{k=1}^{K} \frac{1}{2} \left\| \boldsymbol{c}_k * \boldsymbol{x} - \boldsymbol{z}_k \right\|_{\boldsymbol{W}_k}^2 + \alpha_k \left\| \boldsymbol{z}_k \right\|_1, \tag{6.2}$$

where $\boldsymbol{W}_k = \mathrm{diag}\{\boldsymbol{w}_k\}$, $\boldsymbol{w}_k = g_k(\boldsymbol{c}_k * \boldsymbol{s})$, $\{\boldsymbol{c}_k : k = 1, ..., K\}$ is a set of convolution filters, $*$ denotes convolution operation, $\{\boldsymbol{z}_k : k = 1, ..., K\}$ is a set of sparse codes, and K is the number of filters. As illustrated in Fig. 6.2, $g_k(\cdot)$ is an activation function for filtered segmentation mask and we define it as follows:

$$g_k(\nu) = \frac{2e^{-\kappa_k \nu^2}}{e^{-\kappa_k \nu^2} + 1}, \tag{6.3}$$

where κ_k is a trainable parameter. When $\boldsymbol{c}_k * \boldsymbol{s}$ is equivalent to convolving the segmentation mask with the [1,-1] finite difference filter along different directions, the diagonal weighting matrix $\boldsymbol{w}_k$ will be zero-valued at the boundaries, hence it would avoid smoothing across boundaries between different regions [110, 121].

A traditional optimization approach for solving (6.1) with (6.2) would be to use a block
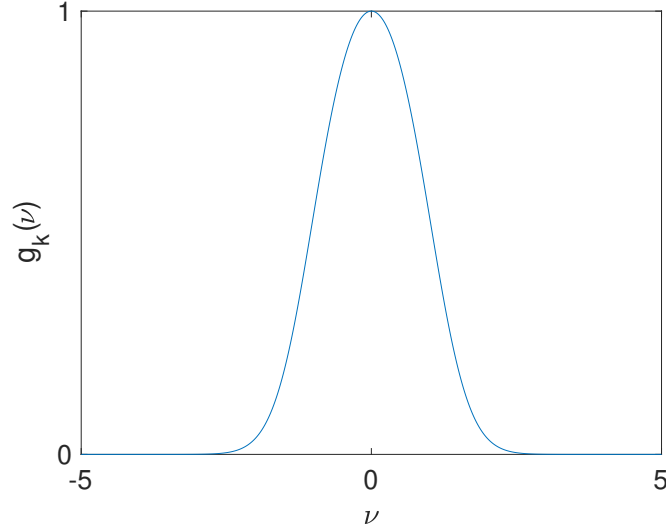
Figure 6.2: Activation function $g_k(\cdot)$ for $\kappa_k = 1$. κ_k is a trainable parameter that changes the width of the function.

coordinate descent algorithm that alternatively updates $\{z_k\}$ and x :

$$z_k^{(n+1)} = \operatorname*{argmin}_{z_k} \frac{1}{2} \left\| c_k * x^{(n)} - z_k \right\|_{W_k}^2 + \alpha_k \|z_k\|_1 = \mathcal{T}(c_k * x^{(n)}, \alpha_k \oslash w_k) \qquad (6.4)$$

$$x^{(n+1)} = \operatorname*{argmin}_{x} f(x) + \frac{\beta}{2} \sum_{k=1}^K \left\| c_k * x - z_k^{(n+1)} \right\|_{W_k}^2, \qquad (6.5)$$

where $\mathcal{T}(\cdot, \cdot)$ is the element-wise soft thresholding operator:

$$\mathcal{T}(t, q)_j := \operatorname{sign}(t_j) \max(|t_j| - q_j, 0). \qquad (6.6)$$

When trained filters $\{c_k\}$ satisfy $\sum_{k=1}^K C_k^T W_k C_k = I$ where C_k is a sparse convolution matrix satisfying $C_k x \iff c_k * x$, updates in (6.4)-(6.5) can be rewritten as the following equivalent variable updates:

$$u^{(n+1)} = \sum_{k=1}^K \tilde{c}_k * \left(W_k \big(\mathcal{T}(c_k * x^{(n)}, \alpha_k \oslash w_k) \big) \right) \qquad (6.7)$$

$$x^{(n+1)} = \operatorname*{argmin}_{x} f(x) + \frac{\beta}{2} \left\| x - u^{(n+1)} \right\|_2^2, \qquad (6.8)$$

where $\tilde{c}_k$ is a reversed version of c_k.

For the trained approach considered in this work, we use separate decoding filters $\{d_k\}$ instead

77

of using $\{\tilde{c}_k\}$ to have more trainable parameters. Moreover, we use iteration-dependent filters and thresholding values so that the learned method can deal with different level (or type) of artifact at each iteration. Inspired by (6.7), hereafter, we define the variable updates as follows:

$$\boldsymbol{u}^{(n+1)} = \sum_{k=1}^{K} \boldsymbol{d}_k^{(n+1)} * \left(\boldsymbol{W}_k \big(\mathcal{T}(\boldsymbol{c}_k^{(n+1)} * \boldsymbol{x}^{(n)}, \alpha_k^{(n+1)} \oslash \boldsymbol{w}_k)) \big) \right) \tag{6.9}$$

$$\boldsymbol{x}^{(n+1)} = \underset{\boldsymbol{x}}{\operatorname{argmin}} \, f(\boldsymbol{x}) + \frac{\beta}{2} \left\| \boldsymbol{x} - \boldsymbol{u}^{(n+1)} \right\|_2^2, \tag{6.10}$$

where separate encoding and decoding filters $\{\boldsymbol{c}_k^{(n)}\}$ and $\{\boldsymbol{d}_k^{(n)}\}$ are learned for the nth iteration. Our proposed framework alternatively updates the reconstructed image $\boldsymbol{x}$ and the denoised image $\boldsymbol{u}$ with convolution filters and soft-thresholding values trained at each iteration. Fig. 6.1 illustrates the corresponding architecture.

In the training phase, we train the set of filters $\{\boldsymbol{c}_k\}$, $\{\boldsymbol{d}_k\}$, soft-thresholding values $\{\alpha_k\}$, and the parameters $\{\kappa_k\}$ for the activation function in (6.3) to map the the image estimate from the previous iteration into a high quality image (e.g., EM reconstruction with high-count measurement) at each iteration:

$$\underset{\{\boldsymbol{c}_k\},\{\boldsymbol{d}_k\},\{\alpha_k\},\{\kappa_k\}}{\operatorname{argmin}} \sum_{l=1}^{L} \left\| \boldsymbol{x}_{\text{true},l} - \sum_{k=1}^{K} \boldsymbol{d}_k * \boldsymbol{W}_k \left(\mathcal{T} \left(\boldsymbol{c}_k * \boldsymbol{x}_l^{(n)}, \alpha_k \oslash \boldsymbol{w}_k \right) \right) \right\|_2^2 \tag{6.11}$$

where L is the total number of training samples, $\{\boldsymbol{x}_{\text{true},l} : l = 1, \ldots, L\}$ is a set of high quality images and $\{\boldsymbol{x}_l^{(n)} : l = 1, \ldots, L\}$ is a set of images estimated in the nth iteration. We do not enforce the equivalence condition $\sum_{k=1}^{K} \boldsymbol{C}_k^T \boldsymbol{W}_k \boldsymbol{C}_k = \boldsymbol{I}$ when training the filters.

6.2.2 Neural network for CT segmentation

For the image segmentation network, we implemented a 2.5-D version of V-Net [136] because training takes much more time when implemented in 3-D. The V-Net architecture adds residual connections to that of U-Net [94]. Those architectures consist of a sequence of encoding blocks and followed by a sequence of decoder blocks. The encoding block consists of multiple sets of pooling layer (or convolutional layer with strides), convolutional layer, ReLU lyaer, and batch normalization layer and the decoder block replaces pooling layer with upsampling using interpolation (or transposed convolution). In the present work, we concatenated 4 adjacent slices (2 upper, 2 lower) to the slice being segmented to consider the context with nearby slices (the number of input channel is 5). Fig. 6.3 illustrates the V-Net architecture.
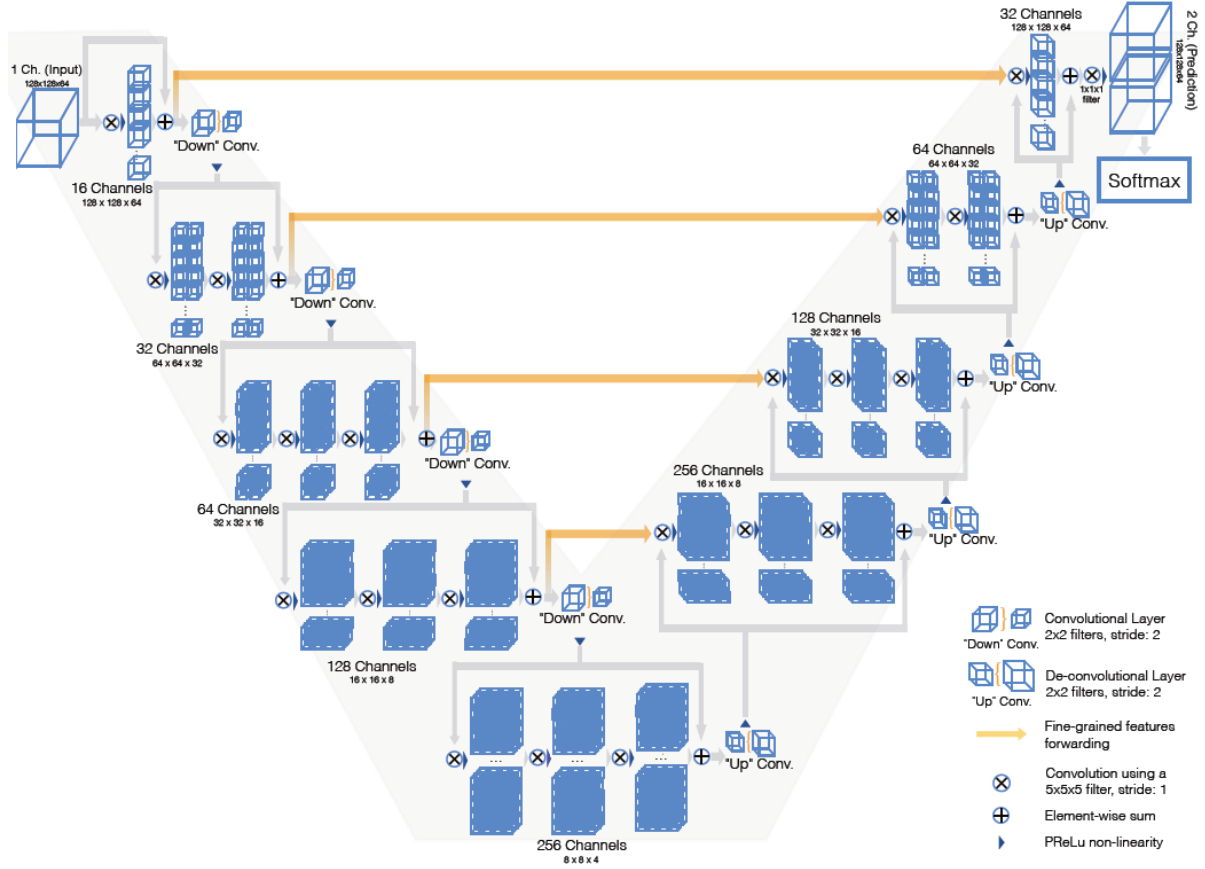
Figure 6.3: Architecture of V-Net

6.2.3 Conventional non-trained regularizer using CT-side information

We compared the proposed method with a conventional non-trained quadratic regularizer and a quadratic regularizer using CT-side information [110, 126]. The regularization using CT-side information modifies the quadratic regularizer $\mathsf{R}(\boldsymbol{x}) = \frac{\beta}{2} \sum_{k=1}^{K} \left\| \check{\boldsymbol{C}}_k \boldsymbol{x} \right\|_2^2$ as follows:

$$\mathsf{R}(\boldsymbol{x}) = \frac{\beta}{2} \sum_{k=1}^{K} \left\| \check{\boldsymbol{C}}_k \boldsymbol{x} \right\|_{\boldsymbol{W}_k}^2. \tag{6.12}$$

Here, $K = 3$ and $\check{\boldsymbol{C}}_k$ is finite differencing matrix along one of x, y, z directions. $\boldsymbol{W}_k = \mathrm{diag}\{\boldsymbol{w}_k\}$ and $\boldsymbol{w}_k = g(\check{\boldsymbol{C}}_k \boldsymbol{s})$. We used the identical segmentation mask $\boldsymbol{s}$ provided for the proposed method and $g(\cdot)$ as in (6.3) without trainable parameter κ_k.

79

6.2.4 Dataset for CT segmentation network

Because ^{177}Lu DOTATATE is for the treatment of neuroendocrine tumors mostly located in liver (83% of ^{177}Lu DOTATATE patients have liver metastases [17]) and healthy liver also absorbs relatively high doses, liver is the main region of interest. Therefore, we used LiTS (Liver Tumor Segmentation) dataset [137] to train the segmentation network to segment the liver and tumor region based on abdominal CT. Fig. 6.4(a)-(b) shows an example training CT image and the corresponding label image provided by the dataset.

6.2.5 Dataset for SPECT denoising network

To train the denoising network with given segmentation mask, we used four Lu-177 patient studies with multiple acquisitions and a measurement using a phantom that has six hot spheres (2,4,8,16,30 and 113 mL) in a warm background. Patient images are acquired at 1-5 days after 7.4 GBq Lu-177 DOTATATE therapy. To generate low-count realizations in training dataset (L=30), we resampled [138] the regular 25-minutes measurement data with Poisson resampling rate of 4% to generate 1-minute equivalent scan this is ultra-low count rates so need to emphasize pre-therapy imaging application. To test BCD-Net, we used a Lu-177 phantom measurement with hot spheres ('lesions') in the warm liver of a torso-phantom with a clinically realistic activity distribution and one additional patient study not used for training.

Table 6.1: Primary counts range in training dataset: 1 phantom study and 4 patients (patient A, B, C, D) studies with multiple acquisition time points

	Count-level	Day0	Day5
Patient	High (25-minutes)	12.3M - 26.5M	2.7M - 6.1M
Patient (resampled)	Low (1-minute)	492K - 1.1M	150K - 250K
Sphere Phantom (resampled)	Low	1.3M	

Table 6.2: Primary counts in testing dataset: 1 phantom studies and 1 patient (patient E) study

	Primary Counts
Patient	109K
Liver Phantom	370K

6.2.6 Training denoising and segmentation networks

6.2.6.1 SPECT denoising network: Sparse convolutional autoencoder

We trained 3D convolutional filters and thresholding values for each iteration using the PyTorch (version 1.2) [107] deep-learning library. We trained a 5 outer-iteration network where each outer-iteration has $K = 100$ (maximum number with available GPU memory) sets of thresholding values and convolutional encoding/decoding filters. We set the size of each filter to be $3 \times 3 \times 3$. We use Adam optimization method to train the network. We used 500 epochs to train the denoising network at each outer-iteration. We applied a learning rate decay method (learning rate = learning rate $\times$ 0.9 at 20 epoch).

6.2.6.2 Segmentation network: V-Net

For training V-Net, we also used Adam optimization method with learning rate of 10^{-3}. We use 16 convolutional filter channels for the first encoding layer, with four times of contraction and four times of expansion. We used weighted cross entropy loss for training and set the weight for each class based on the fraction of each class in the training dataset (if the proportion of each class is a:b:c, we set the weights as [(a+b+c)/a,(a+b+c)/b,(a+b+c)/c] for each class).

6.2.7 Evaluation metrics

For the physical phantom measurement, we evaluated SPECT reconstruction performance with activity recovery (AR, VOI: hot spheres) and image-ensemble-noise across realizations. For the patient measurement, since the true activity distribution is unknown, we used the contrast-to-noise ratio (CNR):

$$\text{AR} = \frac{\text{Estimated } C_{\text{VOI}}}{\text{True } C_{\text{VOI}}} \times 100(\%)$$

$$\text{Noise}_{\text{BKG}} = \frac{\sqrt{\frac{1}{J_{\text{BKG}}} \sum_{j \in \text{BKG}} \left(\frac{1}{M-1} \sum_{m=1}^{M} (\hat{\boldsymbol{x}}_m[j] - \frac{1}{M} \sum_{m'=1}^{M} \hat{\boldsymbol{x}}_{m'}[j])^2 \right)}}{\frac{1}{J_{\text{BKG}}} \sum_{j \in \text{BKG}} \frac{1}{M} \sum_{m=1}^{M} \hat{\boldsymbol{x}}_m[j]} \times 100 \,\%$$

$$\text{CNR} = \frac{C_{\text{Lesion}} - C_{\text{Liver}}}{\text{Noise}_{\text{Liver}}},$$

where C_{VOI} is mean counts in the volume of interest (VOI), M is total number of realizations, and J_{BKG} is the total number of voxels in uniform background region.

We report the segmentation performance with global Dice similarity coefficient [137] for the

| LiTS CT | LiTS Label | Lu-177 Patient CT | Patient Segmentation |

(a) (b) (c) (d)
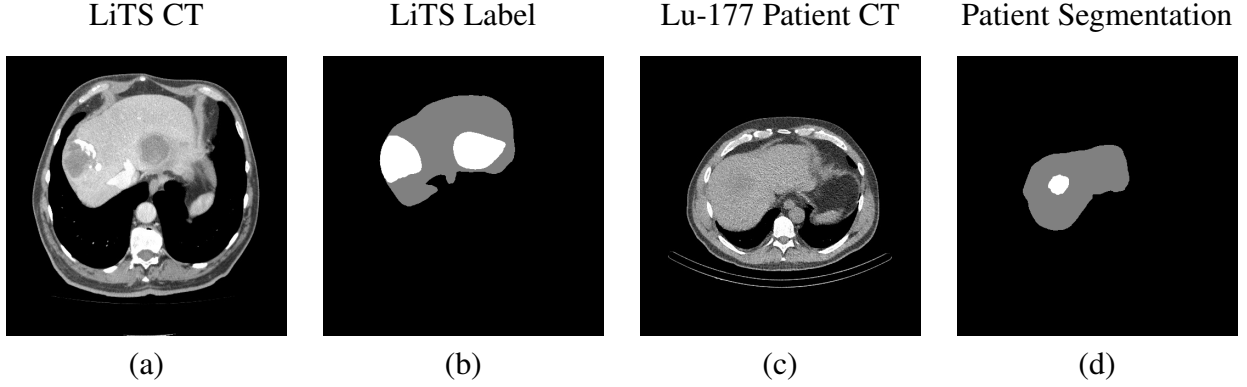
Figure 6.4: LiTS dataset provides CT image (a) in HU unit and label image (b) (tumor:2, liver:1) corresponding to CT. (c) is the one of Lu-177 patients CT images acquired on a Symbia SPECT-CT and (d) is segmentation result corresponding to (c) generated by the segmentation network trained on LiTS dataset.

Table 6.3: Evaluation result on LiTS test dataset.

Method	Global DICE tumor	Global DICE liver
V-Net (used in the present work)	0.77	0.94
First place in leader board	0.86	0.97

LiTS test dataset:

$$\mathrm{Dice}(A, B) = \frac{2|A \cap B|}{|A| + |B|},$$

where A is a estimated segmentation mask and B is a true segmentation mask.

6.3   Results

We compare between standard EM, quadratic regularization (QR), quadratic regularization using CT-side information (QR-CT) described in Section 6.2.3, and the proposed method. For regularized methods including the proposed method, we used 50 EM algorithm iterations to get the initial image $x^{(0)}$. We used 15 iterations for the conventional regularizers and 5 (3) outer (inner) iterations for the proposed method. When reporting evaluation results (Fig. 6.5-6.6), we selected the regularization parameter for each regularized method to obtain the highest CNR.

| TRUE | EM | QR | QR-CT | Proposed |

| High-count EM | EM | QR | QR-CT | Proposed |
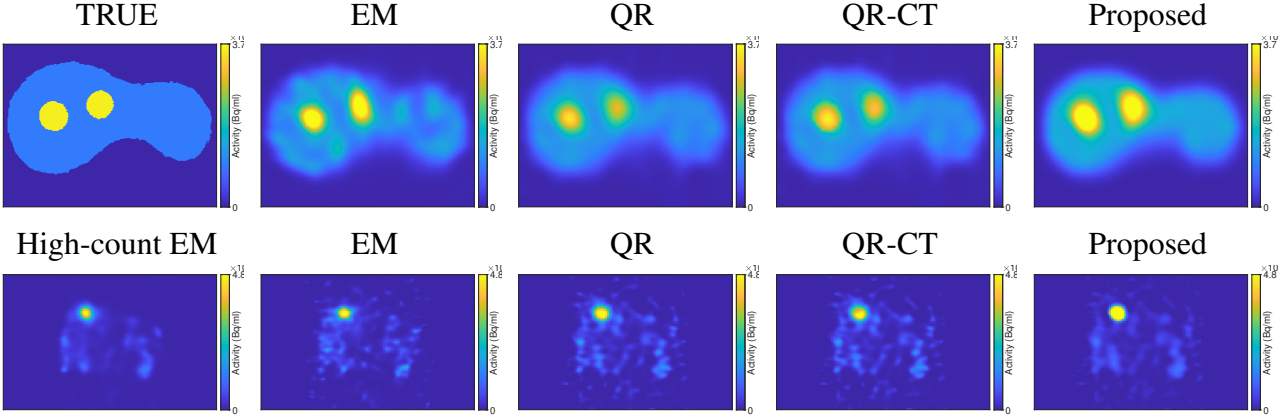
Figure 6.5: Reconstructed images of one slice from different reconstruction methods. (First row) Liver phantom true activity distribution and different reconstruction of the low-count data. (Second row) Coronal slice of the patient high-count EM reconstruction image and different reconstructions of the low-count data.

6.3.1 Results on CT segmentation

This section reports the evaluation result with LiTS test dataset. Since the ground truth (label) is not provided for the test dataset, we evaluated our segmentation network using the LiTS challenge web-page. Table 6.3 shows that our V-Net implementation in Section 6.2.2 achieves slightly worse DICE score than the first place in competition leader board. Fig. 6.4(c)-(d) shows the CT image of Lu-177 patient and segmentation result with trained V-Net. Though the CT is acquired with SPECT-CT machine that has relatively low quality compared to the diagnostic CT, the segmentation from V-Net was similar to the segmentation manually drawn by radiologist. For the phantom studies, we used the segmentation mask manually drawn on the CT because the geometry of phantom is far different from the human abdomen, therefore the trained network does not work for the phantom.

6.3.2 Results on SPECT reconstruction

Fig. 6.5-6.6 show that the proposed method improves overall reconstruction performance over the other conventional regularization methods (with or without anatomical information). Fig. 6.6 reports averaged evaluation metrics over realizations. For the liver phantom case, Fig. 6.5 shows that EM reconstruction gives noisy texture in the uniform background region. QR and QR-CT generates relatively less noisy image for the uniform region compared to EM. However, QR and QR-CT have less contrast between hot and warm region compared to EM and the proposed method. QR-CT has clear improvement over the QR in that it has clearer boundary as in the true image. The reconstructed image using the proposed method is closest true image. For the patient case, we

---

(a) Liver phantom: Noise vs AR   (b) Patient: CNR vs Iteration
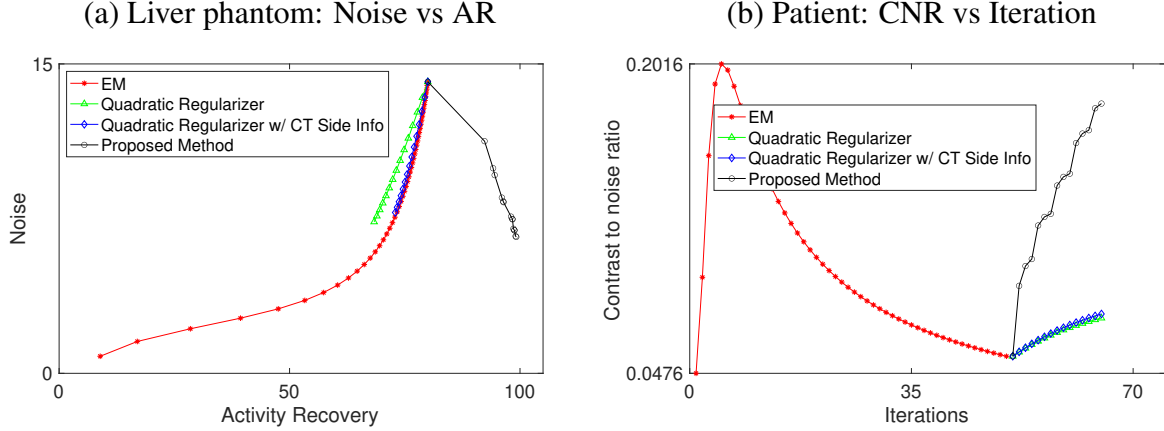
Figure 6.6: (a) Noise in uniform background liver phantom vs activity recovery in hot spot. (b) Contrast to noise ratio vs iteration in patient study. We initialized regularized methods with the 50th iterate of EM reconstruction.

visualize the reconstructed images with coronal view. Here, because the true activity distribution is unknown, we regard the EM reconstruction with high-count measurement as the true image. Similar to liver phantom case, the proposed method gives closest image to the high-count EM whereas QR and QR-CT exceedingly blurred the hot region.

Fig. 6.6 shows that proposed method achieves the best results in all evaluation metrics. In particular, the proposed method improves CNR compared to conventional regularizers. The proposed method also improved the noise in the background region while not sacrificing the AR as much as with conventional regularizers.

6.4 Discussion

This work showed the efficacy of sparsity-based trained regularizer using anatomical information on both qualitative and quantitative Lu-177 SPECT-CT imaging and compared between traditional non-trained regularizer using anatomical information. The proposed approach uses learned denoising neural network that exploits the information from dual modality system such as SPECT-CT. Specifically, the proposed framework uses the segmentation mask from the segmentation neural network as a weight for the trained regularizer. In the Lu-177 SPECT-CT liver phantom measurement where its activity distribution and count-rate mimic Lu-177 patient imaging, the recovery accuracy in the volume of interest was improved with the proposed approach compared to other non-trained regularizers. Improvements were also demonstrated for the patient measurement data.

To analyze how the trained denoising network utilizes the segmentation mask, we visualized the weights based on the segmentation mask with the sphere phantom described in Fig. 6.7. Fig. 6.7(i)-

(p) is visualizing the denoising process of the proposed method. As shown in Fig. 6.7(i)-(l), some filters and thresholding values are trained to behave similarly to finite differencing filter (see Fig. 6.7(e)-(h)). However, Fig. 6.7(m)-(p) shows that some filters and thresholding values are trained to zero out high intensity region using the weights from segmentation mask and sharpen the edge area around the high intensity region. In the present work, there are 100 sets of filters and thresholding values and each set of parameters is trained to behave differently from each other and some of those use the segmentation mask as a prior information where the region of interest is located.

However, using anatomical information would be beneficial only if the anatomical and emission images are mostly matching though utilizing segmentation mask can be less sensitive than using the boundary. The side information can be mismatched due to misregistration or differences between the functional (SPECT) and the anatomical (CT) imaging modalities. For example, anatomical image might show no anomalous voxels where functional images have high uptake, and vice versa. We plan to investigate whether including such cases in our training set would enable the CNN to 'learn' those outlier cases.

6.5   Conclusion

Exploiting the available information from a dual-modality system can benefit a trained regularizer. The proposed method uses the anatomical (CT) segmentation mask generated by segmentation neural network in a fully automatic way. The CT segmentation informs the SPECT denoising network where the region of interest is likely located. The proposed method achieved qualitative and quantitative improvements with the information from anatomical image compared to the non-trained quadratic regularizers with or without using the CT-side information. In particular, the proposed method improves the noise while not degrading the recovery accuracy. However, further investigation of the potential challenges including impact of misregistration between modalities is required. Future work also includes training and testing on measurement datasets where the discrepancies between modalities exist as well as training neural networks for segmentation and denoising together with a weighted combination of loss functions.
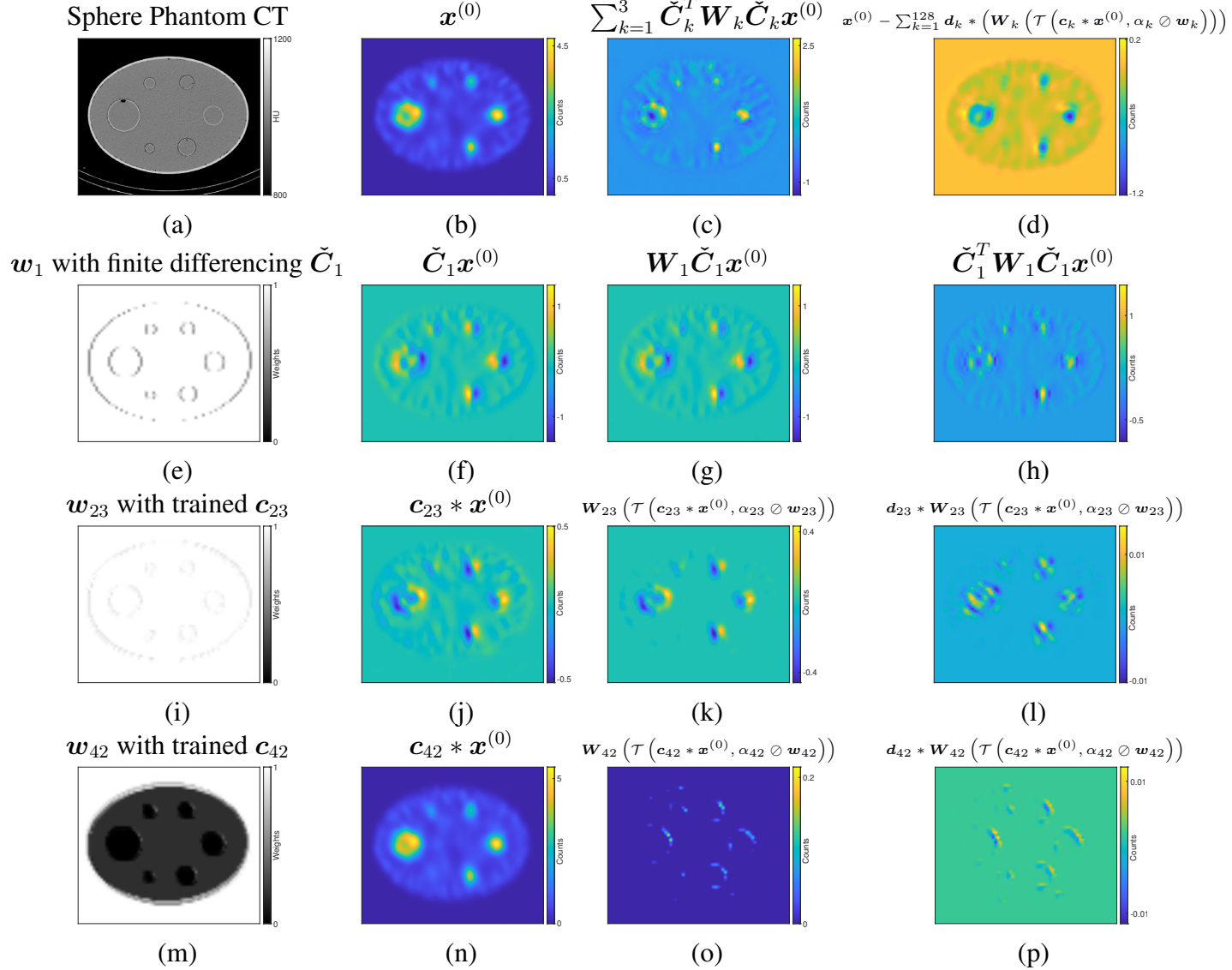
Figure 6.7: (a) CT image of the sphere phantom. (b) Initial image for the regularized methods. We used EM algorithm using 50 iterations. (c) $\nabla \mathsf{R}(\boldsymbol{x})$ of QR-CT for the update at first iteration. (d) $\nabla \mathsf{R}(\boldsymbol{x})$ of proposed method for the update at first iteration. (e)-(h) Denoising process with finite differencing matrix. $\check{\boldsymbol{C}}_1$ is a finite differencing matrix along x-direction. (i)-(p) Denoising process with trained convolutional filters.

CHAPTER 7

Conclusion and Future Work

7.1 Summary

For Y-90 PET, we have proposed a new formulation for bias reduction. The bias due to non-negativity constraint in OS-EM reconstruction is particularly problematic for Y-90 PET because of the low probability positron production and high random coincidence fraction. We proposed a formulation that relaxes the conventional image-domain nonnegativity constraint by instead imposing a positivity constraint on the predicted measurement mean that demonstrated improved quantification in simulation studies. We also tested the new reconstruction on clinically relevant TOF Y-90 PET measurements [6] and the new method outperformed conventional EM reconstruction available in the clinic. This study was performed with the collaboration of the Siemens PET Physics Division that provided us access to their TOF projector to implement our reconstruction with real data from the clinic PET system.

For Y-90 SPECT, we have proposed Y-90 SPECT reconstruction with a new model for tissue-dependent bremsstrahlung production. Experimental SPECT/CT measurements with equal Y-90 activity concentration in water and bone equivalent liquid demonstrated the Z dependence of bremsstrahlung generation and clearly demonstrated improved qualitative and quantitative accuracy with our new SPECT/CT reconstruction formulation including tissue dependent probabilities in the system matrix. This work has implications when using bremsstrahlung imaging in heterogeneous tissue such as marrow and bone (for example, bone marrow dosimetry).

Lastly, we have proposed learning based reconstruction method that mitigates bias effects with lower computational costs. We used an iterative framework that is composed of multiple trained neural networks enabling those in the later iterations to learn how to recover fine details. The framework is derived by an optimization formulation with a mathematical motivation, characterized by fewer parameters (order of a few thousand), thereby avoiding over-fitting and making training from small data sets feasible. The framework alternatively updates the reconstructed image and the denoised image with filters and soft-thresholding values trained at each iteration.

7.2 Future work

- A drawback of the proposed method for Y-90 PET to reduce bias associated with conventional non-negativity constraints is that it requires more computation cost compared to the standard method because of the need of an additional forward and back-projection at each iteration as well as the updates for auxiliary and dual variables. Finding an acceleration method with a convergence guarantee is a future work topic.

- For Y-90 SPECT reconstruction method with tissue dependent bremsstrahlung probabilities, SPECT-CT misalignment due to motion may reduce the benefits of the proposed method where CT information was used to determine voxel-level bone volume fractions. Evaluating the new method using simulations that include motion is a potential future work. Moreover, further investigation of the impact on clinical studies is required.

- For trained regularizer, we will further investigate a conventional edge-preserving non-convex regularizer that has similar form to the motivation of proposed method.

- For trained regularizer, it is natural to extend the method by training all filters simultaneously using a loss function for the final output image that is of interest, rather than any intermediate images. We will also investigate the impact of parameterizing and training the regularization parameter.

- For trained regularizer, we used mean squared error loss function based on reconstructed counts for simplicity, but using loss functions based on the ultimate task of interest, dosimetry, needs to be investigated. Here, our current CNN for reconstruction will be combined with a CNN for dose estimation in an end-to-end approach that uses a single dosimetry task based loss function.

- For trained regularizer, one possible future direction is investigating methods for adaptive selection of trainable parameter numbers depending on the size of training dataset.

- For trained regularizer using anatomical side information, further investigation of the potential challenges including impact of misregistration between modalities is required. Moreover, we will investigate the cases where training and testing on measurement datasets where discrepancies between modalities exist due to difference between physiology and anatomy. For example, 'lesions' with partial necrotic regions within the CT-defined contour where there is no uptake of the radiotracer.

- For trained regularizer using anatomical side information, training neural networks for segmentation and denoising together with a weighted combination of loss functions needs to

be examined.

- Unlike typical SPECT radionuclides, the Y-90 (bremsstrahlung) energy spectrum is continuous, hence energy window-based scatter correction available in most systems is inapplicable. Although Monte Carlo (MC) based scatter estimation has been proposed for Y-90, to reduce computational costs, we developed a CNN based approach to estimate the scatter projections using Monte Carlo only to generate ground truth data for training [139]. We expect the physics based approach, where CNN estimated scatter projections are included in the reconstruction model in a manner appropriate for Poisson statistics, will outperform post-reconstruction approaches. We will expand our initial architecture for scatter estimation to construct a CNN that has a radiation transport physics based foundation (not purely data driven), including imposing physics based constraints. The CNNs developed in the current work for image reconstruction will be combined with the CNNs for scatter estimation in an end-to-end approach using a single loss function.

Bibliography

[1] Y. K. Dewaraja, T. Devasia, R. K. Kaza, J. K. Mikell, D. Owen, P. L. Roberson, and M. J. Schipper, "Prediction of tumor control in 90Y radioembolization by logit models with PET/CT-based dose metrics," *Journal of Nuclear Medicine*, vol. 61, no. 1, pp. 104–111, 2020.

[2] Y. K. Dewaraja, M. J. Schipper, J. Shen, L. B. Smith, J. Murgic, H. Savas, E. Youssef, D. Regan, S. J. Wilderman, P. L. Roberson, *et al.*, "Tumor-absorbed dose predicts progression-free survival following 131I-tositumomab radioimmunotherapy," *Journal of Nuclear Medicine*, vol. 55, no. 7, pp. 1047–1053, 2014.

[3] J. K. Mikell, B. S. Majdalany, D. Owen, K. C. Paradis, and Y. K. Dewaraja, "Assessing spatial concordance between theranostic pairs using phantom and patient-specific acceptance criteria: Application to 99mTc-MAA SPECT/90Y-Microsphere PET," *International Journal of Radiation Oncology, Biology, Physics*, vol. 104, no. 5, pp. 1133–1140, 2019.

[4] K. P. Willowson, M. Tapner, and D. L. Bailey, "A multicentre comparison of quantitative 90Y PET/CT for dosimetric purposes after radioembolization with resin microspheres," *Eur. J. Nuc. Med.*, vol. 42, pp. 1202–22, May 2015.

[5] H. Lim, Y. K. Dewaraja, and J. A. Fessler, "A PET reconstruction formulation that enforces non-negativity in projection space for bias reduction in Y-90 imaging," *Physics in Medicine & Biology*, vol. 63, no. 3, p. 035042, 2018.

[6] H. Lim, K. Kim, Q. Li, J. Fessler, and Y. Dewaraja, "Bias reduction in Y-90 PET with reconstruction that relaxes the non-negativity constraint," in *Journal of Nuclear Medicine*, vol. 59, SOC NUCLEAR MEDICINE INC 1850 SAMUEL MORSE DR, RESTON, VA 20190-5316 USA, 2018.

[7] H. Lim, Y. K. Dewaraja, and J. A. Fessler, "Reducing bias in Y-90 PET images by enforcing non-negativity in projection space," in *2017 IEEE Nuclear Science Symposium and Medical Imaging Conference (NSS/MIC)*, pp. 1–4, IEEE, 2017.

[8] H. Lim, J. A. Fessler, S. J. Wilderman, A. F. Brooks, and Y. K. Dewaraja, "Y-90 SPECT ML image reconstruction with a new model for tissue-dependent bremsstrahlung production using CT information: a proof-of-concept study," *Physics in Medicine & Biology*, vol. 63, no. 11, p. 115001, 2018.

[9] H. Lim, Y. K. Dewaraja, S. J. Wilderman, and J. A. Fessler, "Y-90 SPECT maximum likelihood image reconstruction with a new model for tissue-dependent bremsstrahlung production," *Journal of Nuclear Medicine*, vol. 58, no. supplement 1, pp. 746–746, 2017.

[10] H. Lim, I. Y. Chun, Y. K. Dewaraja, and J. A. Fessler, "Improved low-count quantitative PET reconstruction with an iterative neural network," *IEEE transactions on medical imaging*, 2019. Submitted.

[11] H. Lim, I. Y. Chun, J. A. Fessler, and Y. K. Dewaraja, "Improved low count quantitative SPECT reconstruction with a trained deep learning based regularizer," in *Journal of Nuclear Medicine*, vol. 60, SOC NUCLEAR MEDICINE INC 1850 SAMUEL MORSE DR, RESTON, VA 20190-5316 USA, 2019.

[12] H. Lim, Z. Huang, J. A. Fessler, Y. K. Dewaraja, and I. Y. Chun, "Application of trained deep BCD-Net to iterative low-count PET image reconstruction," in *2018 IEEE Nuclear Science Symposium and Medical Imaging Conference (NSS/MIC)*, IEEE, 2018.

[13] H. Lim, Y. K. Dewaraja, and J. A. Fessler, "Joint low-count PET/CT segmentation and reconstruction with paired variational neural networks," in *Medical Imaging 2020: Physics of Medical Imaging*, vol. 11312, p. 113120U, International Society for Optics and Photonics, 2020.

[14] R. Salem, R. J. Lewandowski, L. Kulik, E. Wang, A. Riaz, R. K. Ryu, K. T. Sato, R. Gupta, P. Nikolaidis, F. H. Miller, *et al.*, "Radioembolization results in longer time-to-progression and reduced toxicity compared with chemoembolization in patients with hepatocellular carcinoma," *Gastroenterology*, vol. 140, no. 2, pp. 497–507, 2011.

[15] J. Edeline, L. Crouzet, B. Campillo-Gimenez, Y. Rolland, M. Pracht, A. Guillygomarc'h, K. Boudjema, L. Lenoir, X. Adhoute, T. Rohou, *et al.*, "Selective internal radiation therapy compared with sorafenib for hepatocellular carcinoma with portal vein thrombosis," *European journal of nuclear medicine and molecular imaging*, vol. 43, no. 4, pp. 635–643, 2016.

[16] L. Bodei, D. J. Kwekkeboom, M. Kidd, I. M. Modlin, and E. P. Krenning, "Radiolabeled somatostatin analogue therapy of gastroenteropancreatic cancer," in *Seminars in nuclear medicine*, vol. 46, pp. 225–238, Elsevier, 2016.

[17] J. Strosberg, G. El-Haddad, E. Wolin, A. Hendifar, J. Yao, B. Chasen, E. Mittra, P. L. Kunz, M. H. Kulke, H. Jacene, *et al.*, "Phase 3 trial of 177Lu-Dotatate for midgut neuroendocrine tumors," *New England Journal of Medicine*, vol. 376, no. 2, pp. 125–135, 2017.

[18] J. M. Ollinger and J. A. Fessler, "Positron emission tomography," *IEEE Sig. Proc. Mag.*, vol. 14, pp. 43–55, Jan. 1997.

[19] J. A. Sorenson and M. E. Phelps, *Physics in nuclear medicine*. Philadelphia: Saunders, 2 ed., 1987.

[20] T. Carlier, K. P. Willowson, E. Fourkal, D. L. Bailey, M. Doss, and M. Conti, "Y90-PET imaging: exploring limitations and accuracy under conditions of low counts and high random fraction," *Med. Phys.*, vol. 42, pp. 4295–309, June 2015.

[21] A. S. Pasciak, A. C. Bourgeois, J. M. McKinney, T. T. Chang, D. R. Osborne, S. N. Acuff, and Y. C. Bradley, "Radioembolization and the dynamic role of 90Y PET/CT," *Frontiers in Oncology*, vol. 4, Feb. 2014.

[22] J. Strydhorst, T. Carlier, A. Dieudonné, M. Conti, and I. Buvat, "A GATE evaluation of the sources of error in quantitative 90Y PET," *Med. Phys.*, vol. 43, pp. 5320–9, Sept. 2016.

[23] M. Ljungberg, A. Celler, M. W. Konijnenberg, K. F. Eckerman, Y. K. Dewaraja, and K. Sjögreen-Gleisner, "MIRD pamphlet no. 26: joint EANM/MIRD guidelines for quantitative 177Lu SPECT applied for dosimetry of radiopharmaceutical therapy," *Journal of nuclear medicine*, vol. 57, no. 1, pp. 151–162, 2016.

[24] Y. K. Dewaraja, E. C. Frey, G. Sgouros, A. B. Brill, P. Roberson, P. B. Zanzonico, and M. Ljungberg, "MIRD pamphlet no. 23: quantitative spect for patient-specific 3-dimensional dosimetry in internal radionuclide therapy," *Journal of Nuclear Medicine*, vol. 53, no. 8, pp. 1310–1325, 2012.

[25] C. S. Levin and E. J. Hoffman, "Calculation of positron range and its effect on the fundamental limit of positron emission tomography system spatial resolution," *Phys. Med. Biol.*, vol. 44, pp. 781–800, Mar. 1999.

[26] S. Strother, M. Casey, and E. Hoffman, "Measuring PET scanner sensitivity: relating coun-trates to image signal-to-noise ratios using noise equivalents counts," *Ieee transactions on nuclear science*, vol. 37, no. 2, pp. 783–788, 1990.

[27] L. A. Shepp and Y. Vardi, "Maximum likelihood reconstruction for emission tomography," *IEEE Trans. Med. Imag.*, vol. 1, pp. 113–22, Oct. 1982.

[28] L. A. Shepp and B. F. Logan, "The Fourier reconstruction of a head section," *IEEE Trans. Nuc. Sci.*, vol. 21, pp. 21–43, June 1974.

[29] A. C. Kak and M. Slaney, *Principles of computerized tomographic imaging*. New York: IEEE Press, 1988.

[30] R. M. Leahy and J. Qi, "Statistical approaches in quantitative positron emission tomography," *Statistics and Computing*, vol. 10, pp. 147–65, Apr. 2000.

[31] A. R. De Pierro, "On the relation between the ISRA and the EM algorithm for positron emission tomography," *IEEE Trans. Med. Imag.*, vol. 12, pp. 328–33, June 1993.

[32] J. A. Fessler, "Grouped coordinate descent algorithms for robust edge-preserving image restoration," in *Proc. SPIE 3170 Im. Recon. and Restor. II*, pp. 184–94, 1997.

[33] H. Erdogan and J. A. Fessler, "Monotonic algorithms for transmission tomography," *IEEE Trans. Med. Imag.*, vol. 18, pp. 801–14, Sept. 1999.

[34] D. S. Lalush and B. M. W. Tsui, "A generalized Gibbs prior for maximum a posteriori-EM SPECT reconstruction with fast and stable convergence properties," *J. Nuc. Med. (Abs. Book)*, vol. 33, p. 832, May 1992.

[35] A. R. De Pierro, "A modified expectation maximization algorithm for penalized likelihood estimation in emission tomography," *IEEE Trans. Med. Imag.*, vol. 14, pp. 132–7, Mar. 1995.

[36] W. H. Press, B. P. Flannery, S. A. Teukolsky, and W. T. Vetterling, *Numerical recipes in C*. New York: Cambridge Univ. Press, 1988.

[37] H. Gupta, K. H. Jin, H. Q. Nguyen, M. T. McCann, and M. Unser, "CNN-based projected gradient descent for consistent CT image reconstruction," *IEEE transactions on medical imaging*, vol. 37, no. 6, pp. 1440–1453, 2018.

[38] J. C. Ye, Y. Han, and E. Cha, "Deep convolutional framelets: A general deep learning framework for inverse problems," *SIAM Journal on Imaging Sciences*, vol. 11, no. 2, pp. 991–1048, 2018.

[39] I. Y. Chun, Z. Huang, H. Lim, and J. A. Fessler, "Momentum-net: Fast and convergent iterative neural network for inverse problems," *journal=IEEE transactions on pattern analysis and machine intelligence,*, 2019. Submitted.

[40] H. K. Aggarwal, M. P. Mani, and M. Jacob, "MoDL: model-based deep learning architecture for inverse problems," *IEEE Trans. Med. Imag.*, vol. 38, pp. 394–405, Feb. 2019.

[41] K. Hammernik, T. Klatzer, E. Kobler, M. P. Recht, D. K. Sodickson, T. Pock, and F. Knoll, "Learning a variational network for reconstruction of accelerated MRI data," *Magnetic resonance in medicine*, vol. 79, no. 6, pp. 3055–3071, 2018.

[42] K. Kim, D. Wu, K. Gong, J. Dutta, J. H. Kim, Y. D. Son, H. K. Kim, G. El Fakhri, and Q. Li, "Penalized PET reconstruction using deep learning prior and local linear fitting," *IEEE transactions on medical imaging*, vol. 37, no. 6, pp. 1478–1487, 2018.

[43] K. Gong, J. Guan, K. Kim, X. Zhang, J. Yang, Y. Seo, G. El Fakhri, J. Qi, and Q. Li, "Iterative PET image reconstruction using convolutional neural network representation," *IEEE transactions on medical imaging*, vol. 38, no. 3, pp. 675–685, 2019.

[44] U. Schmidt and S. Roth, "Shrinkage fields for effective image restoration," in *Proceedings of the IEEE Conference on Computer Vision and Pattern Recognition*, pp. 2774–2781, 2014.

[45] Y. A. LeCun, L. Bottou, G. B. Orr, and K.-R. Müller, "Efficient backprop," in *Neural networks: Tricks of the trade*, pp. 9–48, Springer, 2012.

[46] K. Gong, E. Berg, S. R. Cherry, and J. Qi, "Machine learning in PET: From photon detection to quantitative image reconstruction," *Proceedings of the IEEE*, vol. 108, no. 1, pp. 51–68, 2019.

[47] J. Xu, E. Gong, J. Pauly, and G. Zaharchuk, "200x low-dose PET reconstruction using deep learning," *arXiv preprint arXiv:1712.04119*, 2017.

[48] B. Yang, L. Ying, and J. Tang, "Artificial Neural Network Enhanced Bayesian PET Image Reconstruction," *IEEE Transactions on Medical Imaging*, vol. 37, pp. 1297–1309, June 2018.

[49] A. S. Pasciak, J. M. McKinney, and Y. C. Bradley, "Handbook of radioembolization: Physics, biology, nuclear medicine, and imaging," 2016.

[50] M. Vouche, B. Vanderlinden, P. Delatte, M. Lemort, A. Hendlisz, A. Deleporte, *et al.*, "New imaging techniques for 90Y microsphere radioembolization," *J Nucl Med Radiat Ther*, vol. 2, no. 113, p. 2, 2011.

[51] Y. K. Dewaraja, S. Y. Chun, R. N. Srinivasa, R. K. Kaza, K. C. Cuneo, B. S. Majdalany, P. M. Novelli, M. Ljungberg, and J. A. Fessler, "Improved quantitative Y-90 bremsstrahlung SPECT reconstruction with Monte Carlo scatter modeling," *Med. Phys.*, vol. 44, pp. 6364–76, Dec. 2017.

[52] C. Byrne, "Iterative algorithms for deblurring and deconvolution with constraints," *Inverse Prob.*, vol. 14, pp. 1455–67, Dec. 1998.

[53] K. Erlandsson, D. Visvikis, W. Waddington, I. Cullum, P. Jarritt, and L. Polowsky, "Low-statistics reconstruction with AB-EMML," in *Nuclear Science Symposium Conference Record, 2000 IEEE*, vol. 2, pp. 15–249, IEEE, 2000.

[54] J. Nuyts, S. Stroobants, P. Dupont, S. Vleugels, P. Flamen, and L. Mortelmans, "A dedicated ML-algorithm for non-attenuation corrected PET whole body images," in *Proc. IEEE Nuc. Sci. Symp. Med. Im. Conf.*, vol. 2, pp. 13/6–9, 2000.

[55] L. Grezes-Besset, J. Nuyts, R. Boellard, I. Buvat, C. Michel, C. Pierre, N. Costes, and A. Reilhac, "Simulation-based evaluation of NEG-ML iterative reconstruction of low count PET data," in *Nuclear Science Symposium Conference Record, 2007. NSS'07. IEEE*, vol. 4, pp. 3009–3014, IEEE, 2007.

[56] J. Nuyts, S. Stute, K. Van Slambrouck, F. van Velden, R. Boellaard, and C. Comtat, "Maximum-likelihood reconstruction based on a modified Poisson distribution to reduce bias in PET," in *2011 IEEE Nuclear Science Symposium Conference Record*, 2011.

[57] S. Sotthivirat and J. A. Fessler, "Image recovery using partitioned-separable paraboloidal surrogate coordinate ascent algorithms," *IEEE Trans. Im. Proc.*, vol. 11, pp. 306–17, Mar. 2002.

[58] J. A. Fessler and H. Erdogan, "A paraboloidal surrogates algorithm for convergent penalized-likelihood emission image reconstruction," in *Proc. IEEE Nuc. Sci. Symp. Med. Im. Conf.*, vol. 2, pp. 1132–5, 1998.

[59] K. Van Slambrouck, S. Stute, C. Comtat, M. Sibomana, F. van Velden, R. Boellaard, and J. Nuyts, "Bias reduction for low-statistics PET: Maximum likelihood reconstruction with a modified Poisson distribution," *IEEE Trans. Med. Imag.*, vol. 34, pp. 126–36, Jan. 2015.

[60] S. Boyd, N. Parikh, E. Chu, B. Peleato, and J. Eckstein, "Distributed optimization and statistical learning via the alternating direction method of multipliers," *Found. & Trends in Machine Learning*, vol. 3, no. 1, pp. 1–122, 2010.

[61] S. Z. Li, "Close-form solution and parameter selection for convex minimization-based edge-preserving smoothing," *IEEE Trans. Patt. Anal. Mach. Int.*, vol. 20, pp. 916–32, Sept. 1998.

[62] C. Kurz, J. Bauer, M. Conti, L. , L. Eriksson, and K. Parodi, "Investigating the limits of PET/CT imaging at very low true count rates and high random fractions in ion-beam therapy monitoring," *Med. Phys.*, vol. 42, pp. 3979–91, June 2015.

[63] M. L. Smits, M. Elschot, D. Y. Sze, Y. H. Kao, J. F. Nijsen, A. H. Iagaru, H. W. de Jong, M. A. van den Bosch, and M. G. Lam, "Radioembolization dosimetry: the road ahead," *Cardiovascular and interventional radiology*, vol. 38, no. 2, pp. 261–269, 2015.

[64] C. Fabbri, V. Mattone, M. Casi, F. L. De, M. Agostini, N. Bartolini, M. D'arienzo, G. Marchi, M. Bartolomei, and G. Sarti, "Quantitative evaluation on [90Y] DOTATOC PET and SPECT imaging by phantom acquisitions and clinical applications in locoregional and systemic treatments.," *The quarterly journal of nuclear medicine and molecular imaging: official publication of the Italian Association of Nuclear Medicine (AIMN)[and] the International Association of Radiopharmacology (IAR),[and] Section of the Society of..*, vol. 56, no. 6, pp. 522–528, 2012.

[65] D. Minarik, K. Sjögreen-Gleisner, O. Linden, K. Wingårdh, J. Tennvall, S.-E. Strand, and M. Ljungberg, "90Y Bremsstrahlung imaging for absorbed-dose assessment in high-dose radioimmunotherapy," *Journal of Nuclear Medicine*, vol. 51, no. 12, pp. 1974–1978, 2010.

[66] T. W. Barber, K. S. Yap, M. H. Cherk, A. Powell, and V. Kalff, "Comparison of positron emission tomography/CT and bremsstrahlung imaging following Y-90 radiation synovectomy," *Journal of medical imaging and radiation oncology*, vol. 57, no. 5, pp. 567–571, 2013.

[67] L. Van Elmbt, S. Vandenberghe, S. Walrand, S. Pauwels, and F. Jamar, "Comparison of yttrium-90 quantitative imaging by TOF and non-TOF PET in a phantom of liver selective internal radiotherapy," *Physics in Medicine & Biology*, vol. 56, no. 21, p. 6759, 2011.

[68] D. Minarik, K. S. Gleisner, and M. Ljungberg, "Evaluation of quantitative 90Y SPECT based on experimental phantom studies," *Physics in Medicine & Biology*, vol. 53, no. 20, p. 5689, 2008.

[69] A. Cengiz and E. Almaz, "Internal bremsstrahlung spectra of β-particle emitters using the Monte Carlo method," *Radiation Physics and Chemistry*, vol. 70, no. 6, pp. 661–668, 2004.

[70] P. Venkataramaiah, H. Sanjeeviah, and B. Sanjeevaiah, "Study of inner bremsstrahlung accompanying beta decay in 185W and 90Y," *Journal of Physics G: Nuclear Physics*, vol. 6, no. 11, p. 1443, 1980.

[71] S. Walrand, M. Hesse, F. Jamar, and R. Lhommel, "The origin and reduction of spurious extrahepatic counts observed in 90Y non-TOF PET imaging post radioembolization," *Physics in Medicine & Biology*, vol. 63, no. 7, p. 075016, 2018.

[72] H. Bethe and W. Heitler, "On the stopping of fast particles and on the creation of positive electrons," in *Proc. R. Soc. Lond. A*, vol. 146, pp. 83–112, The Royal Society, 1934.

[73] X. Rong, Y. Du, M. Ljungberg, E. Rault, S. Vandenberghe, and E. C. Frey, "Development and evaluation of an improved quantitative 90Y bremsstrahlung SPECT method," *Medical physics*, vol. 39, no. 5, pp. 2346–2358, 2012.

[74] M. Elschot, M. G. Lam, M. A. van den Bosch, M. A. Viergever, and H. W. de Jong, "Quantitative Monte Carlo-based 90Y SPECT reconstruction," *Journal of Nuclear Medicine*, vol. 54, no. 9, pp. 1557–1563, 2013.

[75] Y. K. Dewaraja, S. Y. Chun, R. N. Srinivasa, R. K. Kaza, K. C. Cuneo, B. S. Majdalany, P. M. Novelli, M. Ljungberg, and J. A. Fessler, "Improved quantitative 90Y bremsstrahlung SPECT/CT reconstruction with Monte Carlo scatter modeling," *Medical physics*, vol. 44, no. 12, pp. 6364–6376, 2017.

[76] F. Salvat, J. M. Fernández-Varea, and J. Sempau, "PENELOPE-2006: A code system for Monte Carlo simulation of electron and photon transport," in *Workshop proceedings*, vol. 4, 2006.

[77] S. M. Seltzer and M. J. Berger, "Bremsstrahlung energy spectra from electrons with kinetic energy 1 keV–10 GeV incident on screened nuclei and orbital electrons of neutral atoms with $Z = 1$–100," *Atomic Data and Nuclear Data Tables*, vol. 35, no. 3, pp. 345–418, 1986.

[78] X. Mougeot, "Reliability of usual assumptions in the calculation of β and ν spectra," *Physical Review C*, vol. 91, no. 5, p. 055504, 2015.

[79] M. J. Berger, "ESTAR, PSTAR, and ASTAR: Computer programs for calculating stopping-power and range tables for electrons, protons, and helium ions," 1992.

[80] O. de Dreuille, V. Strijckmans, P. Ameida, C. Loc'h, and B. Bendriem, "Bone equivalent liquid solution to assess accuracy of transmission measurements in SPECT and PET," *IEEE Transactions on Nuclear Science*, vol. 44, no. 3, pp. 1186–1190, 1997.

[81] M. Park, A. Mahmood, R. E. Zimmerman, N. Limpa-Amara, G. M. Makrigiorgos, and S. C. Moore, "Adsorption of metallic radionuclides on plastic phantom walls," *Medical physics*, vol. 35, no. 4, pp. 1606–1610, 2008.

[82] K. F. Koral, A. Yendiki, and Y. K. Dewaraja, "Recovery of total I-131 activity within focal volumes using SPECT and 3D OSEM," *Physics in Medicine & Biology*, vol. 52, no. 3, p. 777, 2007.

[83] Y. Dewaraja, P. Novelli, J. Fessler, M. Feng, R. Nelson, J. Rothley, M. Ljungberg, P. Roberson, and S. Wilderman, "Y-90 imaging for dosimetry in radioembolization: comparison between scatter corrected bremsstrahlung SPECT/CT and time-of-flight PET/CT," in *EUROPEAN JOURNAL OF NUCLEAR MEDICINE AND MOLECULAR IMAGING*, vol. 42, pp. S156–S157, SPRINGER 233 SPRING ST, NEW YORK, NY 10013 USA, 2015.

[84] W. Segars, G. Sturgeon, S. Mendonca, J. Grimes, and B. M. Tsui, "4D XCAT phantom for multimodality imaging research," *Medical physics*, vol. 37, no. 9, pp. 4902–4915, 2010.

[85] S. Ahn, S. G. Ross, E. Asma, J. Miao, X. Jin, L. Cheng, S. D. Wollenweber, and R. M. Manjeshwar, "Quantitative comparison of OSEM and penalized likelihood image reconstruction using relative difference penalties for clinical PET," *Physics in Medicine & Biology*, vol. 60, no. 15, p. 5733, 2015.

[86] G. Wang, J. C. Ye, K. Mueller, and J. A. Fessler, "Image reconstruction is a new frontier of machine learning," *IEEE Trans. Med. Imag.*, vol. 37, pp. 1289–96, June 2018.

[87] H. Chen, Y. Zhang, M. K. Kalra, F. Lin, Y. Chen, P. Liao, J. Zhou, and G. Wang, "Low-dose CT with a residual encoder-decoder convolutional neural network," *IEEE transactions on medical imaging*, vol. 36, no. 12, pp. 2524–2535, 2017.

[88] K. H. Jin, M. T. McCann, E. Froustey, and M. Unser, "Deep convolutional neural network for inverse problems in imaging," *IEEE Transactions on Image Processing*, vol. 26, no. 9, pp. 4509–4522, 2017.

[89] I. Y. Chun, H. Lim, Z. Huang, and J. A. Fessler, "Fast and convergent iterative signal recovery using trained convolutional neural networks," in *Proc. Allerton Conf. on Commun., Control, and Comput.*, (Allerton, IL), Oct. 2018.

[90] J. Sun, H. Li, Z. Xu, *et al.*, "Deep ADMM-Net for compressive sensing MRI," in *Advances in neural information processing systems*, pp. 10–18, 2016.

[91] M. Mardani, E. Gong, J. Y. Cheng, S. S. Vasanawala, G. Zaharchuk, L. Xing, and J. M. Pauly, "Deep generative adversarial neural networks for compressive sensing MRI," *IEEE transactions on medical imaging*, vol. 38, no. 1, pp. 167–179, 2019.

[92] G. Yang, S. Yu, H. Dong, G. Slabaugh, P. L. Dragotti, X. Ye, F. Liu, S. Arridge, J. Keegan, Y. Guo, *et al.*, "DAGAN: deep de-aliasing generative adversarial networks for fast compressed sensing MRI reconstruction," *IEEE transactions on medical imaging*, vol. 37, no. 6, pp. 1310–1321, 2018.

[93] I. Haggstrom, C. R. Schmidtlein, G. Campanella, and T. J. Fuchs, "DeepPET: A deep encoder-decoder network for directly solving the PET image reconstruction inverse problem," *Med. Im. Anal.*, vol. 54, pp. 253–62, May 2019.

[94] O. Ronneberger, P. Fischer, and T. Brox, "U-net: Convolutional networks for biomedical image segmentation," pp. 234–241, Springer, 2015.

[95] K. Zhang, W. Zuo, Y. Chen, D. Meng, and L. Zhang, "Beyond a Gaussian denoiser: Residual learning of deep CNN for image denoising," *IEEE Transactions on Image Processing*, vol. 26, pp. 3142–3155, July 2017.

[96] K. Gregor and Y. LeCun, "Learning fast approximations of sparse coding," in *Proceedings of the 27th International Conference on International Conference on Machine Learning*, pp. 399–406, Omnipress, 2010.

[97] Y. Chen and T. Pock, "Trainable nonlinear reaction diffusion: A flexible framework for fast and effective image restoration," *IEEE transactions on pattern analysis and machine intelligence*, vol. 39, no. 6, pp. 1256–1272, 2017.

[98] Y. Chun and J. A. Fessler, "Deep BCD-Net using identical encoding-decoding CNN structures for iterative image recovery," in *2018 IEEE 13th Image, Video, and Multidimensional Signal Processing Workshop (IVMSP)*, pp. 1–5, IEEE, 2018.

[99] I. Y. Chun and J. A. Fessler, "Convolutional analysis operator learning: acceleration and convergence," *IEEE Transactions on Image Processing*, vol. 29, no. 1, pp. 2108–2122, 2019.

[100] A. S. Pasciak, A. C. Bourgeois, J. M. McKinney, T. T. Chang, D. R. Osborne, S. N. Acuff, and Y. C. Bradley, "Radioembolization and the dynamic role of 90Y PET/CT," *Frontiers in oncology*, vol. 4, p. 38, 2014.

[101] J. Nuyts, D. Beque, P. Dupont, and L. Mortelmans, "A concave prior penalizing relative differences for maximum-a-posteriori reconstruction in emission tomography," *IEEE Transactions on nuclear science*, vol. 49, no. 1, pp. 56–60, 2002.

[102] L. Pfister and Y. Bresler, "Learning sparsifying filter banks," in *Wavelets and Sparsity XVI*, vol. 9597, p. 959703, International Society for Optics and Photonics, 2015.

[103] J.-F. Cai, H. Ji, Z. Shen, and G.-B. Ye, "Data-driven tight frame construction and image denoising," *Applied and Computational Harmonic Analysis*, vol. 37, no. 1, pp. 89–105, 2014.

[104] Z. Zhang, S. Rose, J. Ye, A. E. Perkins, B. Chen, C.-M. Kao, E. Y. Sidky, C.-H. Tung, and X. Pan, "Optimization-based image reconstruction from low-count, list-mode TOF-PET data," *IEEE Transactions on Biomedical Engineering*, vol. 65, no. 4, pp. 936–946, 2018.

[105] A. Chambolle and T. Pock, "An introduction to continuous optimization for imaging," *Acta Numerica*, vol. 25, pp. 161–319, 2016.

[106] S. Y. Chun, Y. K. Dewaraja, and J. A. Fessler, "Alternating direction method of multiplier for tomography with nonlocal regularizers," *IEEE transactions on medical imaging*, vol. 33, no. 10, pp. 1960–1968, 2014.

[107] A. Paszke, S. Gross, S. Chintala, G. Chanan, E. Yang, Z. DeVito, Z. Lin, A. Desmaison, L. Antiga, and A. Lerer, "Automatic differentiation in PyTorch," 2017.

[108] D. P. Kingma and J. Ba, "Adam: A method for stochastic optimization," *arXiv preprint arXiv:1412.6980*, 2014.

[109] R. Leahy and X. Yan, "Incorporation of anatomical MR data for improved functional imaging with PET," in *Biennial International Conference on Information Processing in Medical Imaging*, pp. 105–120, Springer, 1991.

[110] J. A. Fessler, N. H. Clinthorne, and W. L. Rogers, "Regularized emission image reconstruction using imperfect side information," *IEEE Transactions on Nuclear Science*, vol. 39, no. 5, pp. 1464–1471, 1992.

[111] X. Ouyang, W. H. Wong, V. E. Johnson, X. Hu, and C.-T. Chen, "Incorporation of correlated structural images in PET image reconstruction," *IEEE Transactions on Medical Imaging*, vol. 13, no. 4, pp. 627–640, 1994.

[112] J. E. Bowsher, V. E. Johnson, T. G. Turkington, R. J. Jaszczak, C. Floyd, and R. E. Coleman, "Bayesian reconstruction and use of anatomical a priori information for emission tomography," *IEEE Transactions on Medical Imaging*, vol. 15, no. 5, pp. 673–686, 1996.

[113] B. A. Ardekani, M. Braun, B. F. Hutton, I. Kanno, and H. Iida, "Minimum cross-entropy reconstruction of PET images using prior anatomical information," *Physics in Medicine & Biology*, vol. 41, no. 11, p. 2497, 1996.

[114] S. Sastry and R. E. Carson, "Multimodality bayesian algorithm for image reconstruction in positron emission tomography: a tissue composition model," *IEEE Transactions on Medical imaging*, vol. 16, no. 6, pp. 750–761, 1997.

[115] B. Lipinski, H. Herzog, E. R. Kops, W. Oberschelp, and H. Muller-Gartner, "Expectation maximization reconstruction of positron emission tomography images using anatomical magnetic resonance information," *IEEE transactions on medical imaging*, vol. 16, no. 2, pp. 129–136, 1997.

[116] A. O. Hero, R. Piramuthu, J. A. Fessler, and S. R. Titus, "Minimax emission computed tomography using high-resolution anatomical side information and B-spline models," *IEEE Transactions on Information Theory*, vol. 45, no. 3, pp. 920–938, 1999.

[117] A. Rangarajan, T. Hsiao, and G. Gindi, "A Bayesian joint mixture framework for the integration of anatomical information in functional image reconstruction," *Journal of Mathematical Imaging and Vision*, vol. 12, no. 3, pp. 199–217, 2000.

[118] C. Comtat, P. E. Kinahan, J. A. Fessler, T. Beyer, D. W. Townsend, M. Defrise, and C. Michel, "Clinically feasible reconstruction of 3D whole-body PET/CT data using blurred anatomical labels," *Physics in Medicine & Biology*, vol. 47, no. 1, p. 1, 2001.

[119] J. E. Bowsher, H. Yuan, L. W. Hedlund, T. G. Turkington, G. Akabani, A. Badea, W. C. Kurylo, C. T. Wheeler, G. P. Cofer, M. W. Dewhirst, *et al.*, "Utilizing MRI information to estimate F18-FDG distributions in rat flank tumors," in *IEEE Symposium Conference Record Nuclear Science 2004.*, vol. 4, pp. 2488–2492, IEEE, 2004.

[120] K. Baete, J. Nuyts, W. Van Paesschen, P. Suetens, and P. Dupont, "Anatomical-based FDG-PET reconstruction for the detection of hypo-metabolic regions in epilepsy," *IEEE transactions on medical imaging*, vol. 23, no. 4, pp. 510–519, 2004.

[121] A. M. Alessio and P. E. Kinahan, "Improved quantitation for PET/CT image reconstruction with system modeling and anatomical priors," *Medical physics*, vol. 33, no. 11, pp. 4095–4103, 2006.

[122] F. Bataille, C. Comtat, S. Jan, F. Sureau, and R. Trebossen, "Brain PET partial-volume compensation using blurred anatomical labels," *IEEE Transactions on Nuclear Science*, vol. 54, no. 5, pp. 1606–1615, 2007.

[123] J. Tang and A. Rahmim, "Bayesian PET image reconstruction incorporating anato-functional joint entropy," *Physics in Medicine & Biology*, vol. 54, no. 23, p. 7063, 2009.

[124] L. Cao and J. Peter, "Bayesian reconstruction strategy of fluorescence-mediated tomography using an integrated SPECT-CT-OT system," *Physics in Medicine & Biology*, vol. 55, no. 9, p. 2693, 2010.

[125] S. Somayajula, C. Panagiotou, A. Rangarajan, Q. Li, S. R. Arridge, and R. M. Leahy, "PET image reconstruction using information theoretic anatomical priors," *IEEE transactions on medical imaging*, vol. 30, no. 3, pp. 537–549, 2010.

[126] Y. K. Dewaraja, K. F. Koral, and J. A. Fessler, "Regularized reconstruction in quantitative SPECT using CT side information from hybrid imaging," *Physics in Medicine & Biology*, vol. 55, no. 9, p. 2523, 2010.

[127] J. Cheng-Liao and J. Qi, "PET image reconstruction with anatomical edge guided level set prior," *Physics in Medicine & Biology*, vol. 56, no. 21, p. 6899, 2011.

[128] M. Shidahara, C. Tsoumpas, C. McGinnity, T. Kato, H. Tamura, A. Hammers, H. Watabe, and F. Turkheimer, "Wavelet-based resolution recovery using an anatomical prior provides quantitative recovery for human population phantom PET [11C] raclopride data," *Physics in Medicine & Biology*, vol. 57, no. 10, p. 3107, 2012.

[129] V.-G. Nguyen and S.-J. Lee, "Incorporating anatomical side information into PET reconstruction using nonlocal regularization," *IEEE transactions on Image Processing*, vol. 22, no. 10, pp. 3961–3973, 2013.

[130] R. Loeb, N. Navab, and S. I. Ziegler, "Direct parametric reconstruction using anatomical regularization for simultaneous PET/MRI data," *IEEE transactions on medical imaging*, vol. 34, no. 11, pp. 2233–2247, 2015.

[131] S. Chen, H. Liu, P. Shi, and Y. Chen, "Sparse representation and dictionary learning penalized image reconstruction for positron emission tomography," *Physics in Medicine & Biology*, vol. 60, no. 2, p. 807, 2015.

[132] W. Hutchcroft, G. Wang, K. T. Chen, C. Catana, and J. Qi, "Anatomically-aided PET reconstruction using the kernel method," *Physics in Medicine & Biology*, vol. 61, no. 18, p. 6668, 2016.

[133] K. Gong, J. Cheng-Liao, G. Wang, K. T. Chen, C. Catana, and J. Qi, "Direct patlak reconstruction from dynamic PET data using the kernel method with MRI information based on structural similarity," *IEEE transactions on medical imaging*, vol. 37, no. 4, pp. 955–965, 2017.

[134] J. A. Fessler, "Optimization methods for magnetic resonance image reconstruction: Key models and optimization algorithms," *IEEE Signal Processing Magazine*, vol. 37, no. 1, pp. 33–40, 2020.

[135] P. A. Wolf, J. S. Jørgensen, T. G. Schmidt, and E. Y. Sidky, "Few-view single photon emission computed tomography (SPECT) reconstruction based on a blurred piecewise constant object model," *Physics in Medicine & Biology*, vol. 58, no. 16, p. 5629, 2013.

[136] F. Milletari, N. Navab, and S.-A. Ahmadi, "V-net: Fully convolutional neural networks for volumetric medical image segmentation," in *2016 Fourth International Conference on 3D Vision (3DV)*, pp. 565–571, IEEE, 2016.

[137] P. Bilic, P. F. Christ, E. Vorontsov, G. Chlebus, H. Chen, Q. Dou, C.-W. Fu, X. Han, P.-A. Heng, J. Hesser, *et al.*, "The liver tumor segmentation benchmark (LiTS)," *arXiv preprint arXiv:1901.04056*, 2019.

[138] D. White and R. S. Lawson, "A Poisson resampling method for simulating reduced counts in nuclear medicine images," *Physics in Medicine & Biology*, vol. 60, no. 9, p. N167, 2015.

[139] H. Xiang, H. Lim, J. A. Fessler, and Y. K. Dewaraja, "SPECT/CT scatter correction using deep learning: implementation in Y-90 imaging.," in *IEEE Nuclear Science Symposium and Medical Imaging Conference (NSS/MIC)*, IEEE, 2019. To appear.